COO-2245-50

COOLANT MIXING IN LMFBR ROD BUNDLES AND OUTLET PLENUM MIXING TRANSIENTS

Progress Report

Principal Investigators
Neil E. Todreas - Tasks I and II
Michael W. Golay - Task III
Lothar Wolf - Task IV

Massachusetts Institute of Technology
Department of Nuclear Engineering
Cambridge, Massachusetts 02139

March 1, 1977 - May 31, 1977

Prepared for the U.S. Energy Research and Development Administration under Contract No. AT(11-1)-2245

DISCLAIMER

"This report was prepared as an account of Government-sponsored work. Neither the United States, or the Energy Research and Development Administration nor any person acting on behalf of the Commission

A. Makes any warranty or representation, expressed or implied, with respect to the accuracy, completeness or usefulness of the information contained in this report, or that the use of any information, apparatus method, or process disclosed in this report may not infringe privately owned rights; or

B. Assumes any liabilities with respect to the use of, or for damages resulting from the use of, any information, apparatus, method, or process disclosed in this report.

As used in the above, 'person acting on behalf of the Commission' includes any employee or contractor of the Administration or employee of such contractor, to the extent that such employee or contractor prepares, disseminates, or provides access to, any information pursuant to his employment or contract with the Administration or his employment with such contractor."

Reports and Papers Published under
MIT Coolant Mixing in LMFBR Rod Bundles Project

A. Quarterly Progress Reports (Available from National Technical Information Service, U.S. Department of Commerce, Springfield, VA 22151)

COO-2245-1	Period June 1, 1972 - November 30, 1972
COO-2245-2	Period December 1, 1972 - February 28, 1973
COO-2245-3	Period March 1, 1973 - May 31, 1973
COO-2245-6	Period June 1, 1973 - August 31, 1973
COO-2245-7	Period September 1, 1973 - November 30, 1973
COO-2245-8	Period December 1, 1973 - February 28, 1974
COO-2245-10	Period March 1, 1974 - May 31, 1974
COO-2245-13	Period June 1, 1974 - August 31, 1974
COO-2245-14	Period September 1, 1974 - November 31, 1974
COO-2245-15	Period December 1, 1974 - February 28, 1975
COO-2245-23	Period March 1, 1975 - May 31, 1975
COO-2245-25	Period June 1, 1975 - August 31, 1975
COO-2245-26	Period September 1, 1975 - November 30, 1975
COO-2245-28	Period December 1, 1975 - February 29, 1976
COO-2245-30	Period March 1, 1976 - May 31, 1976
COO-2245-31	Period June 1, 1976 - August 31, 1976
COO-2245-34	Period September 1, 1976 - November 30, 1976
COO-2245-38	Period December 1, 1976 - February 28, 1977
COO-2245-50	Period March 1, 1977 - May 31, 1977

Reports Issued Under This Contract

B. Topical Reports (Available from National Technical Information Service, U.S. Department of Commerce, Springfield, VA 22151)

E. Khan and N. Todreas, "A Review of Recent Analytical and Experimental Studies Applicable to LMFBR Fuel and Blanket Assembly Design," COO-2245-4TR, MIT, Sept. 1973.

E. Khan, W. Rohsenow, A. Sonin and N. Todreas, "A Simplified Approach for Predicting Temperature Distribution in Wire Wrapped Assemblies," COO-2245-5TR, MIT, Sept. 1973.

T. Eaton and N. Todreas, "Instrumentation Methods for Interchannel Coolant Mixing Studies in Wire-Wrap Spaced Nuclear Fuel Assemblies," COO-2245-9TR, MIT, June 1974.

Y.B. Chen, K. Ip, N.E. Todreas, "Velocity Measurements in Edge Subchannels of Wire Wrapped LMFBR Fuel Assemblies," COO-2245-11TR, MIT, September 1974.

E. Khan, N. Todreas, W. Rohsenow, A.A. Sonin, "Analysis of Mixing Data Relevant to Wire-Wrapped Fuel Assembly Thermal-Hydraulic Design," COO-2245-12TR, MIT, September 1974.

E. Khan, W. Rohsenow, A. Sonin, N. Todreas, "A Porous Body Model for Predicting Temperature Distributions in Wire Wrapped Fuel and Blanket Assemblies of a LMFBR," COO-2245-16TR, MIT, March 1975.

E. Khan, W.M. Rohsenow, A. Sonin, N. Todreas, "Input Parameters to the ENERGY Code (To be used with the ENERGY Code Manual) COO-2245-17TR, MIT, May 1975.

E. Khan, W. Rohsenow, A. Sonin, N. Todreas, "Manual for ENERGY Codes I, II, III," COO-2245-18TR, MIT, May 1975

E. Khan, W. Rohsenow, A. Sonin, N. Todreas, "Manual for ENERGY Codes I, II, III Computer Programs," COO-2245-18TR Revision 1, MIT, July 1976.

P. Carajilescov and N. Todreas, "Experimental and Analytical Study of Axial Turbulent Flows in an Interior Subchannel of a Bare Rod Bundle," COO-2245-19TR, MIT.

B. Chen and N. Todreas, "Prediction of Coolant Temperature Field in a Breeder Reactor Including Interassembly Heat Transfer," COO-2245-20TR, MIT, May 1975.

B. Chen and N. Todreas, "Prediction of Coolant Temperature Field in a Breeder Reactor Inlcuding Interassembly Heat Transfer," COO-2245-20TR Revision 1, MIT, December 1976.

F. Carre and N. Todreas, "Development of Input Data to ENERGY Code for Analysis of Reactor Fuel Bundles," COO-2245-21TR, MIT, May 1975.

Reports Issued Under This Contract

B. Topical Reports, Continued

H. Ninokata and N.E. Todreas, "Turbulent Momentum Exchange Coefficients for Reactor Fuel Bundle Analysis," COO-2245-22TR, MIT, June 1975.

R. Anoba and N. Todreas, "Coolant Mixing in LMFBR Rod Bundles and Outlet Plenum Mixing Transients," COO-2245-24TR, August 1975.

B. Bosy, "Fabrication Details for Wire Wrapped Fuel Assembly Components," COO-2245-27TR, MIT, November 1975.

Ralph C. Bennett and Michael W. Golay, "Interferometric Investigation of Turbulently Fluctuating Temperature in an LMFBR Outlet Plenum Geometry," COO-2245-29TR, MIT, June 1976.

N.E. Todreas, "Analysis Methods for LMFBR Wire Wrapped Bundles," COO-2245-32TR, MIT, November 1976.

K.L. Basehore and N.E. Todreas, "Development of Stability Criteria and an Interassembly Conduction Model for the Thermal-Hydraulics Code SUPERENERGY," COO-2245-33TR, MIT December 1976.

Robert Masterson and Neil E. Todreas, "Analysis of the Feasibility of Implementing an Implicit Temporal Differencing Scheme in the SUPERENERGY Code," COO-2245-35TR, MIT, February 1977.

S. Glazer, C. Chiu and N. Todreas, "Collection and Evaluation of Salt Mixing Data with the Real Time Data Acquisition System," COO-2245-36TR, MIT, April 1977.

B. Mikic, E.U. Khan and N.E. Todreas "An Approximate Method for Predicting Temperature Distribution in Wire Wrapped Fuel Assemblies of a LMFBR," COO-2245-37TR, MIT, April 1977.

C. Chiu and N. Todreas, "Development of a Technique for Subchannel Flow Rate Measurements in LMFBR Wire Wrapped Assemblies," COO-2245-39TR, July 1977

C. Chiu and N. Todreas, "WARD Blanket Assembly Pre-Test Predictions by SUPERENERGY," COO-2245-40TR, July 1977

C. Chiu and N. Todreas, "Flow Split for a LMFBR 4" Wire Wrapped Blanket Assembly," COO-2245-41TR, July 1977

C. Chiu and N. Todreas, "Static Pressure and Pressure Drop for a LMFBR 4" Wire Wrapped Blanket Assembly," COO-2245-42TR, July 1977

Reports Issued Under This Contract

B. Topical Reports, Continued

C. Chiu and N. Todreas, "Mixing Experiments for a LMFBR 4" Wire Wrapped Blanket Assembly," COO-2245-43TR, July 1977

Yi Bin Chen and Michael W. Golay, "Coolant Mixing in the LMFBR Outlet Plenum," COO-2245-44TR, June 1977.

J. Kelly and N. Todreas, "Turbulent Interchange in Triangular Array Bare Rod Bundles," COO-2245-45TR, July 1977

K.L. Basehore and N.E. Todreas, "Assessment of the Need to Incorporate a Variable Swirl Flow Model into the ENERGY Code," COO-2245-46TR, July 1977.

K.L. Basehore and N. Todreas, "Analysis of the Thermal-Hydraulic Behavior in the CRBR Secondary Control Assembly, Including Interassembly Heat Transfer Effects," COO-2245-47TR, July 1977.

J.G. Bartzis and N.E. Todreas, "Hydrodynamic Behavior of a Bare Rod Bundle," COO-2245-48TR, June 1977.

M.R. Fakori-Monazah and N.E. Todreas, "Measurement and Analysis of Flow Wall Shear Stress in an Interior Subchannel of Triangular Array Rods," COO-2245-49TR, August 1977.

Reports Issued under this Contract

C. Papers and Summaries

Yi Bin Chen, Ka-Lam Ip, Neil E. Todreas, "Velocity Measurements in Edge Channels of Wire-Wrapped LMFBR Fuel Assemblies," American Nuclear Society Transactions Vol. 19, 1974, pp. 323-324.

P. Carajilescov, N. Todreas, "Experimental and Analytical Study of Axial Turbulent Flows in an Interior Subchannel of a Bare Rod Bundle," J. of Heat Transfer, Vol. 98, No. 2, May 1976, pp. 262-268 (Included as Appendix to Quarterly Progress Report, COO-2245-15).

E. Khan, W. Rohsenow, A. Sonin, N. Todreas, "A Porous Body Model for Predicting Temperature Distribution in Wire-Wrapped Fuel Rod Assemblies," Nuclear Engineering and Design, 35 (1975) 1-12.

E. Khan, W. Rohsenow, A. Sonin, N. Todreas, "A Porous Body Model for Predicting Temperature Distribution in Wire-Wrapped Rod Assemblies Operating in Combined Forced and Free Convection," Nuclear Engineering and Design, 35 (1975) 199-211.

Ralph G. Bennett and Michael W. Golay, "Development of an Optical Method for Measurement of Temperature Fluctuation in Turbulent Flows," American Nuclear Society Transactions, Vol. 22, 1975, p. 581.

B. Chen and N. Todreas, "Prediction of the Coolant Temperature Field in a Breeder Reactor Including Interassembly Heat Transfer," Nuclear Engineering and Design 35, (1975) 423-440 (Included as Appendix to Quarterly Progress Report, COO-2245-23).

R. Bennett and M.W. Golay, "Interferometric Investigation of Turbulently Fluctuating Temperature in an LMFBR Outlet Plenum Geometry," Accepted for the ASME Winter Annual Meeting, Dec., 1976, (Included as Appendix in Quarterly Progress Report, COO-2245-30).

B.B. Mikic, E.U. Khan, N.E. Todreas, "An Approximate Method for Predicting Temperature Distribution in Wire Wrapped Fuel Assemblies of a Liquid Metal Fast Breeder Reactor," Mech. Res. Comm., Vol. 3, 353-360 (1976).

Reports Issued Under this Contract

C. Papers and Summaries (Continued)

L. Wolf, R. Karimi, I.Y. Kim, C.N. Wong, M.K, Yeung "2-D Thermoelastic Analysis of LMFBR Fuel Rod Claddings," Paper C4/d, 4th International Conf. Structural Mechanics in Reactor Technology, San Francisco, August 1977.

M. Yeung, L. Wolf, "Effective Conduction Mixing Lengths for Subchannel Analysis of Finite Hexagonal LMFBR Bundles," ANS Meeting, New York, June 1977.

C. Chiu and N. Todreas, "Flow Split Measurements In An LMFBR Radial Blanket Assembly," ANS Meeting, New York, June 1977.

Commencing with report COO-2245-30, a new task, TASK IV, which has been added to the contract, was reported. This TASK IV and TASK IID differ in that TASK IV is initially concentrated on thermal analyses using slug and laminar velocity profiles while TASK IID is concentrated on hydrodynamic analyses of turbulent velocity fields.

COOLANT MIXING IN LMFBR ROD BUNDLES AND OUTLET PLENUM MIXING TRANSIENTS

Contract AT(11-1)-2245

Quarterly Progress Report

The work of this contract has been divided into the following Tasks:

TASK I: BUNDLE GEOMETRY (WRAPPED AND BARE RODS)

- TASK IA: Assessment of Available Data
- TASK IB: Experimental Bundle Water Mixing Investigation
- TASK IC: Experimental Bundle Peripheral Velocity Measurements (Laser Anemometer)
- TASK ID: Analytic Model Development - Bundles

TASK II: SUBCHANNEL GEOMETRY (BARE RODS)

- TASK IIA: Assessment of Available Data
- TASK IIB: Experimental Subchannel Water Mixing Investigation
- TASK IIC: Experimental Subchannel Local Parameter Measurements (Laser Anemometer)
- TASK IID: Analytic Model Development - Subchannels

TASK III: LMFBR OUTLET PLENUM FLOW MIXING

- TASK IIIA: Analytical and Experimental Investigation of Velocity and Temperature Fields

TASK IV: THEORETICAL DETERMINATION OF LOCAL TEMPERATURE FIELDS IN LMFBR FUEL ROD BUNDLES

TASK I: BUNDLE GEOMETRY (WRAPPED AND BARE RODS)

TASK IA: Assessment of Available Data and Codes (Kerry Basehore)

No work was performed this quarter.

TASK IB.2 Experimental Bundle Water Mixing Investigation

Repeat of Laminar and Transition Flow - 61 Pin Fuel Mixing Experiments (Stuart Glazer)

During the previous quarter, a variant of the isokinetic sampling technique used by C. Chiu with the 61 pin blanket bundle, was developed to handle differences in construction of the fuel and blanket bundles. The tests were not satisfactorily completed due to unacceptable sensitivity to the particular measurements taken and non repeatability of volumetric flow measurements in individual subchannels. Minor variations in flow exiting from the same subchannel was observed, and was postulated to occur due to the relative "looseness" of the pins within the duct assembly. The ratio of nominal pin to pin centerline distance, to pin diameter (P/d) is much larger for the fuel bundle than for the blanket bundle (1.24 versus 1.067) so that more significant rod bowing and rod repositioning may occur at the exit plane, particularly due to the influence of insertion and removal of the isokinetic sampling probe. Since flow split measurements are sensitive to the "spread" of the fuel pins, and since the work of Chiu [1] indicated relatively uniform flow over each of the interior, edge and corner regions, it was decided to drop the current plans for flow split measurement on a subchannel by subchannel basis. The sampler tube has been redesigned to record the axial volumetric flowrate from 1/6 of the interior subchannels at once. It has also been found that the analysis techniques reported by Chiu in [1] are applicable to the current situation, so that these will be used. The new sampler tube has been designed and fabricated, and is currently being used to collect axial flowsplit data as a function of Reynolds number. Flow split tests are expected to be completed shortly.

Preparations have also been made for the conduct of the 61 pin fuel bundle salt mixing tests. A new complete set of 126 salt conductivity probes have been wired to the standard 16 pin connectors to facilitate connection to the Real Time Data Acquisition System. Three injection rods previously

fabricated, were wrapped with the spacer wire, and will be installed in the 61 pin fuel bundle upon completion of the current series of flowsplit tests. At that time, the electrical conductivity probes will be platinized and inserted into the flow separator. Salt mixing tests are expected to be run and completed during the current quarter.

The report on the Real Time Data Acquisition System has been nearly completed, and will be issued during the current quarter as [2].

TASK IB.3 217 Pin Mixing Experiments (Stuart Glazer)

During the past quarter, a version of the SUPERENERGY code was used to determine the number of subchannels at the exit plane of the 5 foot test section which will be expected to contain higher than background salt concentrations as a result of salt tracer injection at predetermined positions. Although the results are incomplete, it is currently believed that less than 1/2 the 438 subchannels in the 217 pin bundle need be instrumented. Previous probe manufacturing efforts have resulted in a stock of approximately 200 partially completed probes. An appropriate number of these probes will be finished pending final results of the study. Operation of the 217 pin mixing tests must necessarily wait until completion of the 61 pin bundle salt mixing tests, as plans call for the centerless grinding of 1 or 2 of the injection rods built for the 61 pin test bundle (pin dia = .250") to the size of the prototypical pins (pin dia = .230") in the 217 pin bundle. Injection rod fabrication costs will therefore be held to a minimum.

TASK IB.4 61 Pin Blanket Bundle Expeirments (Chong Chiu)

During this quarter, much work has been devoted toward the mixing experiments of the alternating wire wrapped blanket assembly and the static pressure drop measurements of the 2" lead wire wrapped blanket bundle.

The mixing experiments of the alternating wire wrapped bundle are performed by measuring the salt concentration map at the bundle exit with different salt injection depth for a given Re. The experimental condition of these data are summarized in Table 1. The purpose of this study is to understand the salt transport process at different distances from the position where the saline solution is injected from the

injection rod. The salt concentration maps at different Re for a given injection depth are used to calibrate the input function FPRCE of COBRA-IIIC computer code. By doing so, we are able to determine the subchannel coolant temperature and peripheral duct temperature distribution of a typical heated alternating wire wrapped blanket assembly by this calibrated computer code. The results from this COBRA IIIC study will be compared with the subchannel coolant temperatures and duct temperature distribution of an in-phase wire wrapped blanket assembly under the same operating condition predicted by SUPERENERGY. From this comparison we believe we can determine the advantages and disadvantages of the alternating wire wrapped assembly versus the conventional in-phase assembly.

The static pressure data of the 2" lead blanket assembly are obtained in two different kinds of subchannels. One is an edge subchannel, the other is an interior subchannel. Injection rods are used in both subchannels to obtain static pressure data at two different depths, i.e., 16 inches and 22.5 inches from the bundle exit.

The static pressure data are presented in Figs. 1 and 2 for edge subchannel and interior subchannel respectively. The pressure drop data for these two subchannels are presented in Figs. 3 and 4. Since the pressure drop data for a given Re of these two subchannels are identical, the bundle friction factor can be determined by assuming uniform pressure drop over a certain bundle axial distance. The resulting friction factor is plotted versus Re as shwon in Fig. 5.

TASK IC: Experimental Bundle Peripheral Velocity Measurements (Laser Anemometer)

No work was performed this quarter.

TASK ID: Analytic Model Development - Bundles (Kerry Basehore)

Our model development efforts have been substantial in the past. To assist the reader in identifying our published material on these efforts and the associated codes, this new summary format has been added to our progress reports

Summary of Existing ENERGY Model and Related References

Report numbers listed refer to those report titles included in the complete listing at the beginning of this progress report.

I. ENERGY Physical Model Development

a. General

COO-2245-12TR
COO-2245-16TR

II. Code Listing and Input Description

a. Summary of Capabilities

COO-2245-28, pp. 16-17

b. ENERGY I, II, III

COO-2245-17TR
COO-2245-18TR, Revision 1

c. SUPERENERGY

COO-2245-20TR, Revision 1

III. Empirical Input Parameters, ϵ^* and C

a. Khan correlation, fuel bundle

COO-2245-16TR, pp. 67-69 or
COO-2245-17TR

b. Blanket bundle

COO-2245-34, pp. 3
COO-2245-45TR (not released)

c. Conversion factors between porous and subchannel models

COO-2245-16TR, Appendix 4
COO-2245-34, pp. 4-7 (graphs)

IV. Model-Data Comparison

a. General

COO-2245-12TR
COO-2245-16TR
COO-2245-21TR

b. ANL XX07

COO-2245-33TR

c. ORNL FPM-2A

COO-2245-28 pp. 2-3
COO-2245-32TR
COO-2245-46TR

V. Model Comparison with other Codes

a. General

COO-2245-16TR

b. COBRA

COO-2245-32TR

c. TRITON - COTEC

COO-2245-31, pp. 3-4

VI. Model Additions and Improvements

a. G^{*}_{rc} Criteria for Forced Convection

COO-2245-16TR, pp. 76-90 (derivation)
COO-2245-28 pp. 14 (coded version)

b. Stability - ENERGY I

COO-2245-16TR, Appendix 3

c. Stability - SUPERENERGY

COO-2245-31, pp. 9-14
COO-2245-32TR

d. Interassembly gap conduction model

COO-2245-20TR, Revision 1 (original model)
COO-2245-33TR (resistance model)

e. Variable swirl flow model

COO-2245-34, pp. 8-10
COO-2245-38, pp. 4
COO-2245-46TR

VII. Codes and Models under Development

a. Secondary control assembly model

COO-2245-38, pp. 5
COO-2245-47TR (not released)

b. Transient SUPERENERGY

COO-2245-31, pp. 14-22
COO-2245-34, pp. 11-41
COO-2245-38, pp. 5
COO-2245-35TR

c. A complete summary of code developments is shown in Table 2.

TASK ID.1 Steady State SUPERENERGY (Kerry Basehore)

1. Variable Swirl Flow Model

A report assessing the practicality and worth of introducing a variable swirl flow model into the ENERGY codes, using the data reduction and model implementation schemes documented in previous progress reports [3,4], has been written [5] and is now in the distribution phase. The conclusions reached were as follows:

i) The variable swirl model will give temperature predictions close to the constant swirl model for axial heights above one wire wrap lead length and for power distributions that are not unrealistically skewed. At relatively large axial heights local fluctuations of opposite sign caused by variable transverse flow tend to compensate. The transverse velocity is less important in bundles that are not highly power skewed.

ii) The mass imbalance effects in the swirl model used to date are noticeable. If a permanent implementation of the variable swirl flow model is attempted, a method of providing a mass balance will have to be done carefully, so as not to destroy the simplicity and physical nature of the ENERGY model.

iii) The differences between the variable and constant swirl models are generally insignificant compared to bundle tolerance effects. It is recommended that the variable swirl model not be used until it is found that variations in predictions between it and the constant swirl model are equal to variations due to fabrication tolerances.

2. GE Secondary Control Assembly

A computer model of the thermal hydraulic behavior of the Clinch River secondary control assembly has been completed. The computer program uses a semi-analytical method to model the counterflow section and explicit SUPERENERGY type equations to model the poison control section. A simplified sample problem shows that the results from the counterflow section of the program have excellent agreement with the purely analytical solution. Boundary condition interfacing with SUPERENERGY has been achieved and works well. Documentation on modeling is now being completed and will be released in topical report form next quarter.

TASK ID.2 Analytical Model Development - Transient SUPERENERGY (Stuart Glazer)

As reported in [3], two versions of the transient SUPERENERGY code are under development: a detailed single assembly version capable of analyzing flow, power, and inlet temperature transients at a subchannel level for bundles up to 217 pins, and a multiassembly version which represents each bundle as a 7 pin assembly for the purpose of determination of interassembly heat transfer. The multiassembly version will be desinged to permit up to 39 assemblies (a 1/12 core sector) to be coupled.

Current plans call for the use of the two codes either independently or in a cascade technique. In the cascade technique the multiassembly lumped version is first run to determine approximate interassembly heat transfer during the transient. These heat fluxes will be stored on magnetic tape and used later by the single assembly version as boundary conditions on the six bundle faces throughout the transient.

An effort has been made to develop a base of commonality and interchangeability between several subroutines in these two codes, as well as with the steady state codes being developed by K. Basehore. Division of work has been made, and a coordinated effort of code development is under way. Currently, the author has expended most effort on the development of the detailed single bundle code, with emphasis on development of common data structures and internal organizations between the single and multiassembly code versions. Completion of both codes is expected during the current quarter.

REFERENCES

[1] C. Chiu and N. Todreas, "Development of a Technique for Subchannel Flow Rate Measurements in LMFBR Wire Wrapped Assemblies," COO-2245-39TR, MIT, July 1977.

[2] S. Glazer, C. Chiu, N. Todreas, "Collection and Evaluation of Salt Mixing Data with the Real Time Data Acquisition System," Topical Report, COO-2245-36TR, MIT, April 1977

[3] N.E. Todreas, M.W. Golay, L. Wolf, "Coolant Mixing in LMFBR Rod Bundles and Outlet Mixing Transients," Progress Report, COO-2245-34, MIT, November 1976.

[4] N. Todreas, M. Golay, L. Wolf, "Coolant Mixing in LMFBR Rod Bundles and Outlet Mixing Transients," Progress Report, COO-2245-38, MIT, February 1977

[5] K.L. Basehore, N.E. Todreas, "Assessment of the Need to Incorporate the Variable Swirl Model in the ENERGY Code," COO-2245-46TR, MIT, July 1977

TABLE 1

TEST RUN NO. AND INJECTION DEPTH

Center Injection Subchannel		Edge Injection Subchannel (180° Out-of-Phase W.W)		Edge Injection Subchannel (In-Phase W.W.)	
Test Run No.	Injection Depth	Test Run No.	Injection Depth	Test Run No.	Injection Depth
16	16.0"	33	13.5"	47	13.5"
17	16.5"	34	14.5"	48	14.0"
18	17.0"	35	15.5"	49	14.5"
19	17.5"	36	16.5"	50	15.0"
20	18.0"	37	17.5"	51	15.5"
21	19.0"	38	18.0"	52	16.0"
22	19.5"	39	18.5"	53	16.5"
23	20.0"	40	19.0"	54	17.5"
24	20.5"	41	19.5"	55	18.0"
25	21.0"	42	20.0"	56	18.5"
26	22.0"	43	23.0"	57	19.0"
27	22.5"	44	23.5"	58	19.5"
28	23.0"	45	24.0"	59	20.0"
29	23.5"	46	25.0"	60	20.5"
30	24.5"			61	21.0"
31	25.5"			62	21.5"
32	26.5"			63	22.0"
				64	23.0"
				65	24.0"
				66	25.0"

TABLE 2

ENERGY SERIES CODE DEVELOPMENT

Code	Options	Status	Documentation	Author	Comment
Steady State-Forced Convection			COO-2245-XXX		
ENERGY I	I-Porous Body Is-Subchannel Model	Superceded by ENERGY I, Rev. 1	18TR May, 1975	Khan	
ENERGY I, Rev. 1	I-Porous Body Is-Subchannel Model	Superceded by ENERGY I, Rev. 2	18TR, Rev. 1 July, 1976	Basehore	Sample Program changed
ENERGY I, Rev. 2	I-Porous Body Is-Subchannel Model	Latest of its class	To be assigned	Basehore	1) Reprogrammed version of Rev. 1 but with adiabatic wall condition. 2) Use in place of SUPERENERGY II (low storage) application and for direct enthalpy calculations.
SUPERENERGY	Subchannel Model only	Superceded by SUPERENERGY, Rev. 1	20TR May, 1975	Basehore	
SUPERENERGY, Rev. 1	Subchannel Model only	Superceded by SUPERENERGY, Rev. 2	20TR, Rev. 1 December, 1976		
SUPERENERGY, Rev. 2	Porous Body Model and Subchannel Model	Latest of its class	To be assigned	Basehore	Use for core segment (can handle with extra bypass region) or single assembly with wall temperature or heat flux condition

TABLE 2 (Continued)

ENERGY SERIRES CODE DEVELOPMENT

Code	Options	Status	Documentation	Author	Comment
Transient-Forced Convection					
TRANSENERGY-S	Single Assembly-Porous Body Model	Latest of its class	To be assigned	Glazer	
TRANSENERGY-C	Core Segment-Fixed Nodal Layout	Latest of its class	To be assigned	Glazer	
Steady State-Mixed Convection					
ENERGY II	Porous Body Model	Superceded by ENERGY II, Rev. 1	18TR May, 1975	Khan	Neglects convective terms in axial momentum equation and lateral energy convection in energy equation.
ENERGY II, Rev. 1	Porous Body Model	Latest of its class	18TR, Rev. 1 July, 1976	Basehore	Sample problem changed.
ENERGY III	Porous Body Model	Superceded by ENERGY III, Rev. 1	18TR May, 1975	Khan	
ENERGY III, Rev. 1	Porous Body Model	Latest of its class	18TR, Rev. 1 July, 1976	Basehore	

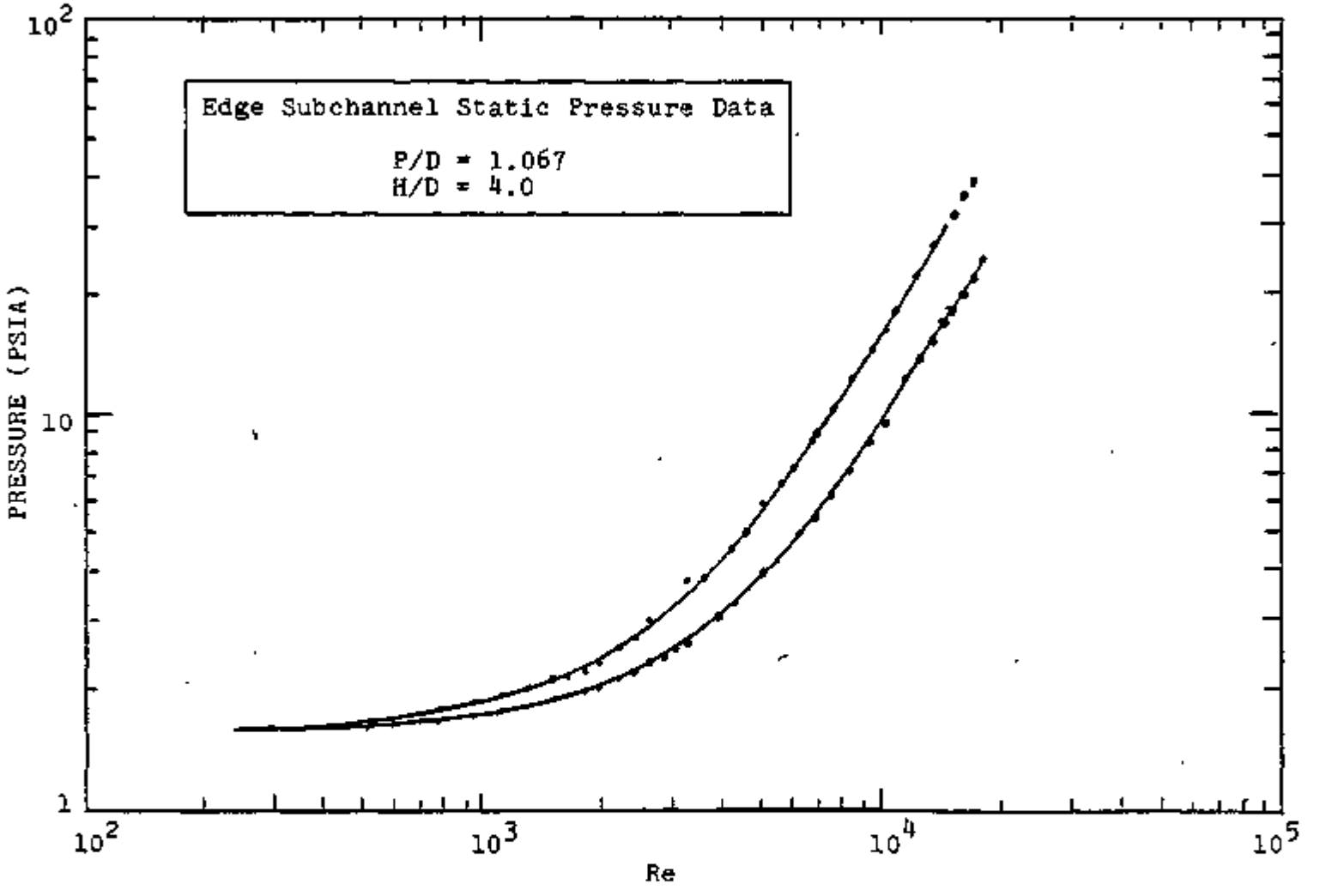

Figure 1: Edge Injection Tube Pressur vs Reynolds Number

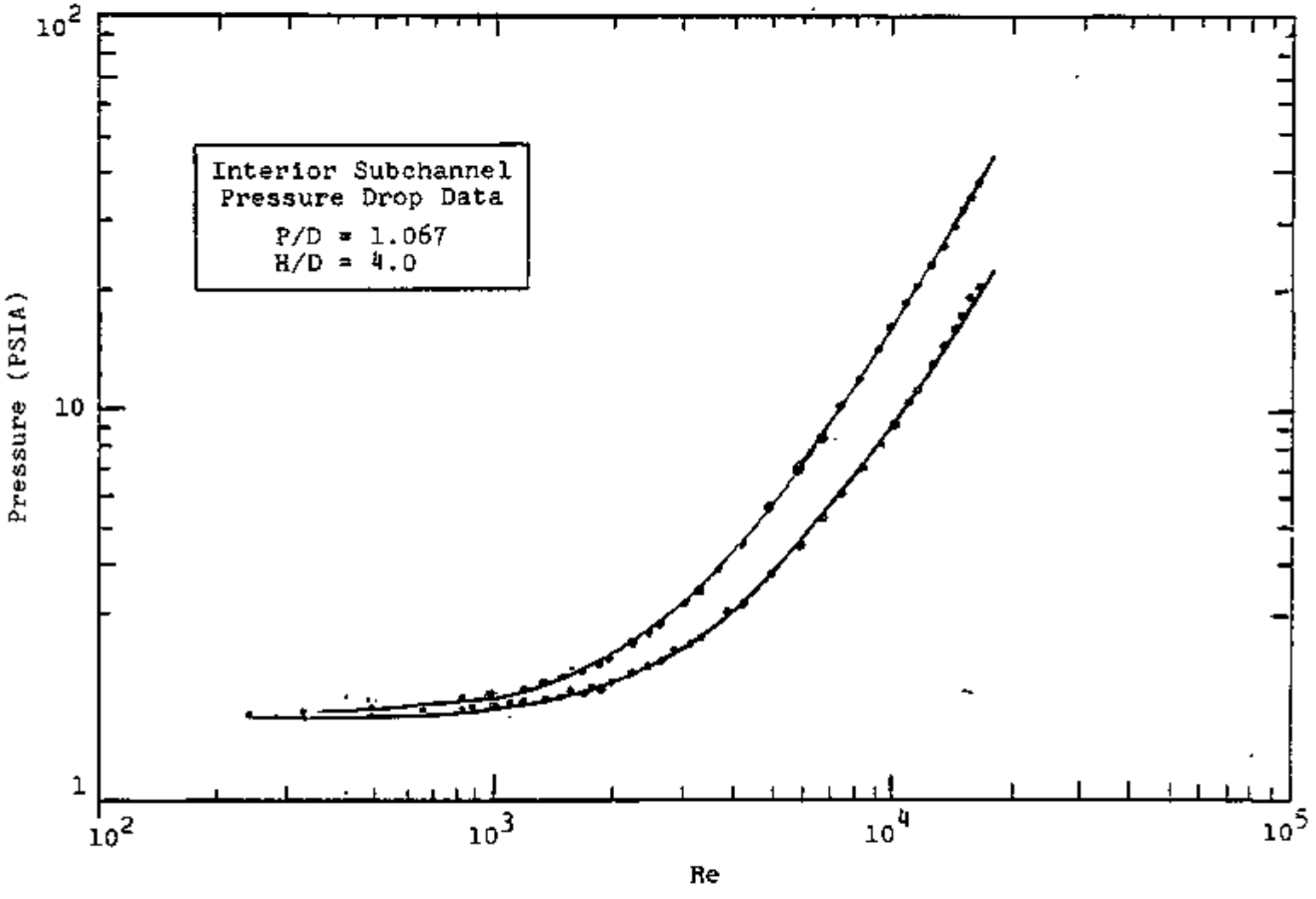

Figure 2: Center Injection Tube Pressure vs Reynolds Number

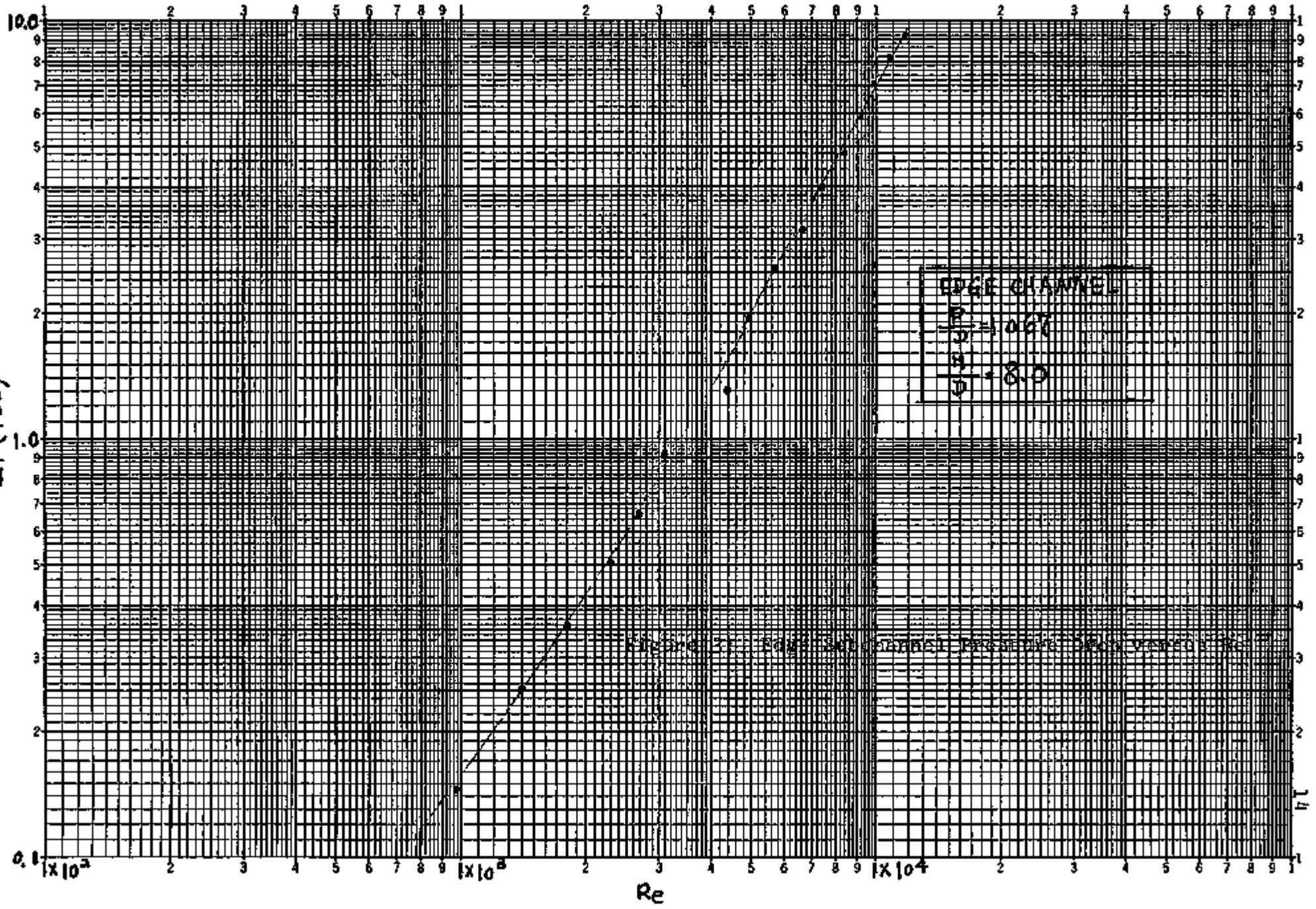

Figure 3: Edge Channel Pressure Drop versus Re

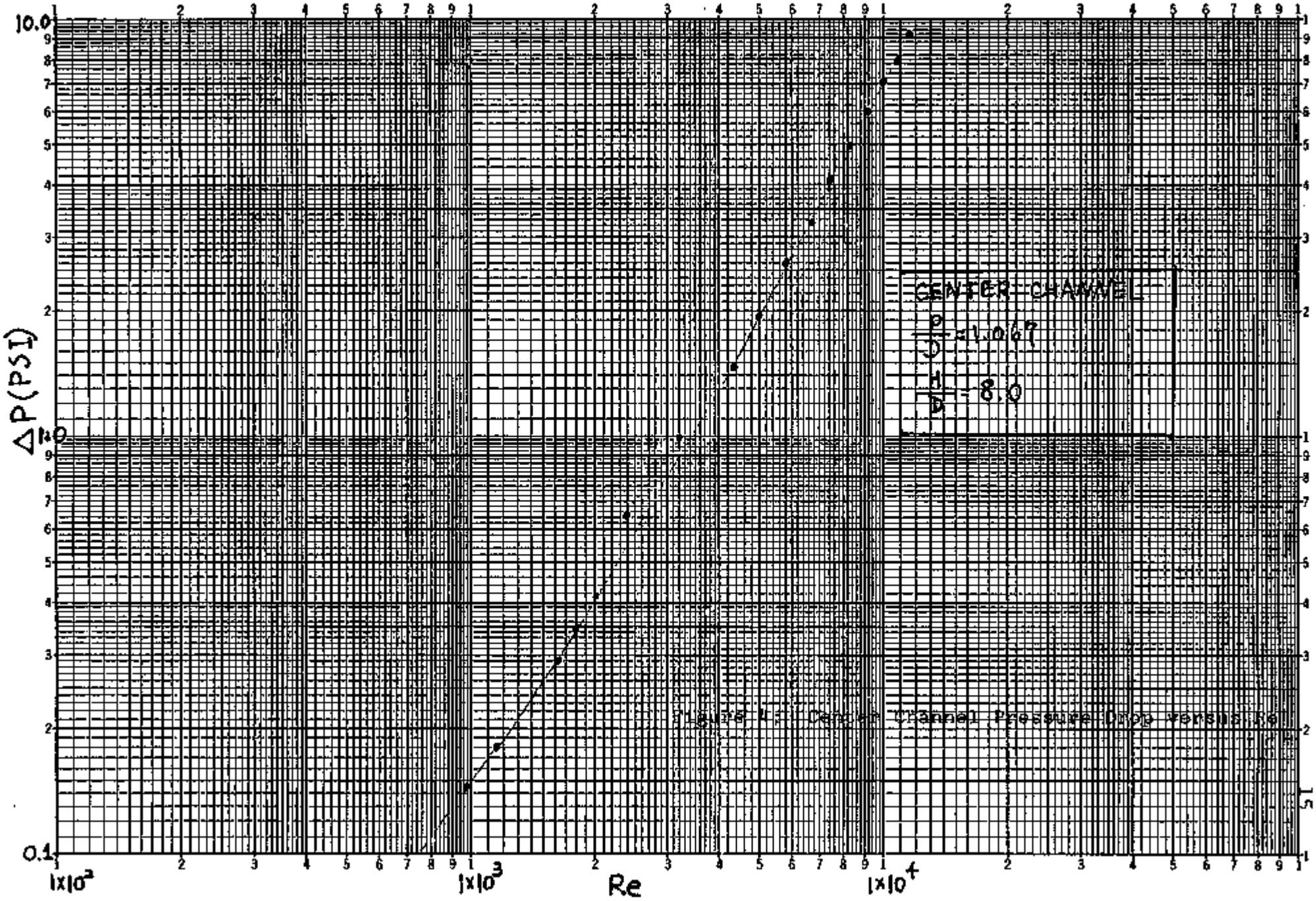

Figure 4: Center Channel Pressure Drop versus Re

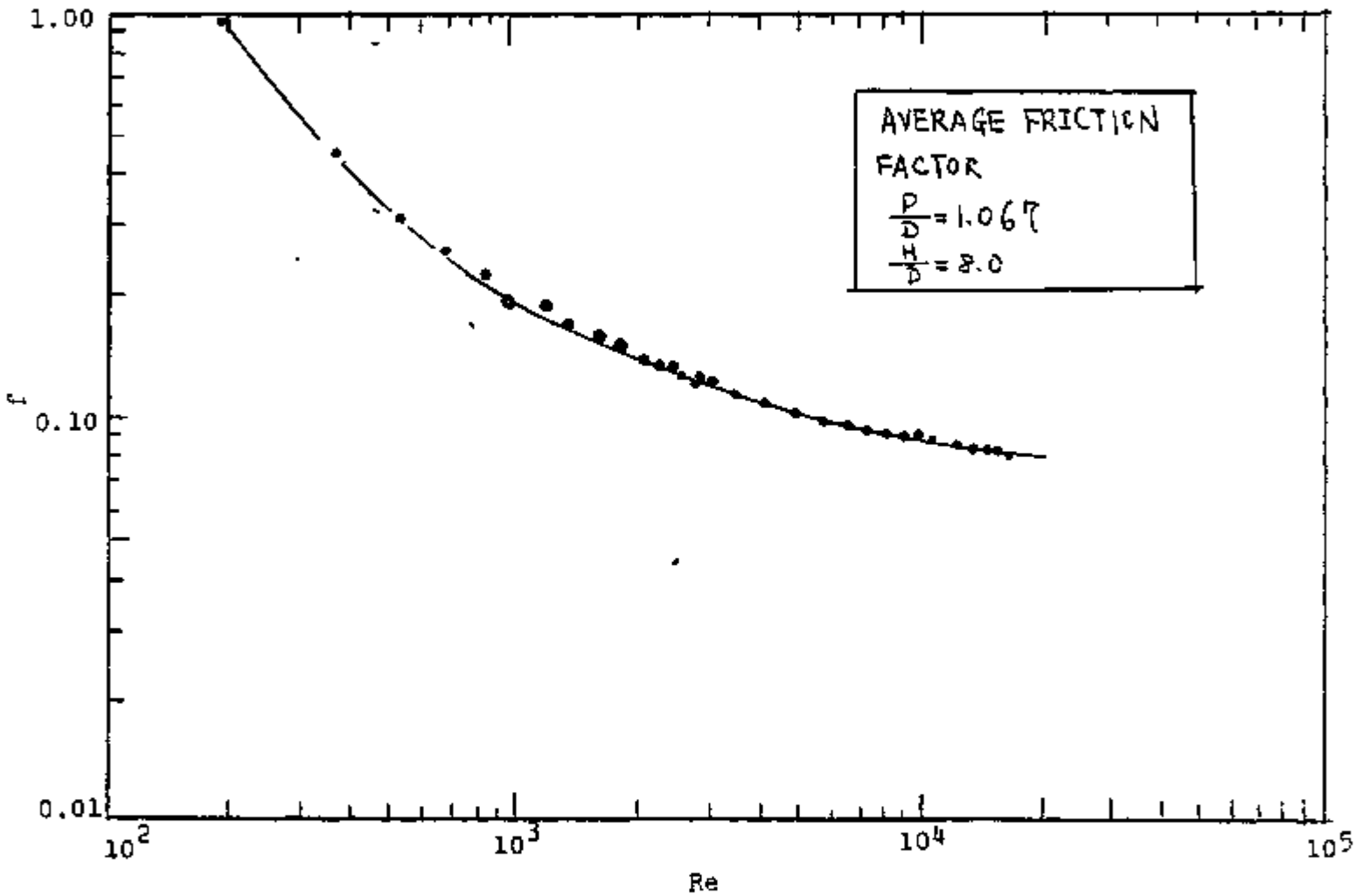

Figure 5: Average Pressure Drop Friction Factor vs Reynolds Number

TASK II: SUBCHANNEL GEOMETRY (BARE RODS)

TASK IIA: Assessment of Available Data

No work performed on this task this quarter.

TASK IIB: Experimental Subchannel Water Mixing Investigation (Joseph M. Kelly)

Work has been completed and reporte in COO-2245-45TR.

TASK IIC: Experimental Subchannel Local Parameter Measurements (John Bartzis)

A 2-channel Laser Doppler Anemometer working on the Reference mode with forward scattering was used to perform the measurements in a simulated interior subchannel of a triangular rod array with P/D=1.124. Experimental measurements of the distribution of axial velocity, turbulent axial velocity, turbulent kinetic energy and radial Reynolds stresses were performed in the developing and fully developed regions. All measurements have been completed and will be reported in COO-2245-48TR.

TASK IIC.1 Wall Shear Stress Measurements (Mohammed Fakory)

In this period the measurements were completed. The experiment was performed at different Reynolds number in the same test section geometry (P/D = 1.1, D = 1.5 inches). Table 1 summarizes the measurements and conditions under which they were performed.

We are now reviewing the data. Conclusions drawn so far are as follows:

1. The wall shear stress is a monotonical function of θ (azimuthal angle along the rod periphery), within $0 < \theta < 30$ degrees. The maximum value of the wall shear stress occurs at $\theta = 30$ degrees. At $\theta = 0$ and $\theta = 30$ degrees the distribution of wall shear stress is symmetrical with respect to $\theta = 0$ and $\theta = 30$ degrees provided that there is good symmetry between the neighboring subchannels.

2. At Reynolds number equal to 4,000 the flow regime is not stable but is between laminar and turbulent.

3. There is no effects of secondary flow in the region very close to the wall.

4. The wall shear stress is not skewed from the rod axis by the effect of secondary flow.

5. The friction factor calculated from the average wall shear stress distribution (f_s) is less than the friction factor resulting from the measured pressure drop at $\theta = 0$ degree (f). The f_s can be calculated using the equivalent annular zone formula or the round tube friction factor multiplied by a coefficient.

6. The static pressure (p_s) is not uniform around the subchannel periphery and decreases as θ increases from zero to 30 degrees.

TASK IID: Analytical Model Development - Subchannels
(John Bartzis)

The thesis in this area has been completed and will be issued as Report COO-2245-48TR which will include the measurements of TASK IIC.

In the present work a 2-equation turbulence model - a strong candidate for analyzing actual three dimensional turbulent flows - has been used to predict fully developed flow of infinite bare rod bundle of various aspect ratios (P/D). The model has been modified to take into account anisotropic effects of eddy viscosity.

Secondary flow calculations have been also performed although the model seems to be too rough to predict the secondary flow corrently. Heat transfer calcualtions have been performed to confirm the importance of anisotropic viscosity in temperature predictions.

All numerical calculations for flow and heat have been performed by two computer codes developed in the present work which were based on the TEACH code.

Comparisons between the analytical results and the results of this experiment as well as other experimental data in rod bundle array available in literature were made. The predictions are in good agreement with the results for the high Reynolds numbers.

Experiment Number	Test Section	Flow Source	Probe Model	$Rex10^{-3}$	Measured Parameters
1	Final design	Blower	3	4.15	$\tau_w(\theta), \bar{\tau}_w, \frac{\tau_w(\theta)}{\bar{\tau}_w}, f_s, f, P_s(\theta)$, RMS
2	Final design	Blower	3	4.14	$\tau_w(\theta), \bar{\tau}_w, \frac{\tau_w(\theta)}{\bar{\tau}_w}, f_s, f, P_s(\theta)$, RMS
3	Final design	Blower	2	9.11	$\tau_w(\theta), \bar{\tau}_w, \frac{\tau_w(\theta)}{\bar{\tau}_w}, f_s, f, P_s(\theta)$
4	+Intermediate design	Compressor (Regulator Valves)	2	9.52	$\tau_w(\theta), \bar{\tau}_w, \frac{\tau_w(\theta)}{\bar{\tau}_w}, f_s, f, P_s(0), P_s(30)$
5	+Final design	Blower	2	10.47	$\tau_w(\theta), \bar{\tau}_w, \frac{\tau_w(\theta)}{\bar{\tau}_w}, f_s, f, P_s(\theta)$
6	Final design	Compressor (Continuously)	3	18.89	$\tau_w(\theta), \bar{\tau}_w, \frac{\tau_w(\theta)}{\bar{\tau}_w}, f_s, f$, RMS
7	Final design	Compressor (Continuously)	3	36.17	$\tau_w(\theta), \bar{\tau}_w, \frac{\tau_w(\theta)}{\bar{\tau}_w}, f_s, f, P_s(\theta)$, RMS

TABLE 1

List of Test Conditions and Measured Parameters

+ These results are unreliable.

TASK III. LMFBR OUTLET PLENUM FLOW MIXING

III.A. Steady State Velocity Field Measurements (Yi Bin Chen)

The steady state outlet plenum velocity field measurements and analysis have been completed. The results are summarized in the project report Coolant Mixing in the LMFBR Outlet Plenum, COO-2245-44TR by Yi Bin Chen and Michael W. Golay (transmitted separately), and in the paper Validation of Turbulence Models for LMFBR Outlet Plenum Flows by Yi Bin Chen and Michael W. Golay (Appendix III.A) which will be presented at the 1977 National Heat Transfer Conference. The major conclusions of the work are that the VARR-II turbulence model is adequate for design calculations in geometries having significant length scales of different magnitude (as with the FFTF plenum). However, in cases having several length scales of the same magnitude (as with the CRBR plenum), the model fails to provide results which are accurate even qualitatively. In the latter case, no amount of model parameter adjustment was adequate to improve experimental and theoretical agreement significantly. It was also found that detailed knowledge of the inlet flow mean flow and turbulence fields is required for accurate calculations.

III.B. Combined Temperature and Velocity Measurements (Vincent P. Manno)

During the past quarter, the fluidized bed seed injection system discussed in the previous progress report was constructed and introduced into the flow circuit. The preliminary testing of this system has been very promising and it seems that this mode of seed injection will prove successful. With the flow now seeded with particles, the question arose as to whether the presence of the particles would interfere with the interferometric temperature measurement. Therefore, the temperature measurement system was tested first with and then without flow seeding, and no appreciable difference was found. The interference patterns observed during both modes of operation were identical in both intensity and configuration. In addition to the seeding system, the new test cell also described in the last report was installed into the experiment.

The next task undertaken was the transfer of the remainder of the LDA equipment to the experimental area. The components which were introduced were: a photomultiplier and its associated high voltage unit, the Doppler frequency tracker and power unit, the exciter unit for the LDA frequency shifting Bragg cell, turbulence processor, and RMS (root mean squared) voltmeters.

At present the LDA system has been completely installed and initial alignment and adjustments have begun. The present efforts are centered around finding the optimum flow seeding rate and equipment settings so as to attain the best velocity data. Once this is established, actual measurements will begin. The first measurements to be taken will allow evaluation of the average velocity signal ($\bar{U}$) and mean temperature signal ($\bar{T}$) at prescribed measurement stations in the flow. As was outlined in a previous progress report, the product of these two quantities must be subtracted from the measurement system output in order to attain a value for $\langle u'T' \rangle$ at the various positions, since $\langle u'T' \rangle$ is the crucial quantity for evaluation of the eddy diffusivity of heat. The efforts of the next quarter will therefore center around aligning and adjusting the completed integrated system and then turn to data acquisition.

an ASME publication

$3.00 PER COPY
$1.50 TO ASME MEMBERS

Validation of Turbulence Models for LMFBR Outlet Plenum Flows

Y. B. CHEN

Graduate Student
Student Mem. ASME

M. W. GOLAY

Associate Professor of Nuclear Engineering
Mem. ASME

Massachusetts Institute of Technology,
Cambridge, Mass.

Small scale experiments involving water flows are used to provide mean flow and turbulence field data for LMFBR outlet plenum flows. Measurements are performed at Reynolds number (Re) values of 33,000 and 70,000 in a 1/15-scale FFTF geometry and at Re = 35,000 in a 3/80-scale CRBR geometry. The experimental behavior is predicted using two different two-equation turbulence model computer programs, TEACH-T and VARR-II. It is found that the qualitative nature of the flow field within the plenum depends strongly upon the distribution of the mean inlet flow field, importantly also upon the degree of inlet turbulence, and also upon the turbulent momentum exchange model used in the calculations. It is found in the FFTF geometry that the TEACH-T predictions agree well with the experiments, while the agreement of the VARR-II prediction is poorer, and in the CRBR geometry neither code provides a good prediction of the observed behavior.

Contributed by the Heat Transfer Division of The American Society of Mechanical Engineers for presentation at the AIChE-ASME Heat Transfer Conference, Salt Lake City, Utah August 15–17, 1977. Manuscript received at ASME Headquarters April 12, 1977.

Copies will be available until May 1, 1978.

UNITED ENGINEERING CENTER, 345 EAST 47th STREET, NEW YORK, N.Y. 10017

Validation of Turbulence Models for LMFBR Outlet Plenum Flows

Y. B. CHEN M. W. GOLAY

ABSTRACT

Small scale experiments involving water flows are used to provide mean flow and turbulence field data for LMFBR outlet plenum flows. Measurements are performed at Reynolds number (Re) values of 33000 and 70000 in a 1/15 - scale FFTF geometry and at Re = 35000 in a 3/80-scale CRBR geometry. The experimental behavior is predicted using two different two-equation turbulence model computer programs, TEACH-T and VARR-II. It is found that the qualitative nature of the flow field within the plenum depends strongly upon the distribution of the mean inlet flow field, importantly also upon the degree of inlet turbulence, and also upon the turbulent momentum exchange model used in the calculations. It is found in the FFTF geometry that the TEACH-T predictions agree well with the experiments, while the agreement of the VARR-II prediction is poorer, and in the CRBR geometry neither code provides a good prediction of the observed behavior.

NOMENCLATURE

C_1, C_2, C_μ	constants appearing in transport equations of TEACH-T
g_x, g_z	gravitational force in x and z direction
I	internal energy
k	turbulence kinetic energy, $\frac{1}{2}\overline{u_i'^2}$
p	pressure
q	amount of heat transfer from boundary to the surrounding fluid
Re	Reynolds number, defined with respect to inlet duct width
r	radial coordinate
t	time
u	mean velocity in r direction
$\overline{u'v'}$	kinematic shear stress
$\overline{u_i'u_j'}$	kinematic Reynolds stresses
u_i, u_j	mean velocity components
u_i', u_j'	fluctuating velocity components
v	mean velocity in z direction
x_i, x_j	general cartesian coordinate
σ	turbulent kinematic viscosity
σ_k σ_ε	effective turbulent Prandtl number for transport of k and ε
ρ	density of the fluid
ρ_o	reference density
Γ, Γ_1, α	constants appearing in transport equations of VARR-II
γ_T	reciprocal of the turbulent Prandtl number
ν	kinematic viscosity
μ	molecular viscosity
μ_t	turbulent viscosity
ε	turbulent energy dissipation rate

INTRODUCTION

In the Liquid Metal-cooled Fast Breeder Reactor (LMFBR), sodium is used as coolant to remove heat from the reactor core. Since sodium is a good heat transfer medium and has low heat capacity, the temperature difference between inlet and outlet of the core is much higher than that of the current design light water reactor (LWR). A typical value for this temperature rise is approximately 300 F. During a reactor scram with (or without) flow coastdown, the cold sodium will issue from the reactor core, and will mix with hot sodium which had previously filled the reactor outlet plenum. Predicting the transient thermal response of the sodium in the outlet plenum is an important problem, since this thermal regime will dictate the thermal fatigue environment for the outlet nozzles, instrument trees, and other mechanical components which will be exposed to the reactor coolant flow. Two-equation turbulence model calculations are being used to predict the thermal histories which such components will experience. Thus, it is necessary, in order to insure the adequacy of the design of these components, that the design numerical simulations be both accurate and economical. Experimental verification of the accuracy of the resulting predictions is an essential component of that insurance.

The detailed analytical treatment of the coolant mixing in the outlet plenum is very difficult due to the complex nature of the resulting turbulent flow. The Navier-Stokes equation cannot be solved numerically because of small scale of turbulence, and due to the limited storage capacity and speed of existing computers. Therefore, most of the problems in the turbulent flow are solved by using the time-averaged Navier-Stokes equations (or Reynolds equation). Due to the nonlinearity of the Navier-Stokes equations, one additional term, known as Reynolds stress, appears in the Reynolds equation. Much of the attention has been concentrated on how to model this parameter in terms of known quantities. This is the so-called turbulence

model approach. In general the LMFBR outlet plenum will display a recirculating flow pattern. The simplest model (e.g., Prandtl's mixing length theory) has been found to be inadequate in providing accurate predictions of this behavior (1). Therefore current design work has adopted the use of the two-equation turbulence model. This decision is based on the need for accuracy and for reasonably short computation times.

ANALYTIC TOOLS

In our work two computer codes, namely TEACH-T (2) and VARR-II (3) are used. TEACH-T is a steady-state two-dimensional code which adopts turbulent kinetic energy and turbulent energy dissipation as two additional dependent variables. Turbulent kinetic energy and turbulent energy dissipation are defined as

$$\frac{1}{2}\overline{u_i'^2} \quad \text{and} \quad \nu\overline{\left(\frac{\partial u_i'}{\partial x_j}\right)^2}$$

(both in tensor form) respectively. VARR-II is a time-dependent two-dimensional thermal hydraulic code. Different from TEACH-T, it solves turbulent kinetic energy and turbulent kinematic viscosity conservation equations in differential form. In addition, a heat conservation equation is also incorporated into the code for temperature prediction, and in order to provide buoyant force feedback to the vertical momentum equation. (See the Appendix for a more complete discussion of the two codes.) The code TEACH-T has been modified to calculate flows in the reactor plenum geometry, and has been used to generate a prediction of the flows which would be observed in the validation experiments of this work. The code VARR-II is currently in use as a design tool in the U.S. LMFBR demonstration reactor (Clinch River) program. Its predictions have not been verified experimentally in the flow geometry of interest. It is also being used in this work to predict the flow in the experimental test cell. Thus, by intercomparison of the results from these two competing turbulence model codes and the observed experimental data, one may identify sources of error in the predictions and make appropriate improvements in the turbulence models for the outlet plenum application.

EXPERIMENTS

In the experiments, small-scale Cartesian geometry test models of a diametrical section of the prototypic outlet plenum geometries are used. The experiments consist of measurements of appropriate turbulence model parameters in steady-state water flows. These data are then compared to predictions of the behavior of the experiment by each of the two-equation turbulence model codes.

A variable geometry outlet plenum test cell which simulates two reactor cases, namely those of the Fast Flux Test Facility (FFTF) and the Clinch River Breeder Reactor Project (CRBRP), has been fabricated, and is shown in Fig. 1.

Measurements of velocity, turbulent kinetic energy, and Reynolds stresses $(-\rho\,\overline{u'v'})$ in the two perpendicular directions are obtained simultaneously by use of a DISA Mark-II two-channel Laser Doppler Anemometer (4) operating in the reference beam mode as shown in Fig. 2. Both velocity component signals have 40 MHz preshift devices and frequency down mixing to remove the ambiguity regarding the flow direction in low speed measurements. A 2-watt Spectra Physics Argon Laser is the light source.

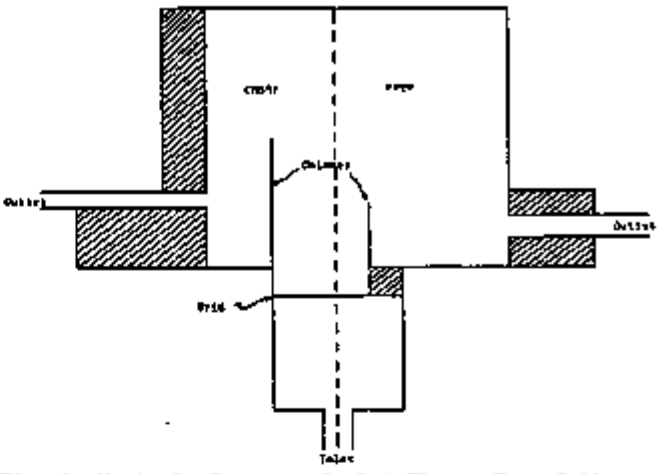

Fig. 1 Variable Geometry Outlet Plenum Test Cell

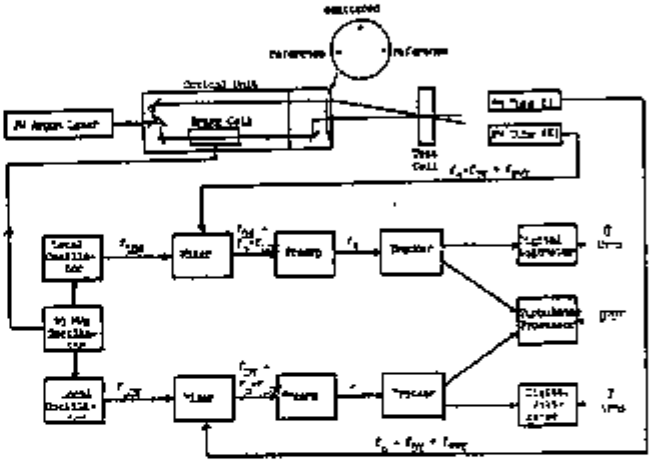

Fig. 2 Layout of Instrument and Optic Unit

RESULTS

The results obtained have shown significant discrepancies in the agreements between the measurements and the code predictions in a spectrum of cases. The experimental errors are typically 20 percent for the Reynolds stress, 5 percent for the turbulence kinetic energy, and 2 percent for the mean velocity data. In all of the TEACH-T calculations the mean velocity field and the turbulence kinetic energy field at the plenum inlet are set equal to the values measured in the case of interest. In all of the VARR-II calculations the inlet mean velocity distributions are set equal to the measured values; however, the turbulence kinetic energy and Reynolds stress values are calculated internally in the program.

The measured and predicted velocity field data for the cases investigated are shown in Figs. 3 through 12 for the 1/15 scale FFTF geometry and in Figs. 13 through 15 for the 3/80-scale CRBR geometry. In each of the Figures the data are normalized in terms of the maximum value of the inlet velocities. It is seen consistently in examining the data that both the measured and predicted flow fields depend strongly upon both the inlet flow conditions (velocity distribution and turbulence level) and the turbulent momentum exchange in the flow. The results obtained are discussed in order of ascending Figure number.

The first set of data applies to the FFTF geometry at a Reynolds number (Re) value of 70,000 (defined with respect to the inlet orifice width). It is seen that the velocity fields comparison between TEACH-T, VARR-II and the experiment is good throughout the field, except that the predicted vortex centers are displaced from the observed location and the predicted mean velocity values near the cell boundaries are significantly greater than those observed experimentally.

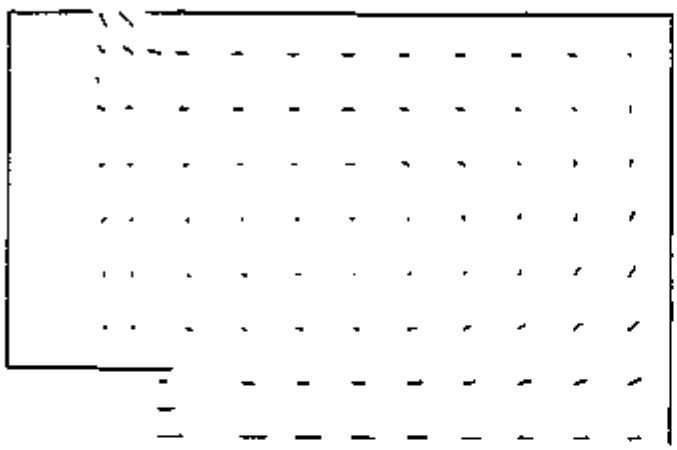

Fig. 3 Measured Mean Flow Field, FFTF Geometry, Re = 70,000

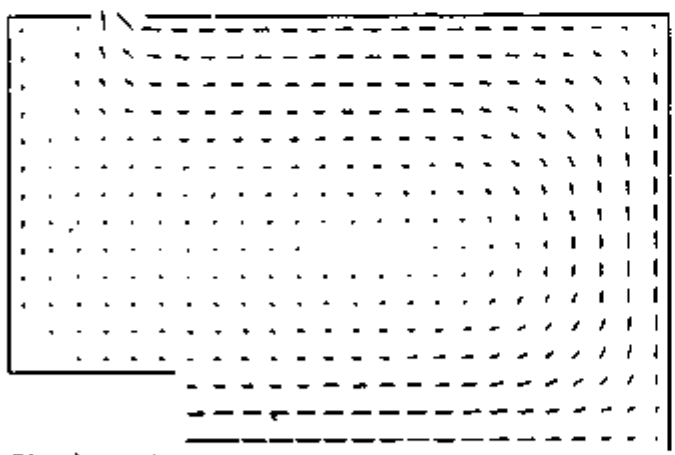

Fig. 4 TEACH-T Prediction, FFTF Geometry, Re = 70,000

It is seen in Figs. 6 and 7 that the turbulence parameter fields predicted by TEACH-T agree reasonably well at most positions with those observed experimentally (i.e. within the same order of magnitude), and those predicted by VARR-II are generally smaller than the measured values by as much as an order of magnitude, typically. It is seen that the Reynolds stress agreement is poorer for both codes than is that for the turbulence kinetic energy, since in neither calculation are the inlet Reynolds stress values matched to the experimental values. The generally better quality of the TEACH-T prediction reflects the value of specifying accurately the inlet velocity and turbulence kinetic energy distributions.

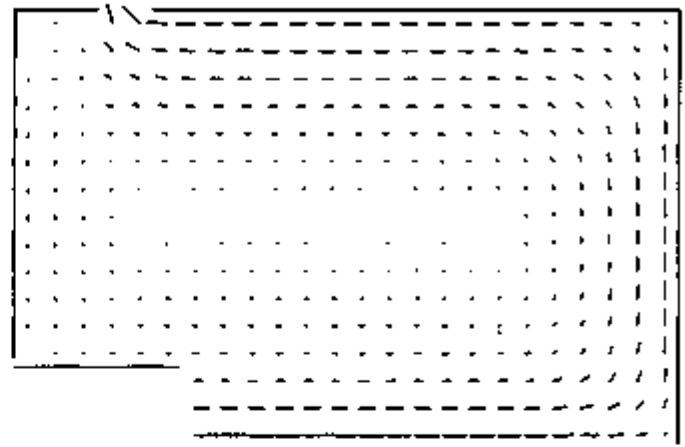

Fig. 5 VARR-II Prediction, FFTF Geometry, Re = 70,000

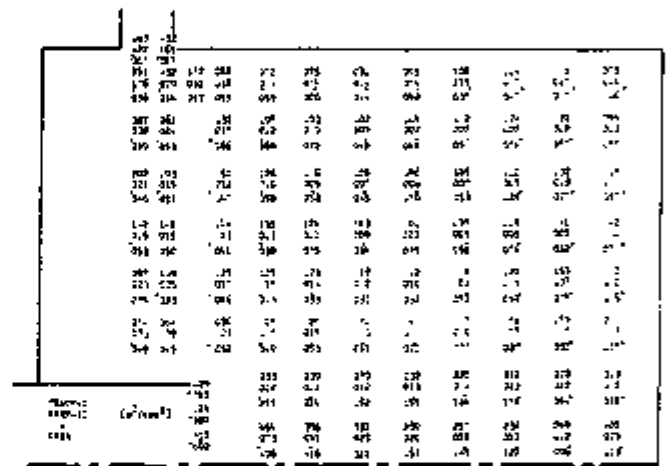

Fig. 6 Compared Calculated and Measured Turbulence Kinetic Energy Fields, FFTF Geometry, Re = 70,000

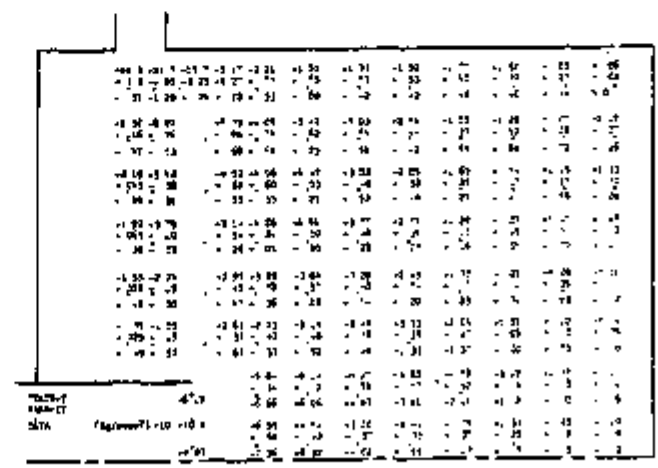

Fig. 7 Compared Calculated and Measured Reynolds Stress Fields, FFTF Geometry, Re = 70,000

It has also been observed that further improvement can be obtained by matching the inlet Reynolds stress values in the calculations to those observed experimentally.

The qualitative dependence of the observed and predicted flow fields upon the inlet mean velocity distribution is shown in a startling fashion in Figs. 8 through 12. In this case in the FFTF geometry the inlet mass flow rate is maintained for Re = 70,000; however, a partial inlet flow blockage is used to provide a velocity distribution which has a maximum near the outside edge of the inlet duct (See Fig. 8). This results in a mean flow map which is qualitatively different from that observed in the previous cases. The main flow is observed to pass through the lower portion of the plenum, with an upper region being occupied by a counter-rotating secondary flow. This is due to the high rate of mean flow shear above the inlet orifice with rapid entrainment of fluid in the plenum, accompanied by strong degradation of the inlet jet momentum. It is notable that both of the codes are able to predict the qualitative features of this flow, although neither code is successful in describing the experimentally observed flow field in detail, particularly in regard to the location and rate of circulation of the secondary flow vortex.

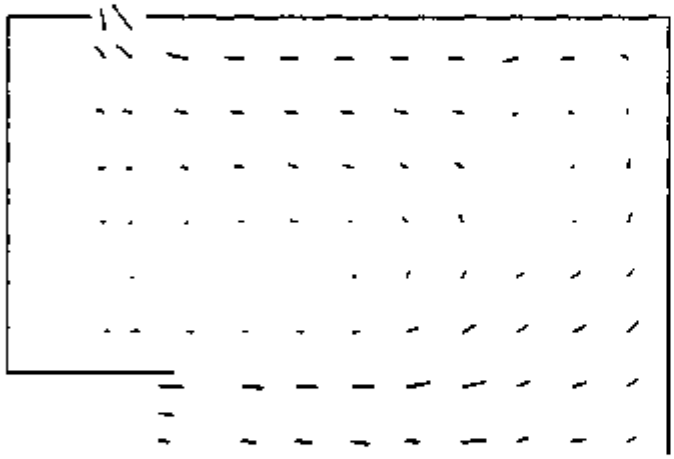

Fig. 8 Measured Mean Flow Field, FFTF Geometry, Re = 70,000, Distorted Inlet Mean Flow Distribution

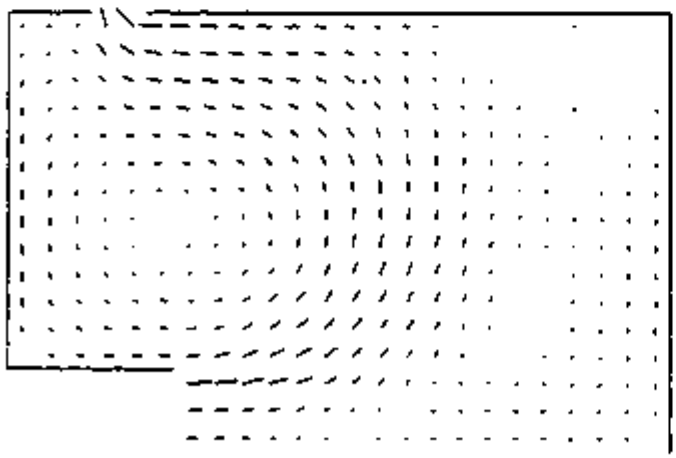

Fig. 9 TEACH-T Prediction, FFTF Geometry, Re=70,000, Distorted Inlet Mean Flow Distribution

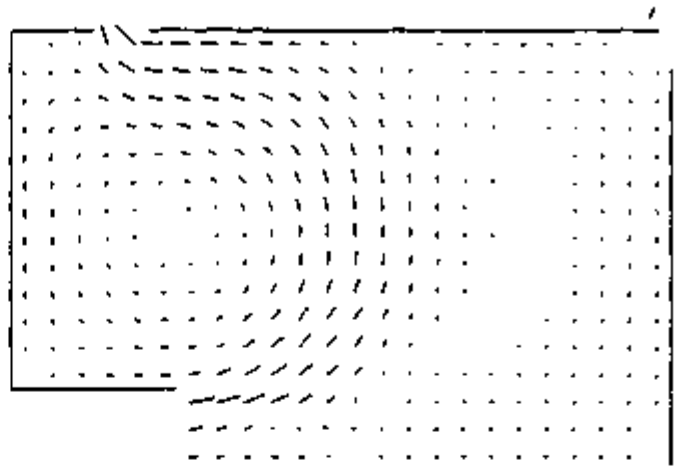

Fig. 10 VARR-II Prediction, FFTF Geometry, Re =70,000, Distorted Inlet Mean Flow Distribution

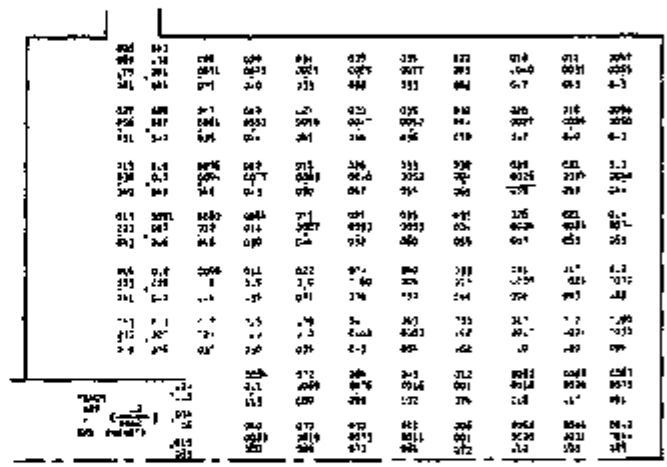

Fig. 11 Compared Calculated and Measured Turbulence Kinetic Energy Fields, FFTF Geometry, Re = 70,000, Distorted Inlet Mean Flow Distribution

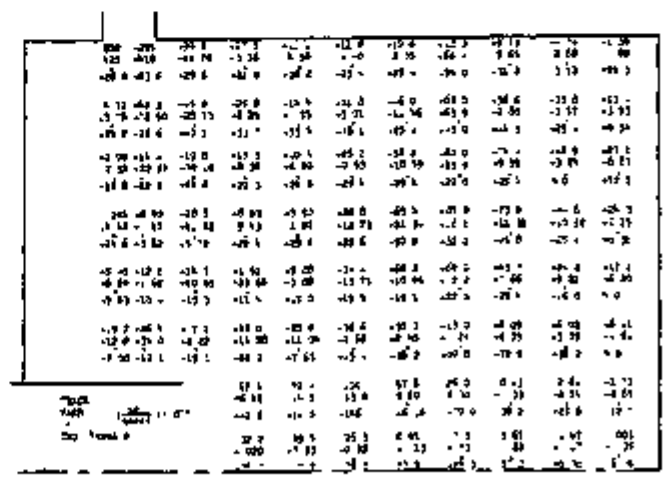

Fig. 12 Compared Calculated and Measured Reynolds Stress Fields, FFTF Geometry, Re = 70,000, Distorted Inlet Mean Flow Distribution

As with the previous cases the TEACH-T prediction of the turbulence parameters is much more successful than that of VARR-II, reflecting the more accurate inlet turbulence specification in the former case. The importance of this case lies in demonstrating that the qualitative nature of the mean flow field is strongly dependent upon the inlet mean velocity field. The implications for design calculations of the need for an accurate knowledge of these inlet conditions is clearly evident.

Data similar to those obtained in the 1/15-scale FFTF test cell have also been obtained for steady state water flows in a 3/80-scale Clinch River Breeder Reactor (CRBR) outlet plenum geometry (see Fig. 13). In this geometry the inlet orifice (i.e., the region above the reactor core) is much wider, and penetrates to a much greater height into the plenum, so that relative to the inlet orifice width the outlet plenum is much shorter and narrower than in the FFTF case. A mass flowrate approximately equal to that at a Re value of 70,000 in the FFTF geometry results in a Re value of 35,000 in the CRBR geometry.

The CRBR data with the "normal" inlet mean flow distribution are shown in Figs. 13 through 15. Effectively in this geometry the inlet jet impacts against the upper plenum boundary in a much shorter distance than in the FFTF case and then rebounds to the outlet duct due to high upper plenum stagnation pressures, while in the FFTF geometry the mean flow is able to follow streamlines from the entrance to the exit in a fashion as would be encountered in a laminar flow.

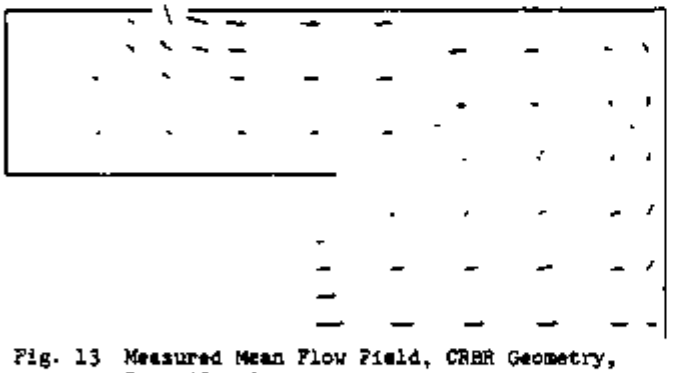

Fig. 13 Measured Mean Flow Field, CRBR Geometry, Re = 35,000

This greater mean flow chaos is seen in the comparison of the measured mean flow field (Fig. 13) to the TEACH-T (Fig. 14) and VARR-II (Fig. 15) predictions. It is seen in the lower half of the plenum that the measurements and code predictions agree reasonably well, with the TEACH-T prediction agreeing excellently and with the VARR-II prediction being approximately 20% too high in the high velocity regions. In the upper half of the plenum it is seen that neither of the codes is able to predict the flow field qualitatively. As in previous cases the VARR-II prediction (not shown here) is insensitive to the matching of the turbulence kinetic energy to the experiment at a single inlet point, and the predicted turbulence kinetic energy field is typically too low by approximately an order of magnitude

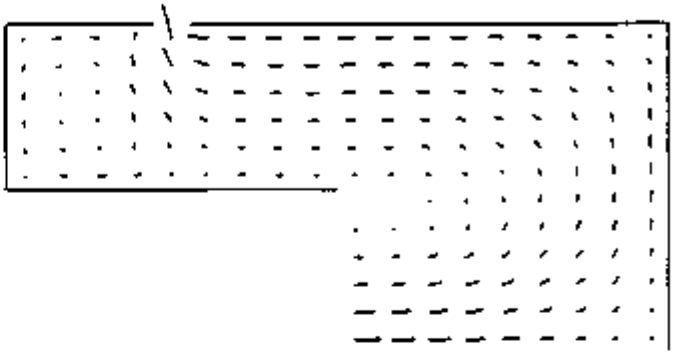

Fig. 14 TEACH-T Prediction, CRBR Geometry, Re = 35,000

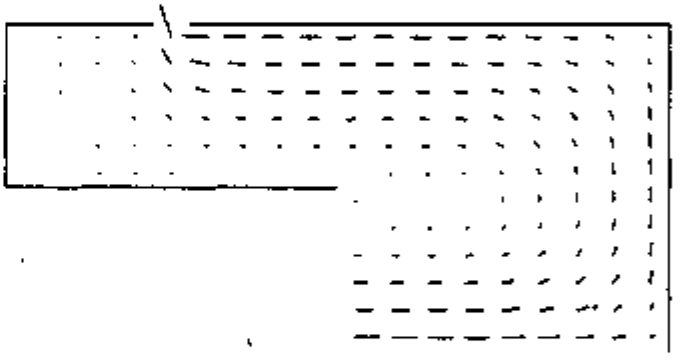

Fig. 15 VARR-II Prediction, CRBR Geometry, Re = 35,000

throughout most of the flow field.

CRBR flow data for Re = 35,000 are not shown here for the case with a partial inlet flow blockage, resulting in a distorted inlet mean flow distribution. The striking feature is that neither code is able anywhere except in the neighborhood of the inlet and outlet ducts. In a situation such as this one the highly chaotic mean flow distribution (with little net mass flow) in the upper plenum region is translated by the codes into a stagnant, or alternatively into a recirculating flow region. Thus, the net flow into and out of the plenum is predicted correctly, but the flow pattern within the plenum is described very inaccurately.

CONCLUSIONS

From examination of the turbulence data for the FFTF and CRBR geometries it is seen that the predictions for the latter geometries fail because the degree of detail required for describing the turbulence kinetic energy (k) and Reynolds stress variation (σ) is not supplied in the turbulence models examined. From the experimental data (see Figs. 6 and 7) it is seen in the FFTF case that k is approximately uniformly distributed spatially, and that σ increases from the vortex center approximately in proportion to

the mean-flow kinetic energy. Notably, the calculated turbulence fields do not display this detailed spatial behavior, although the mean flow field predictions are similar to the measured fields.

The TEACH-T model has been developed with extensive experimental testing in recirculating flows, while the VARR-II model has been verified experimentally only for boundary layer flows (5). Thus, it is not surprising that the former model provides superior results.

In a separate calculation we have observed that use of a relationship $\overline{u'v'} = C_1|u|^2$ rather than a two-equation turbulence model yields results in the FFTF geometry which are of accuracy equivalent to that obtained from the more complicated models for both normal and distorted inlet velocity distributions. The results are only weakly sensitive to the value of C_1.

The more important conclusions arise from the inability of either code to predict the qualitative flow behavior in either geometry when the distorted inlet conditions prevail. This indicates that the turbulence model used to describe turbulent momentum transfer within the flow may be less important than an accurate knowledge of the detailed inlet mean flow and turbulence fields. It is notable that the zero-equation model $\overline{u'v'} = C_1|u|^2$ $(-20 \geq C_1 \geq -50)$ provides results in this case which are of comparable accuracy to the two codes.

By contrast in the CRBR geometry it is seen that the turbulence model calculations are much less accurate than in the FFTF case in the prediction of mean flow fields. The predictions of turbulence quantity fields is hopelessly poor. The causes for this can be seen from an examination of the experimental turbulence data. It is seen that the k-field is large in the inlet jet region, with declining values as one progresses toward the outlet. The region downstream from the inlet jet is characterized by conversion of mean flow kinetic energy into stagnation pressure, and turbulence kinetic energy with these quantities exceeding viscous dissipation. In this region it would be expected that the turbulent correlation $\overline{u_j'\phi'}$ would be large and would have a complicated spatial variation, although a measurement of it is unavailable. In addition, because of the more tortuous flow path in the CRBR geometry, the number of significant length-scales determining the nature of the flow in any region of the plenum would be greater than in the FFTF use; the magnitude and complexity of each term in the enclosed turbulence equations would be increased greatly as will the degree of departure from turbulent isotropy. The net result is that the closure assumptions for the turbulence models examined are too simple to describe adequately the complicated nature of the CRBR flow field.

From the FFTF cases having normal inlet flow conditions it is seen that excellent agreement is obtained between the TEACH-T predictions and the measurements. The inferior quality of the VARR-II predictions is attributable to the inability to match the inlet turbulence conditions to those in the experiment, as well as to possible errors in the turbulence model.

The inability of either program to predict the nature of the flow under distorted inlet conditions indicates that the choice of a turbulence model is not as important as an accurate knowledge of inlet flow and turbulence field. It also implies that codes such as those used in this study should be used with great caution in which abrupt changes in shape situations arise (i.e., CRBR flows) or in which stron mean flow gradients or several length scales are imposed. Within these limitations codes of the type used in this work can provide predictions which are useful for design purposes, although further work is required to determine the degree of accuracy of turbulent momentum exchange within a simple geometry well-specified flow.

ACKNOWLEDGMENT

This work was performed with financial support from the U.S. Energy Research and Development Administration.

REFERENCES

1 Rodi, W., and Spalding, D.B., "A Two-Parameter Model of Turbulence and its Application to Free Jets," Warme-und Stoffübertra gung, Vol. 3, 1970, pp. 85-95.

2 Notes on "Turbulent Recirculating Flow-prediction and Measurement," College of Engineering, The Pennsylvania State University. July 28-August 1, 1975.

3 Cook, J.L., Nakayama, P.I., "VARR-II. A Computer Program for Calculating Time Dependent Turbulent Fluid Flows with Slight Density Variation," WARD-D-0106. July 1975.

4 The DISA Mark II Laser Doppler Anemometer, DISA Electronics, Franklin Lakes, N.J., 1974.

5 Stuhmiller, J.H., "Development and Validation of a Two-Variable Turbulence Model," SAI-74-509-LJ, January 1974.

6 Amsden, A.A., Harlow, F.H., "The SMAC Method: A Numerical Technique for Calculating Incompressible Fluid Flows," LA-4370, May 1970.

7 Caretto, L.S., Gosman, A.D., Patankar, S.V., Spalding, D.B., "Two Calculation Procedures for Steady, Three-dimensional Flows with Recirculation," Imperial College, Mechanical Engineering Department Report No. HTS/72/5.

APPENDIX

The fundamental equations of the VARR-II and TEACH-T codes are outlined in this appendix. These codes are used to provide the detailed analysis of the experiment, and the theoretically predicted velocity and turbulence distributions.

VARR-II

The equations solved by this code in cylindrical coordinates are the following:

$$\frac{\partial u}{\partial t} + \frac{1}{r}\frac{\partial}{\partial r} ru^2 + \frac{\partial}{\partial z} uw = -\frac{\partial p}{\partial r} + \frac{(\rho-\rho_o)}{\rho_o} g_x + \frac{\partial}{\partial r}\left[\left(\frac{\sigma}{r}\right)\frac{\partial}{\partial r}(ru)\right] + \frac{\partial}{\partial z}\left(\sigma\frac{\partial u}{\partial z}\right) \quad (1)$$

$$\frac{\partial w}{\partial t} + \frac{1}{r}\frac{\partial}{\partial r} ruw + \frac{\partial}{\partial z} w^2 = -\frac{\partial p}{\partial z} + \frac{(\rho-\rho_o)}{\rho_o} g_z + \frac{1}{r}\frac{\partial}{\partial r}\left(r\sigma\frac{\partial w}{\partial r}\right) + \frac{\partial}{\partial z}\left(\sigma\frac{\partial w}{\partial z}\right) \quad (2)$$

$$\frac{\partial k}{\partial t} + \frac{1}{r}\frac{\partial}{\partial r} ruk + \frac{\partial}{\partial tz} wk = 2\sigma(SIJ) + \Gamma\left[\frac{1}{r}\frac{\partial}{\partial r}\left(r\sigma\frac{\partial k}{\partial r}\right) + \frac{\partial}{\partial z}\left(\sigma\frac{\partial k}{\partial z}\right)\right] - 4\alpha k^2/\sigma \quad (3)$$

$$\frac{\partial \sigma}{\partial t} + \frac{1}{r}\frac{\partial}{\partial r}(ru\sigma) + \frac{\partial}{\partial z}(w\sigma) = \frac{\sigma^2}{k}(SIJ) + \Gamma(\sigma/k)$$
$$[\frac{1}{r}\frac{\partial}{\partial r}(r\sigma\frac{\partial k}{\partial r}) + \frac{\partial}{\partial z}(\sigma\frac{\partial k}{\partial z})] - \Gamma_1(\frac{\sigma^3}{k^2})$$
$$\{\frac{1}{r}\frac{\partial}{\partial r}[r\sigma\frac{\partial}{\partial r}(k/\sigma)] + \frac{\partial}{\partial z}[k\frac{\partial}{\partial z}(k/\sigma)]\}$$
$$- \alpha(k/\sigma)\sigma \qquad (4)$$

$$\frac{\partial I}{\partial t} + \frac{1}{r}\frac{\partial}{\partial r}(ruI) + \frac{\partial}{\partial z}(wI) = -q + \frac{1}{r}\frac{\partial}{\partial r}$$
$$(r\gamma_T\sigma\frac{\partial I}{\partial r}) + \frac{\partial}{\partial z}(\gamma_T\sigma\frac{\partial I}{\partial z}) \qquad (5)$$

$$\frac{1}{r}\frac{\partial}{\partial r}(ru) + \frac{\partial w}{\partial z} = 0 \qquad (6)$$

where $SIJ \equiv (\frac{\partial u}{\partial r})^2 + (\frac{\partial w}{\partial z})^2 + \frac{1}{2}(\frac{\partial u}{\partial z} + \frac{\partial w}{\partial r})^2 + \frac{u^2}{r^2}$

The recommended values of constants (5) are

Γ	α	Γ_1	γ_T
1.5	.045	0.75	.5

The solution scheme adopted is the Simplified Marker And Cell (SMAC) method (6). It may be summarized as follows.

1 Computing guesses for the new velocities for the entire mesh from finite difference form of equation (1) and (2) which involve only the previous time values.

2 Matching the boundary conditions and adjusting these velocities to satisfy the continuity equation (6) by making appropriate changes in the cell pressure. In the iteration, each cell is considered successively and is given a pressure changes that drives its instantaneous velocity divergence to zero.

3 When convergence has been achieved, the velocity and pressure fields can be used to compute turbulence kinetic energy, turbulence kinematic viscosity and internal energy.

4 Finally, all the field properties are at the advanced time level and may be used as starting value for the next cycle.

TEACH-T

The equations solved by this code in tensor forms are:

$$\frac{\partial}{\partial x_j}(\rho u_j u_i) - \frac{\partial}{\partial x_j}(\mu_t\frac{\partial}{\partial x_j}u_i - \rho\overline{u_i' u_j'}) - \frac{\partial p}{\partial x_i} = 0 \qquad (7)$$

$$u_j\frac{\partial}{\partial x_j}\rho k - \frac{\partial}{\partial x_j}(\frac{\mu_t}{\sigma_k}\frac{\partial k}{\partial x_j}) - \mu_t G + \rho\epsilon = 0 \qquad (8)$$

$$u_j\frac{\partial}{\partial x_j}\rho\epsilon - \frac{\partial}{\partial x_j}(\frac{\mu_t}{\sigma_\epsilon}\frac{\partial \epsilon}{\partial x_j}) - \frac{C_1\epsilon}{k}\mu_t G + C_2\rho\frac{\epsilon^2}{k} = 0 \qquad (9)$$

$$\frac{\partial}{\partial x_j}(\rho u_j) = 0 \qquad (10)$$

where

$$-\rho\overline{u_i' u_j'} = \mu_t(\frac{\partial u_i}{\partial x_j} + \frac{\partial u_j}{\partial x_i})$$

$$\mu_t = C_\mu\rho k^2/\epsilon$$

$$G \equiv (\frac{\partial u_i}{\partial x_j} + \frac{\partial u_j}{\partial x_i})\frac{\partial u_i}{\partial x_j}$$

The recommended values of constants (2) are

C_μ	C_1	C_2	σ_k	σ_ϵ
.09	1.44	1.92	1.0	1.3

The solution scheme (7) may be summarized as follows. Integrating the partial differential equations over the control volume, using the Gauss's theorem to replace volume integral by surface ones, then approximating the integrals with the aid of one-dimensional analysis. A hybrid of central and upwind difference is used to treat convection and diffusion term, and in order to obtain good stability and accuracy. The solution technique is a cyclic series of guess and correct operations. Firstly, the guessed velocities and pressure are substituted into momentum equations, it will yield intermediate velocities. However, these will not satisfy the continuity equation. The pressures are then adjusted so as to satisfy continuity. In general, it is not necessary to satisfy continuity for each cycle, since the later calculation of k and ϵ will affect the velocities. In TEACH-T code u, v, k and ϵ are solved three times and pressure five times for each cycle. The convergence criterion is set for residual soure for mass and velocities to be below selected values. This solution algorithm obviates the need to approach the steady state via time evolution of the flow, as is required by conventional method (e.g., SMAC method in VARR-II). In the plenum case, the computation time for TEACH is approximately one order of magnitude less than that of VARR-II.

TASK IV: THEORETICAL DETERMINATION OF LOCAL TEMPERATURE FIELDS IN LMFBR FUEL ROD BUNDLES

TASK IVA: Code Development for Solving the 2-D Multicell Multiregion Energy Equations

(Man Kit Yeung)

SUMMARY:

During the last quarter, emphasis has been primarily focused on the determination of the geometric correction factors for the effective conduction mixing lengths of intersubchannel conduction heat transport. Detailed analytical procedures for calculating the geometric correction factor from a local temperature field of a hexagonal bundle are illustrated. Efforts have been also directed to investigate the effect of power tilting on the behavior of the geometric correction factor. Calculations with accurately predicted correction factor for a 7-pin LMFBR bundle are performed with COBRA-IIIC for different flow conditions. The calculational results indicate that significant design margins can be gained by implementing the accurately predicted mixing lengths in subchannel calculations.

INTRODUCTION

Subchannel codes usually divide the assembly into a finite grid of "subchannels" each of which is characterized by a bulk temperature, flow rate and pressure.

Energy transport between adjacent subchannels is governed by the mechanisms of diversion cross-flow, turbulence mixing and conduction. (Naturally, the layout of the subchannels may not be the same as the unit cells used in the present analysis.) For LMFBR design calculations the energy transport by conduction constitutes a major contribution to the overall energy transport. This effect is even more promounced for flows which are characterized by low-Re numbers. These flow situations especially arise in the case of a loss-of-flow accident and the like. Despite this importance only scattered information is available for internal subchannels [1], but nothing is known for the subchannels near the bundle wall regions. In this chapter, effective lumped parameters due to conduction are determined by using the coolant temperature field resulted from the multicell analysis.

2. Definition of Effective Conduction Mixing Length

The heat transfer rate due to conduction between adjacent subchannels i and j as calculated in subchannel codes is given by: [2]

$$Q_{ij} = k_c \frac{S_{ij}(\bar{T}_i - \bar{T}_j)}{l_{ij}} = k_c \frac{S_{ij}}{l^*_{ij}} (\bar{T}_i - \bar{T}_j) \frac{1}{L_{ij}} \qquad (1)$$

Where S_{ij} = the length of the common boundary

l_{ij} - the effective conduction mixing length

l^*_{ij} - the centroid-to-centroid distance of adjacent coolant channels

and L_{ij} - a dimensionless correction factor representing the ratio of the effective conduction mixing length to the centroid- to-centroid distance, i.e.,

$$L_{ij} = \frac{l_{ij}}{l^*_{ij}} \qquad (2)$$

In subchannel calculations, L_{ij} is usually set to be unity due to the lack of knowledge of the local temperature field. It is quite obvious that the lumped parameter codes will not quite give reliable results if the correct effective mixing lengths are not known. However, by setting the L_{ij} to be unity implies that the effective conduction mixing length is equal to the centroid-to-centroid distance. This assumption is completely intuitive and lacks either analytical or experimental verification. With some rearrangements, Eq. (1) can be written as:

$$L_{ij} = k_c \frac{S_{ij}}{l^*_{ij}} \frac{\bar{T}_i - \bar{T}_j}{Q_{ij}} \qquad (3)$$

In addition, the total heat transfer from subchannel i

to j due to conduction can be expressed as:

$$Q_{ij} = \int_{S_{ij}} q''_s ds \tag{4}$$

Where q''_s denotes the heat flux distribution along the common boundary between subchannels i and j. Substituting Eq. (4) into Eq. (3) leads to:

$$L_{ij} = k_c \frac{S_{ij}}{l^*_{ij}} \frac{(\bar{T}_i - \bar{T}_j)}{\int_{S_{ij}} q''_s ds} \tag{5}$$

Eq. (5) can be normalized into dimensionless form by multiplying and dividing by the group $\bar{q}'''a^2/2k_c$

$$L_{ij} = k_c \frac{S_{ij}}{l^*_{ij}} \frac{\dfrac{(\bar{T}_i - \bar{T}_j)}{\bar{q}''' a^2/2k_c}}{\int_{S_{ij}} \dfrac{q''_s}{\bar{q}''' a^2/2k_c} dS} = \frac{S_{ij}}{l^*_{ij}} \frac{\dfrac{(T_i - T_j)}{\bar{q}''' a^2/2k_c}}{\int_{S_{ij}} \dfrac{q''_s}{\bar{q}''' a^2/2}} \tag{6}$$

Multiplying and dividing the integral in the numerator by the radius of the rod leads to the formula

$$L_{ij} = \frac{S_{ij}}{l^*_{ij}} \frac{\dfrac{(\bar{T}_i - \bar{T}_j)}{\bar{q}''' a^2/2k_c}}{\int_{S_{ij}} \dfrac{q''_s}{\bar{q}''' a^2/2b} d\left(\frac{s}{b}\right)} \tag{7}$$

3. Calculation of Lumped Quantities from the Local Temperature Field of a 7-Rod Bundle.

A cross-sectional view of a typical 7-rod bundle as shown in Figure 1 is used as an example to illustrate the applicability of the local temperature field for effective conduction mixing length calculation. The dash lines indicated in the figure denote the layout of the subchannels usually employed in most subchannel calculations. Obviously this kind of coolant-centered subchannel structure does not coincide with the unit cell structure which has been used so far in this analysis. As shown in Figure 2, the symmetry section of the bundle consists of a 30^{o} internal cell and a corner cell with their common cell boundary indicated as solid line. The local temperature fields of the coolant, the clad and the fuel regions are obtained by coupling the temperature fields of the two cells.

From Figure 2, it can be seen that the internal subchannel (denoted as subchannel i) consists of the entire internal unit cell and part of the corner cell where $2\pi/3 \leq \phi\pi$ and the corner subchannel (denoted as subchannel (j) is actually the portion of the corner unit cell where $0 \leq \phi \leq 2\pi/3$. Upon multiplying and dividing the heat transfer integral of Eq. (17) by the cell-to-average power factor q_2^+ the correction factor L_{ij} can be written as:

$$L_{ij} = \frac{S_{ij}}{l_{ij}^{*}} \frac{\dfrac{(\bar{T}_1 - \bar{T}_j)}{q'''a^2/2k_c}}{q_2^+ \displaystyle\int_{S_{ij}} \frac{q_s''}{q'''a^2/2b} d\left(\frac{s}{b}\right)} \qquad (8)$$

Recognizing that the subchannel boundary is the normal of the corner cell to its second boundary for this particular example,

$$ds = dr \tag{9}$$

Furthermore the heat flux distribution at the subchannel boundary S_{ij} is given by the local temperature field of the corner cell as:

$$q_s'' = -k_c \nabla T_2 \cdot \hat{n} = -k_c \nabla T_2 \cdot (-\hat{\phi}_2) \tag{10}$$

or equivalently

$$q_s'' = k_c\left[\frac{\partial T_2}{\partial r_2}\ \hat{r}_2 + \frac{1}{r_2}\ \frac{\partial T_2}{\partial \phi_2}\ \hat{\phi}_2\right] \cdot \hat{\phi}_2 = k_c \frac{1}{r_2}\frac{\partial T_2}{\partial \phi_2} \tag{11}$$

dividing Eq. (11) by the group $q_a'''a/2b$ leads to:

$$\frac{q_s''}{q_2'''a^2/2b} = \frac{k_2 \frac{1}{r_2}\ \frac{\partial T_2}{\partial \phi_2}}{q_2''' a^2/2b} = \frac{\frac{b}{r_2}\ \frac{\partial T_2}{\partial \phi_2}}{q_2'''a^2/2k_c} = \frac{1}{\rho_2}\ \frac{\partial \theta_2}{\partial \phi_2} \tag{12}$$

Where θ_2 is the dimensionless temperature of the coolant of the corner cell as calculated from the coupled multicell calculation. Substituting Eq. (12)into Eq.(8) and integrating

from $\rho = 1$ to $a_{2,2}/b$, L_{ij} takes on the form:

$$L_{ij} = \frac{S_{ij}}{l^*_{ij}} \frac{(\bar{T}_i - \bar{T}_j)}{\bar{q}'''a^2/2k_c} \Big/ q_2^+ \int_1^{a_{2,2}/b} \frac{1}{\rho_2} \frac{\partial\theta_2}{\partial\phi_2} d\rho_2 \qquad (13)$$

Where the heat transfer integral is evaluated by the Gauss-Legendre ten-point method [3].

The next lumped quantity to be calculated from the local temperature field is the normalized averaged coolant temperature difference between subchannels. From Figure 2 it can be seen that the averaged coolant temperature of the subchannel i can be written as:

$$\bar{T}_i = \frac{A_I \langle T_1 \rangle_I + A_{II} \langle T_2 \rangle_{II}}{(A_I + A_{II})} \qquad (14)$$

Where $\langle T_1 \rangle_I$ is the averaged coolant temperature of the small internal cell integrated over the area A_I, and $\langle T_2 \rangle_{II}$ is the averaged coolant temperature of the corner cell integrated over the area A_{II} as indicated in the figure. Recalling the relation between the coolant temperature and its dimensionless temperature as given in the previous report Eq. (14) can be written as follows:

$$\bar{T}_i = \frac{A_I[A_{o,1} + \frac{q_1'''a^2}{2k_c} \langle \theta_1 \rangle_I] + A_{II}[A_{o,2} + \frac{q_2'''a^2}{2k_c} \langle \theta_2 \rangle_{II}]}{(A_I + A_{II})} \qquad (15)$$

Similarly, the averaged coolant temperature of subchannel j is given by:

(16)

$$\bar{T}_j = \frac{A_{III}\left[A_{o,2} + \frac{q'''_2 a^2}{k_c} \langle \theta_2 \rangle_{III}\right]}{A_{III}} = A_{o,2} + \frac{q'''_2 a^2}{2k_c} \langle \theta_2 \rangle_{III}$$

Naturally, the quantity $\langle \theta_2 \rangle_{III}$ denotes the averaged coolant temperature of the corner unit cell integrated over the area A_{III}.

Therefore the temperature difference between the two subchannels is obtained by combining Eqs. (15) and (16):

$$(\bar{T}_i - \bar{T}_j) = \frac{(A_I A_{o,1} + A_{II} A_{o,2})}{A_1 + A_{II}} - A_{o,2} + \frac{A_I \frac{q'''_1 a^2}{2k_c} \langle \theta_1 \rangle_I + \frac{A_{II} q'''_2 a^2}{2k_c} \langle \theta_2 \rangle_{II}}{A_I + A_{II}}$$

$$+ \frac{q'''_2 a^2}{2k_c} \langle \theta_2 \rangle_{III} \qquad (17)$$

Simplifying Eq. (17) and dividing Eq. (17) by the group $q''' a^2/2k_c$ the normalized dimensionless averaged coolant temperature difference between subchannel i and j becomes:

$$\frac{(\bar{T}_i - \bar{T}_j)}{q''' a^2/2k_c} = \frac{(A_{0,1} - A_{0,2})}{q''' a^2/2k_c} \quad \frac{1}{1 + \frac{A_{II}}{A_I}} + \frac{q_1^+ \langle \theta_1 \rangle_I + q_2^+ \langle \theta_2 \rangle_{II} \cdot \frac{A_{II}}{A_I}}{1 + \frac{A_{II}}{A_I}}$$

$$+ q_2^+ \langle \theta_2 \rangle_{III} \qquad (18)$$

It can be shown that the difference between the two constants is given by:

$$Y_o = \frac{1}{2} \frac{(A_{o,2} - A_{o,1})}{q''' a^2/2k_c} \tag{19}$$

Where Y_o is a constant resulted from the coupled multicell calculation. And it can be seen from Figure 2 that the coolant area A_{II} is just twice of that of A_I. Therefore Eq. (18) finally becomes:

$$\frac{(\bar{T}_i - \bar{T}_j)}{q''' a^2/2k_c} = -\frac{2}{3} Y_o + \frac{q_2^+ \langle \theta_1 \rangle_I + q_2^+ \langle \theta_2 \rangle_{II}}{3}$$

$$+ q_2^+ \langle \theta \rangle_{III} \tag{19}$$

Additionally, it can be shown that the ratio S_{ij}/l_{ij}^* in Eq. (19) can be expressed as:

(20)

$$\frac{S_{ij}}{l_{ij}^*} = \frac{\frac{1}{2}\left(\frac{P}{D} - 1\right)}{\left[\frac{\frac{1}{16}\left(\frac{2w}{D}\right)^2\left(\frac{P}{D}\right) + \frac{1}{24\sqrt{3}}\left(\frac{2w}{D}\right)^3 - \frac{1}{16}}{\frac{1}{4}\left(\frac{P}{D}\right)\left(\frac{2w}{b}\right) + \frac{1}{2\sqrt{3}}\left(\frac{2w}{D}\right)^3 - \frac{\pi}{12}} + \frac{\frac{1}{2}\left(\frac{P}{D}\right)^3 - \frac{\sqrt{3}}{12}\pi\left(\frac{P}{D}\right)}{\sqrt{3}\left(\frac{P}{D}\right)^2 - \frac{\pi}{2}}\right]}$$

Thus all quantities in Eq. (13) can be determined either by appropriately lumping the coolant temperature fields resulted from the local analysis or just by geometric parameters. Numerical calculation results are given in the next section.

CORRECTION FACTOR FOR EFFECTIVE CONDUCTION MIXING LENGTH

In this section the correction factor for the effective conduction mixing length for a 7-rod bundle with pitch-to-diameter ratios of 1.24 and 1.08 are determined as examples for typical fuel and blanket assemblies respectively. Before the L_{ij} for each case is given, it is advantageous to investigate the behavior of the limped quantities namely the normalized averaged intersubchannel coolant temperature difference and the integral net heat transport between subchannels. These two quantities for a 7-rod fuel bundle ($\frac{P}{D} = 1.24$) are given as a function of the dimensionless wall distance ($\frac{2w}{D}$) in Figures 3 and 4 for multi-region and single region analyses, respectively. For these calculations, slug flow without flow split is assumed. From Figures 3 and 4, it becomes obvious that both the normalized temperature difference and the integral heat transport between subchannels increase monotonically with the dimensionless wall distance $\frac{2w}{D}$. Physically, this is because the degree of undercooling of the fraction of the coolant in the vicinity of the bundle wall increases as a result of the increase in $\frac{2w}{D}$ ratio which implies a widening of the coolant channel. In addition, the increase in the dimensionless wall distance ($\frac{2w}{D}$) results in larger coolant area in the near bundle wall region which provides a larger heat sink and as a result attracts more heat to be conducted into this region.

In can also be seen from Figure 4 that for both single and multi-region analyses the normalized averaged coolant tempera-

ture differences between subchannels for the fuel assembly have values of 0 at approximately $\frac{2w}{D} \simeq 1.16$. For smaller $\frac{2w}{D}$ values the normalized averaged coolant temperature between subchannels becomes negative implying that the averaged coolant temperature of subchannel j is higher than that of subchannel i. In addition, the normalized integral heat transport intersects the abscissa at approximately 1.13 for both the single and multi-region analyses implying a zero net heat transport between subchannels. For smaller values of $\frac{2w}{D}$ the integral heat transport becomes negative indicating a reversal of the heat flow direction, i.e., heat is transported from subchannel j to i.

Having determined the lumped quantities from the local temperature field resulted from the multicell coupling calculation, it is of prime interest to investigate the behavior of the correction factor L_{ij} as given by Eq. (13). Figure 5 shows L_{ij} as a function of the dimensionless wall distance for the 7-rod bundle in case of $\frac{P}{D} = 1.24$. It is evident that both the multi and single region analyses indicate that L_{ij} generally deviates quite substantially from unity what is usually assumed in subchannel codes such as COBRA-IIIC [4]. The singularities shown in the figure implies zero integral net heat transport between subchannels. To the right of the singularities of both curves there is a range in which L_{ij} assumes negative values. This is due to the fact that in this small range of $\frac{2w}{D}$ the net integral heat transport does

not have the same sign as the normalized averaged coolant temperature difference between subchannels, i.e., the averaged coolant temperature of subchannel j is higher than that of subchannel i but the net integral heat transport by conduction is from subchannel i to subchannel j. This is a surprising result but does not constitute a violation of basic heat transfer laws. This is because the heat trasnfer at the subchannel boundary S_{ij} is a rather short-ranged phenomenon and is not governed by the subchannel averaged coolant temperatures resulted from a more-or-less arbitrary lumping scheme.

For larger values of $\frac{2W}{D}$ ($\frac{2W}{D} \geq 1.3$ or so) the L_{ij} s approach their respective asymptotic values of 0.81 and 0.71 approximately for multi and single region analysis, respectively. In this range of $\frac{2W}{D}$ ratio the L_{ij} is independent of the wall distance and is only governed by the $\frac{P}{D}$ ratio. Therefore for $\frac{2W}{D} \geq 1.30$ (which is typical for current LMTER designs). The net heat transport between subchannels in subchannel code calculation can be easily corrected by a constant correction factor resulted from the local temperature field.

To the left of the singularity, asymptotic values of L_{ij} are not achieved in the range of $\frac{2W}{D}$ being considered. However, it can be seen readily that values of L_{ij} for both curves are generally larger than one. The sudden change of L_{ij} clearly indicates a geometric effect on heat transport characteristic between subchannels, i.e., the net heat transport from subchannel i to j will not be the same as the net heat transport from sub-

channel j to i if the averaged coolant temperature of subchannel i to j is simply interchanged, i.e., a different L_{ij} has to be used if the heat flow direction is reversed. Up to this point all calculations are based on the assumption of equal powers in the rods. However, this is not the case especially for the blanket assembly where large power gradients may exist. In order to investigate the effect of interassembly power gradient three cases with different power peaking factors in the rods are performed as indicated in Table 1. Moreover only multiregional analysis is performed for these calculations because it is physically unrealistic to impose a uniform heat flux distribution at the clad outer surface in such a closely packed bundle. The normalized intersubchannel temperature difference and integral heat transport between subchannel i and j are plotted vs. $\frac{2w}{D}$ in Figures 6 and 7 respectively. As expected, case 1 results in the highest intersubchannel temperature difference and heat transport because of the unfavorable combination of its geometry and the power distribution.

For case 3, the opposite is true. Furthermore, the normalized intersubchannel heat transport has a zero value at around $\frac{2w}{D} = 1.06$ implying that a reversal of heat flow direction occurs. The geometric correction factors (L_{ij}) for these three cases are given in Figure 8 as a function of $\frac{W}{D}$ ratio. It can be seen from the figure that all three curves emerge to the same asymptotic L_{ij} value (~ 0.64) despite large difference in power distribution. The power distribution in the rods simply shifts the loca-

tion of the curves but does not alter the shapes of the curves. However, for the practical design of blanket assemblies the dimensionless wall distance is in the vicinity of 1.10 or so, therefore significant variation in L_{ij} is not experienced.

The effect of L_{ij} on subchannel calculations will be investigated and presented in the next section.

5.4. EFFECT OF L_{ij} ON SUBCHANNEL CALCULATIONS

In order to demonstrate the effect of L_{ij} on subchannel calculations two cases with different flow conditions were performed with CØBRA-IIIC for the 7-Rod Fuel Assembly. For each case channel averaged temperature at 36" from the core entrance with and without proper correction factor L_{ij} are calculated. In CØBRA-IIIC a uniform heat flux distribution is always assumed at the outside clad surface, therefore using a correction resulting from a multiregion analysis would not be consistent. As indicated by Figure 5, the analytically predicted correction factor resulted from the single-region analysis is approximately 0.7. For the cases without proper correction factor the centroid-to-centroid distance is used as the effective conduction mixing length, i.e., $L_{ij} = 1.0$. For these calculations, slug flow without flow split between subchannels has been assumed and other operating conditions are listed in Table 2. The results are summarized in Table 3.

From the results of these calculations, it is obvious that for both cases the use of an accurately predicted correction factor L_{ij} is successful in reducing the intersubchannel temperature difference as a result of increasing heat transport between subchannels. As shown in Table 3 the intersubchannel temperature difference ($\bar{T}_i - \bar{T}_j$) decreases from 70°F to 63.7° for the normal flow condition ($G=3x10^6$ lbm/ ft^2hr) and from 94.29° to 83.54°F for the low flow condition ($G=2x10^6$ lbm/ft^2hr.). Therefore the accurately predicted L_{ij} has indeed removed excess conservatism due to the lack of knowledge of the local temperature field. However, it must be pointed out that calculations with analytically predicted value of L_{ij} do not necessarily result in conservative results. For example, using a $L_{ij} > 1$ in subchannel calculations (which is the case for a fuel assembly with small $\frac{2w}{D}$ ratio) will result in a decrease in intersubchannel heat transport for the same intersubchannel temperature gradient and lead to higher subchannel temperature difference than predicted by calculation without the correction factor.

Another important feature of the calculational results which has to be pointed out is that the effect of the correction factor is more pronounced when the mass flow rate decreases, i.e., a reduction in intersubchannel temperature difference of 6.3°F for the normal flow condition vs. 10.75°F for the low flow situation. Therefore it can be easily imagined that untolerable error in heat transport and subsequent channel temperature would result in a loss of flow accident if the appropriate correction factor is not known.

It should be mentioned at this point that most ongoing

efforts have been devoted to the diversion mixing area which obtains mixing effects of similar magnitude and it is felt that an equally significant gain in design margin is possible by properly accounting for the conduction effect.

REFERENCES

1. D.M. France and T. Ginsberg, "Evaluation of Jumped Parameter Heat Transfer Techniques for Nuclear Reactor Applications," Nucl. Sci. and Engr. 51:41-51 (1973).

2. D.S. Rowe, "COBRA-IIIC - A Digital Computer Program for Steady State and Transient Thermal-Hydraulic Analysis of Rod Bundle Nuclear Fuel Elements.", BNWL-1695, Mar. 1973.

3. B. Carnahan, H.A. Luther, and J.O. Wilkes, "Applied Numerical Methods," John Wiley & Sons, Inc., 1969

TASK IVB: 3-D Coupled Cell Heat Transfer Analysis

(Chung Nin Wong)

1. INTRODUCTION

An axially variable "effective mixing length" for conduction heat transfer, a parameter which enters the subchannel formulation and application for LMFBR's, has been studied thoroughly in the last quarter of the year. Improvements have been made and reasonable results were obtained. A first set of results including the application of the axially variable mixing length to the 7-pin LMFBR bundle calculation performed by COBRA-IIIC will be presented in what follows. For evaluating the bulk temperature difference between two adjacent channels, the results show that using an accurate mixing length can be very important for design purposes.

2. DETERMINATION OF THE EFFECTIVE CONDUCTION MIXING LENGTH IN HEXAGONAL ROD BUNDLES

Subchannel codes like COBRA-IIIC usually "lump" the assembly into a finite grid of subchannels, each of which is characterized by a bulk temperature, flow rate and pressure. Energy transport between adjacent channels is governed by the mechanisms of diversion cross-flow, turbulent mixing and conduction mixing. For LMFBR design calculations, the energy transport

by conduction constitutes a major contribution to the overall energy transport. This effect is even more pronounced for flows which are characterized by low Reynolds numbers. These flow situations especially arise in the case of a loss-of- flow accident. Due to this importance, which has been already mentioned in the previous report, it is desireable to have better knowledge of the conductive heat transport between two adjacent channels. In what follows, an attempt is made to establish a relationship for an axially variable mixing length such that it can be inputted into subchannel codes like COBRA-IIIC for achieving better results.

As noted in the previous report, L_{ij} is a dimensionless correction factor which represents the ratio of the effective conduction mixing length to the centroid-to-centroid distance ($L_{ij} = l_{ij}/l^*_{ij}$). Furthermore, L_{ij} can also be expressed in the following way:

$$L_{ij} = k \frac{S_{ij}}{l^*_{ij}} \frac{(\bar{T}_i - \bar{T}_j)}{\int_{S_{ij}} q''ds}$$

To obtain this correction factor, the bulk temperature in different channels and the average heat flux across the boundary of these two channels are needed.

The case under consideration consists of a coupled internal and corner channel with P/D = 1.3, 2w/D = 1.38, Pin diameter =

0.9 cm., heat flux = 104 cm., core height = 150 cm.

The results are plotted in figures 9, 10, 11. Fig. 9 shows the correction factor L_{ij} as a function of the axial location. It indicates that L_{ij} starts off at zero initially, increases axially and assumes an asymptotic limit. The behavior of this curve may be thought of as being the image of the entrance heat transfer coefficient. Although the numerical value is naturally completely different, there is some similarity between both parameters. The heat transfer coefficient represents the ratio of the amount of energy deposited into the coolant to the film temperature difference. Then, at the inlet, with no film temperature difference being developed yet, but heat diffusion having started already, the heat transfer coefficient is singular in this region and decreases towards an asymptotic limit. On the other hand, the correction factor includes a factor which is the ratio of the temperature difference between two zones and the heat flux across the boundary separating these two zones. It is difficult to predict how this ratio behaves at the inlet because no temperature difference and heat flux have been developed yet. But at a certain distance away from the inlet, as shown in Fig. 10 and Fig. 11, the heat flux has out-grown the temperature differences. Therefore, L_{ij} approaches zero at the entrance. Physically, this can be explained as follows: once the temperature difference exists, it initiates an instantaneous heat transport progressing through

the gap in order to decrease the difference. However, since the gap spacing is comparably small, an increased heat flux is necessary. As a result, when moving towards the entrance, the heat flux is diminishing slower than the bulk temperature difference. Thus, L_{ij} becomes zero at the inlet and increases asymptotically towards a limit value.

Figure 11, illustrates the importance of using the accurate mixing length in the calculation. The solid line represents the calculation of the bulk temperature difference between two adjacent channels obtained from the three-dimensional temperature fields, whereas, all broken lines represent cases of using different mixing lengths in COBRA-IIIC. The isolated channel approach yields the highest temperature difference at the core exit, indicating that it is over-conservative because it neglects the conduction transport at all, although this is especially high in this region. On the other hand, setting L_{ij} equal to unity which is mostly done in subchannel calculations, results in underpredicting the temperature difference because the conductive mixing obviously is not that high throughout the whole core. Finally the following empirical equation for L_{ij} as a function of the axial coordinate is applied in COBRA-IIIC

$$L_{ij} = (0.70102)\left[\frac{1}{0.0643462^{0.788} + 1}\right]$$

z in cm.

This equation has been fitted to the results obtained from the three dimensional calculations. The result shows naturally a closer agreement with the solid line. Therefore, one can conclude that it is important to have an accurately determined L_{ij} in order to get more accurate solutions.

For the specific geometry under consideration, the results indicate that setting L_{ij} equal to infinity, i.e., $L_{ij} = \infty$ results in a better agreement overall with the distributed parameter results than taking $L_{ij} = 1$. This is indeed a surprising and unexpected result. However, this picture might change drastically when the geometry of the bundle is changed. Thus, future efforts will concentrate upon expressing L_{ij} in terms of the governing geometrical parameters as well as the ratio of heat source densities in the fuel pins.

TASK IV-C. FULLY DEVELOPED LAMINAR MIXED CONVECTION

(Jong-Yul Kim)

SUMMARY

This study which has been totally completed will be published as a topical report in the Fall and specific results will be summarized in a technical paper to be submitted to the Journal of Nuclear Engineering Design. Attached is a copy of a short paper which has been submitted for presentation at the ANS winter meeting 1977 in San Francisco.

TASK IV-D. 2-D THERMOELASTIC AND INELASTIC CLAD ANALYSIS

(R. Karimi)

SUMMARY

Basically, work has been completed for this task. The objective of this subproject to develop a computational tool for a combined two-dimensional ~~normal~~ thermal and inelastic structural clad analysis has been met.

Some details are given in the attached paper which has been accepted for presentation at the 4th International Conference on Structural Mechanics in Reactor Technology to be held in San Francisco, August 15-19, 1977. Additional results which were obtained in the meantime will be given in the presentation of this paper as well as in the forthcoming progress report. A topical report will be issued in the near future.

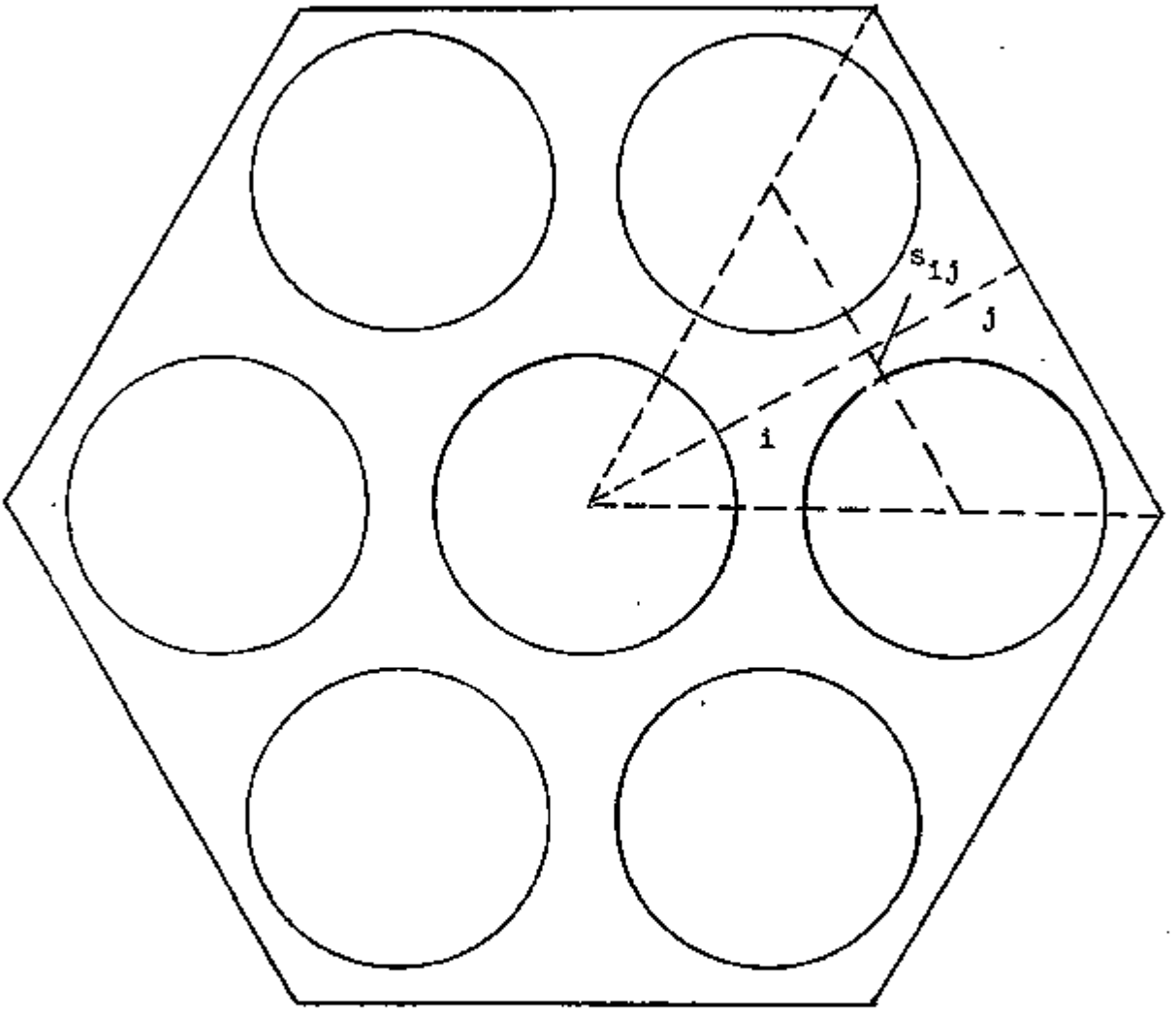

Fig. 1 Configuration of a 7 Pin Bundle

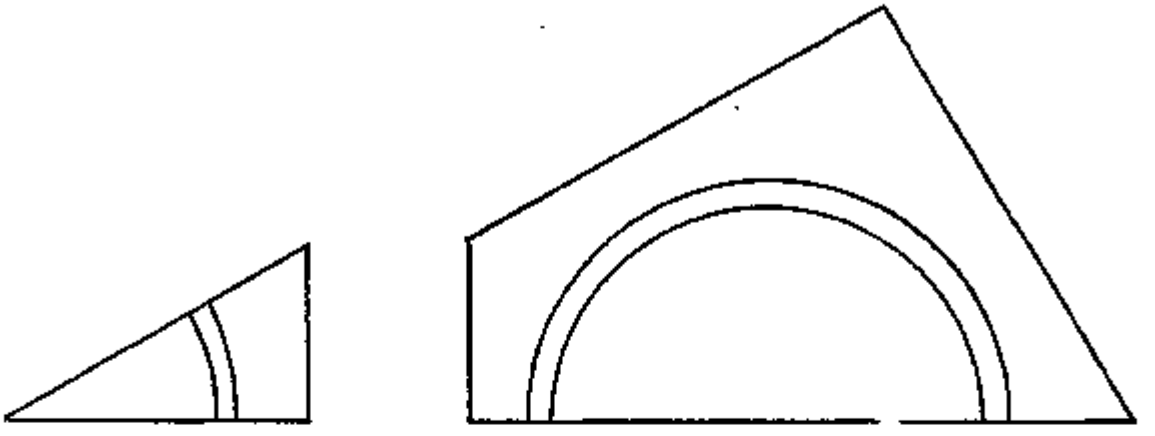

internal cell corner cell

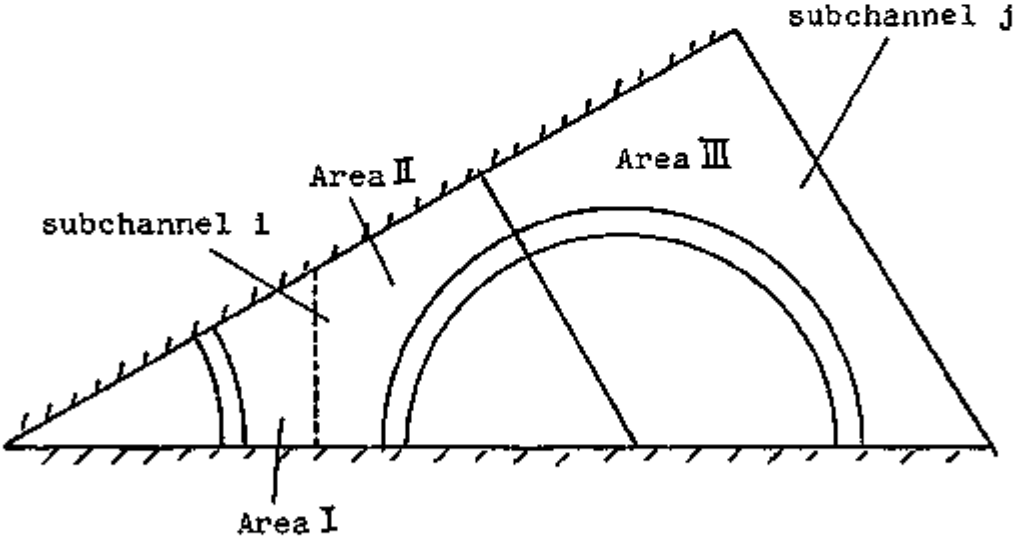

Fig. 2 Symmetry Section of a 7-Pin Bundle

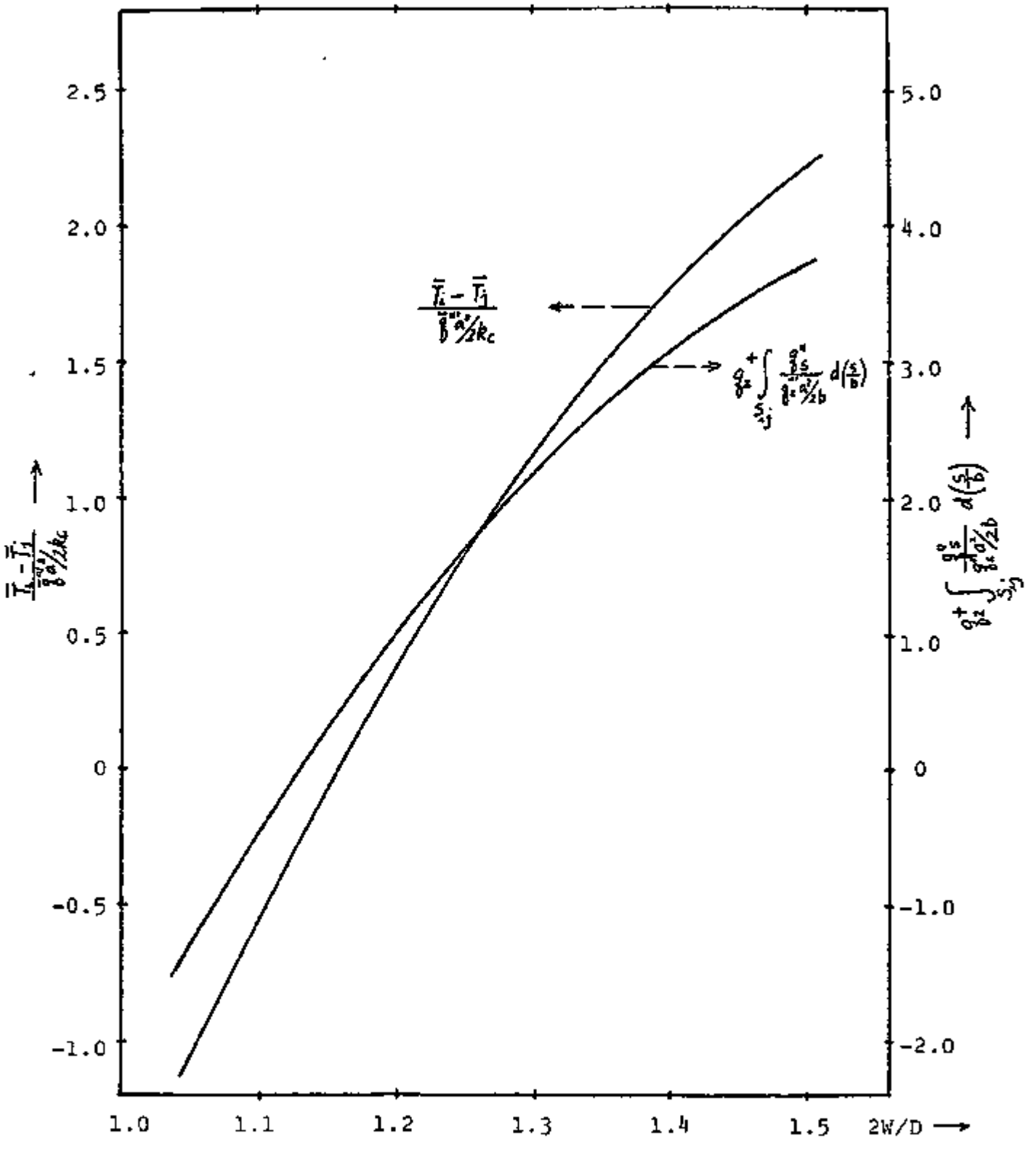

Fig. 3 Normalized Intersubchannel Temperature Difference and and Heat Transport for Multiregion Analysis

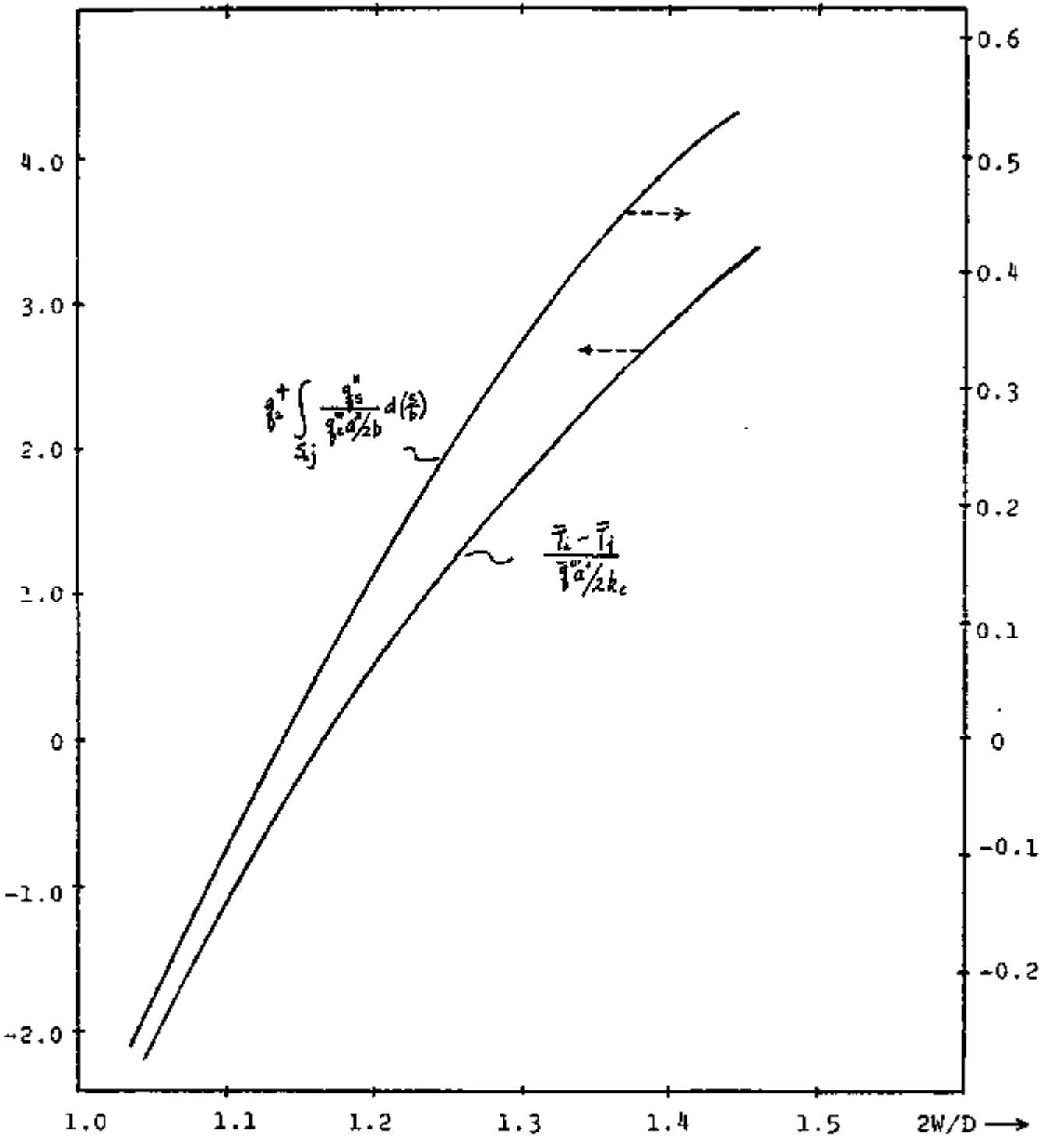

Fig. 4 Normalized Intersubchannel Temperature Difference and Heat Transport for Single Region Analysis

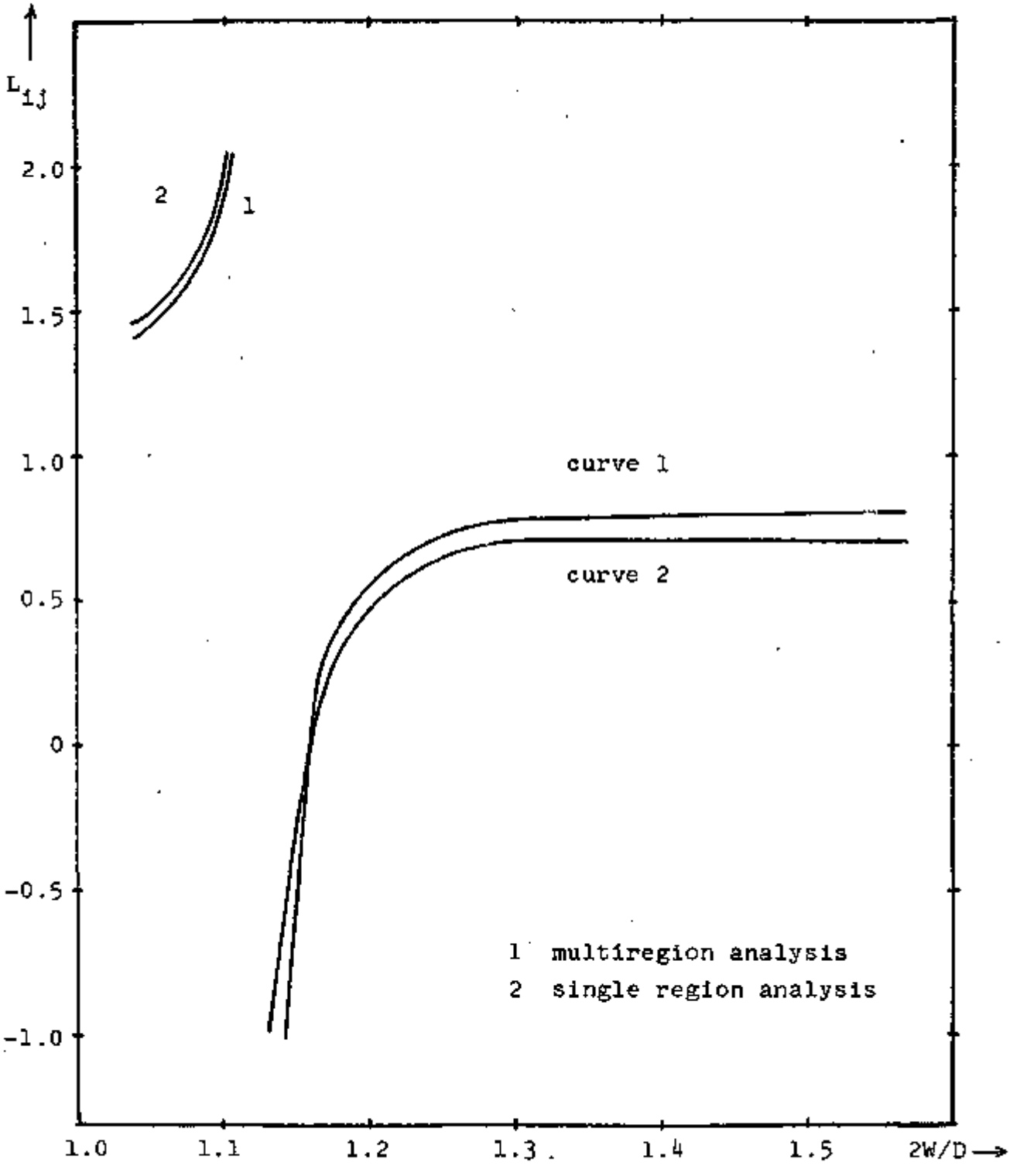

Fig. 5 Correction Factor for Effective Conduction Mixing Lengths of Fuel Bundles

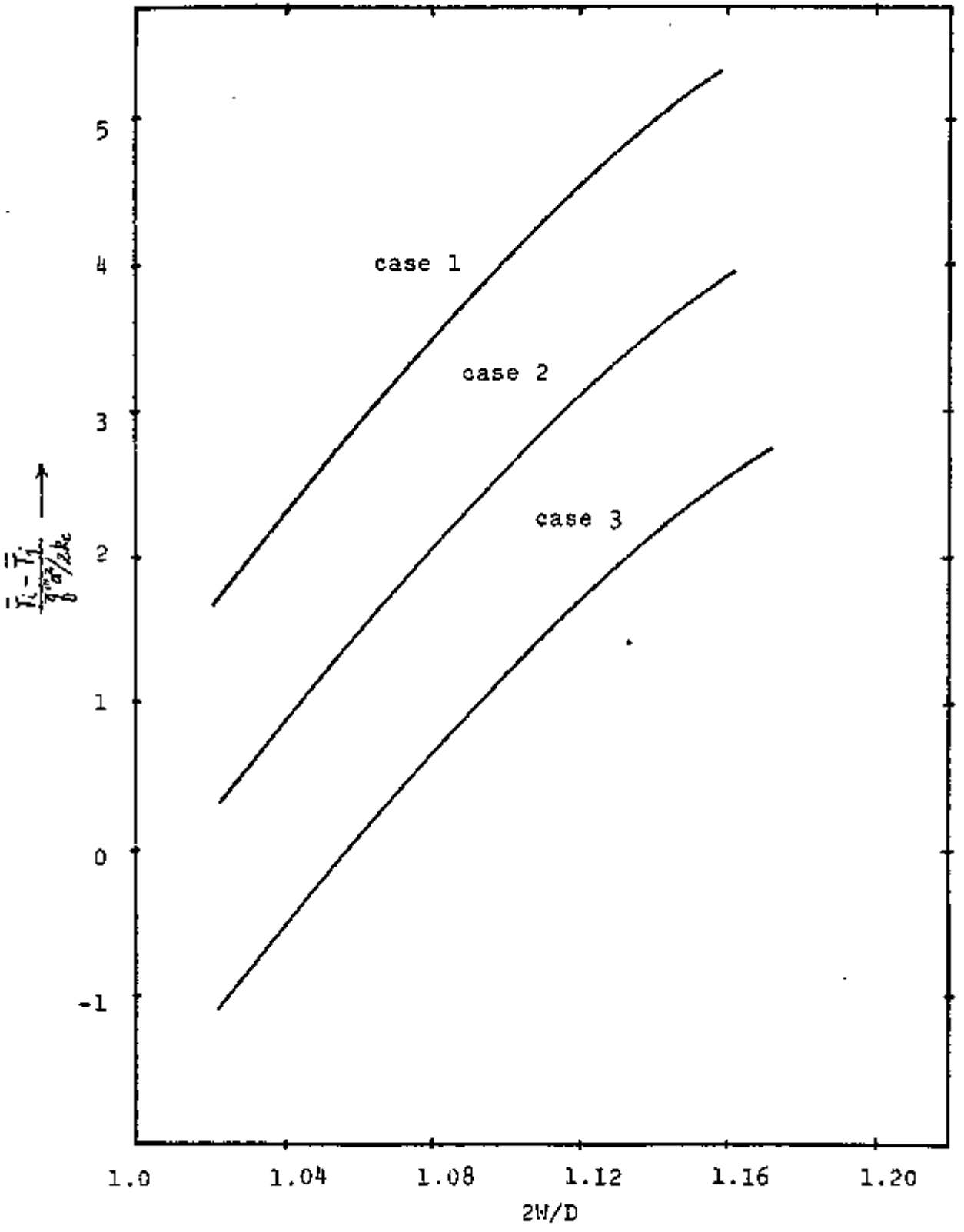

Fig. 6 Normalized Intersubchannel Temperature Difference with Power Tilting

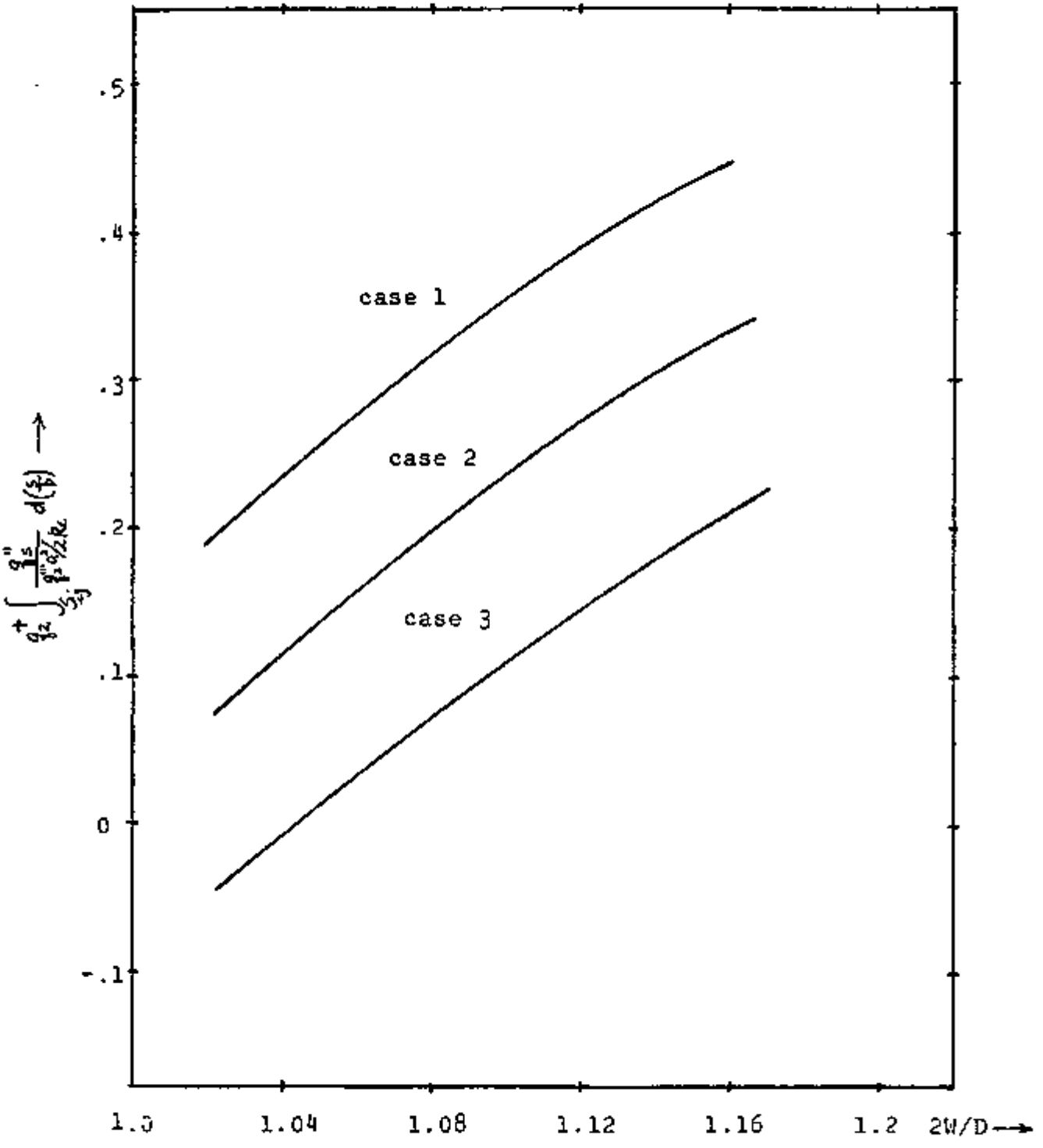

Fig. 7 Normalized Intersubchannel Heat Transport with Power Tilting

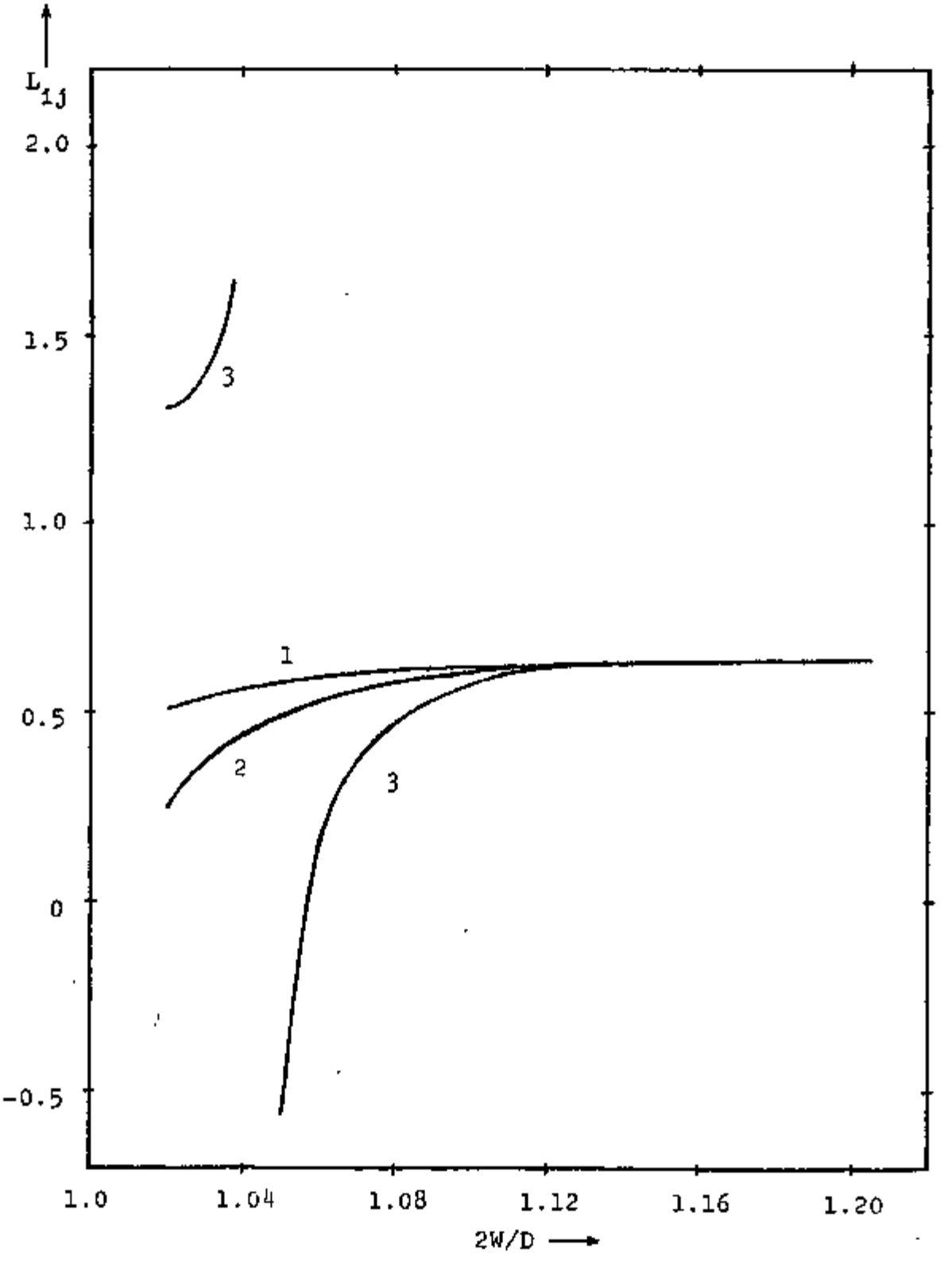

Fig. 8 Correction Factor for Effective Conduction Mixing Lengths for Blanket Assembly with Power Tilting

TABLE 1

POWER PEAKING FACTORS USED IN THE ANALYSIS

CASE	PEAKING FACTOR	
	q_1^+	q_2^+
1	1.1	0.9
2	1.0	1.0
3	0.9	1.1

TABLE 3

Subchannel Averaged Temperature @36" from the Entrance of a 7-Pm LMFBR Bundle

-		$\bar{T}_i$	$\bar{T}_j$	$\bar{T}_i - \bar{T}_j$
$G = 2x10^6 lbm/ft^2-hr$	$L_{ij} = 1.0$	1089.88	994.59	94.29
	$L_{ij} = .70$	1082.11	998.57	83.54
$G = 3x10^6 lbm/ft^2-hr$	$L_{ij} = 1.0$	963.47	893.47	70.0
	$L_{ij} = 0.7$	959.30	895.60	63.7

TABLE 5.2

OPERATING CONDITIONS FOR CØBRA-III CALCULATORS

System pressure = 60 psia

Inlet enthalpy = 365.9 BTU/lbm

Avg. Mass Velocity (G) = 3×10^6 lbm/ft^2-hr

Inlet Temperature = 700° F

Avg. heat flux = $.3 \times 10^6$ BTU/hr ft^2

Uniform power in rods

Uniform heat flux distribution at rod surface

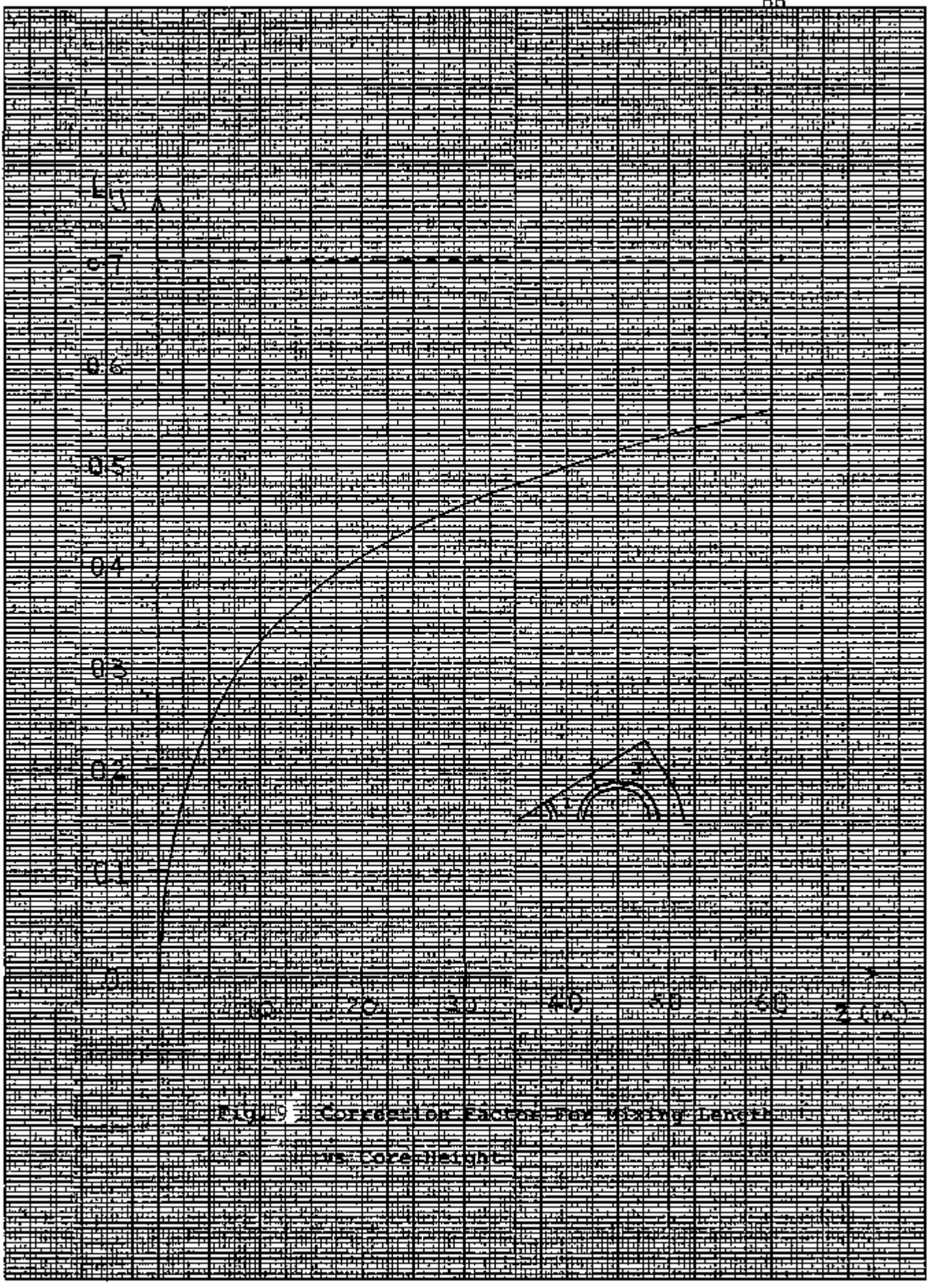

Fig. 9 Correction Factor for Mixing Length vs. Core Height

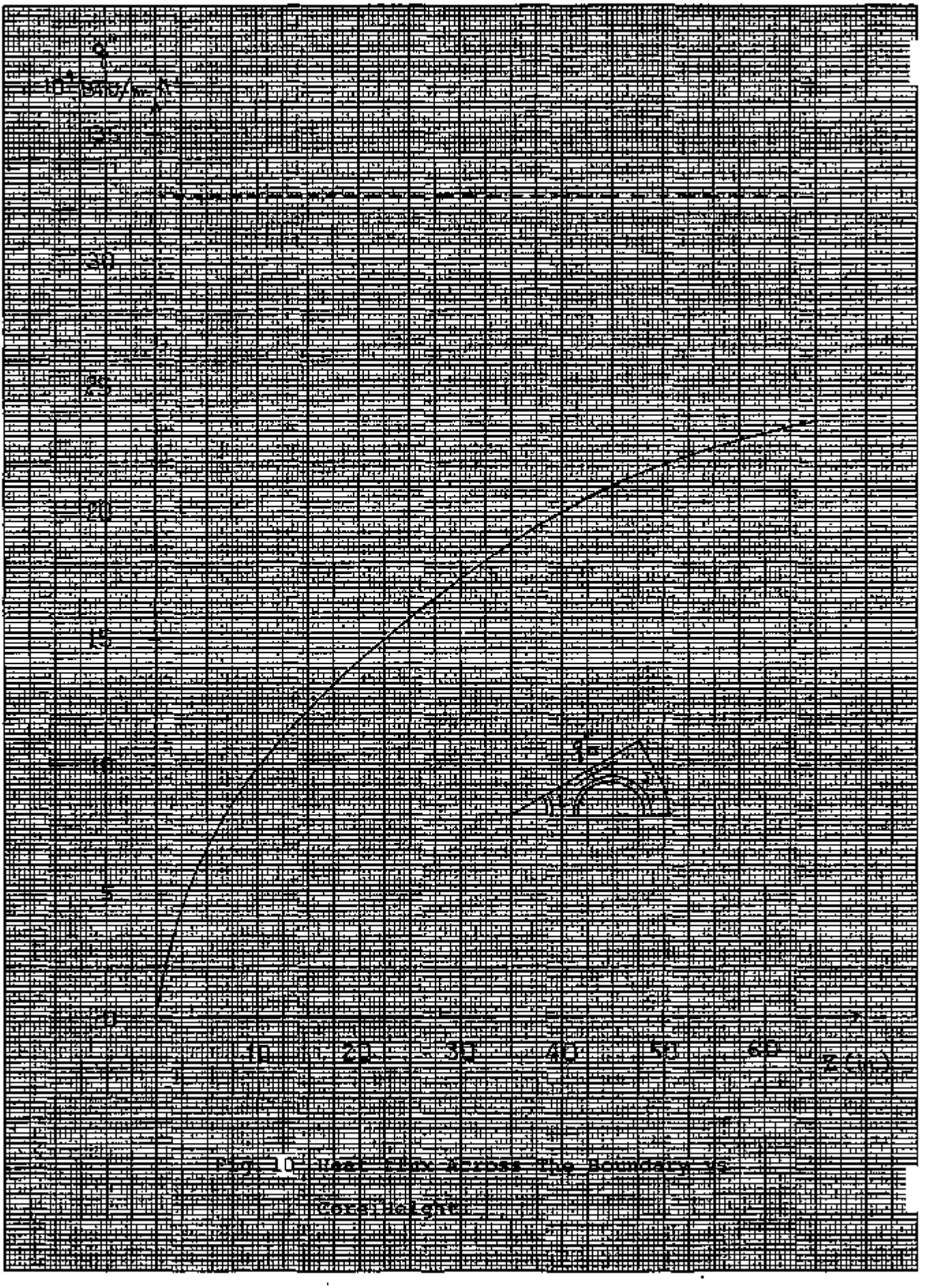

Fig. 10 Heat Flux Across the Boundary vs. Core Height

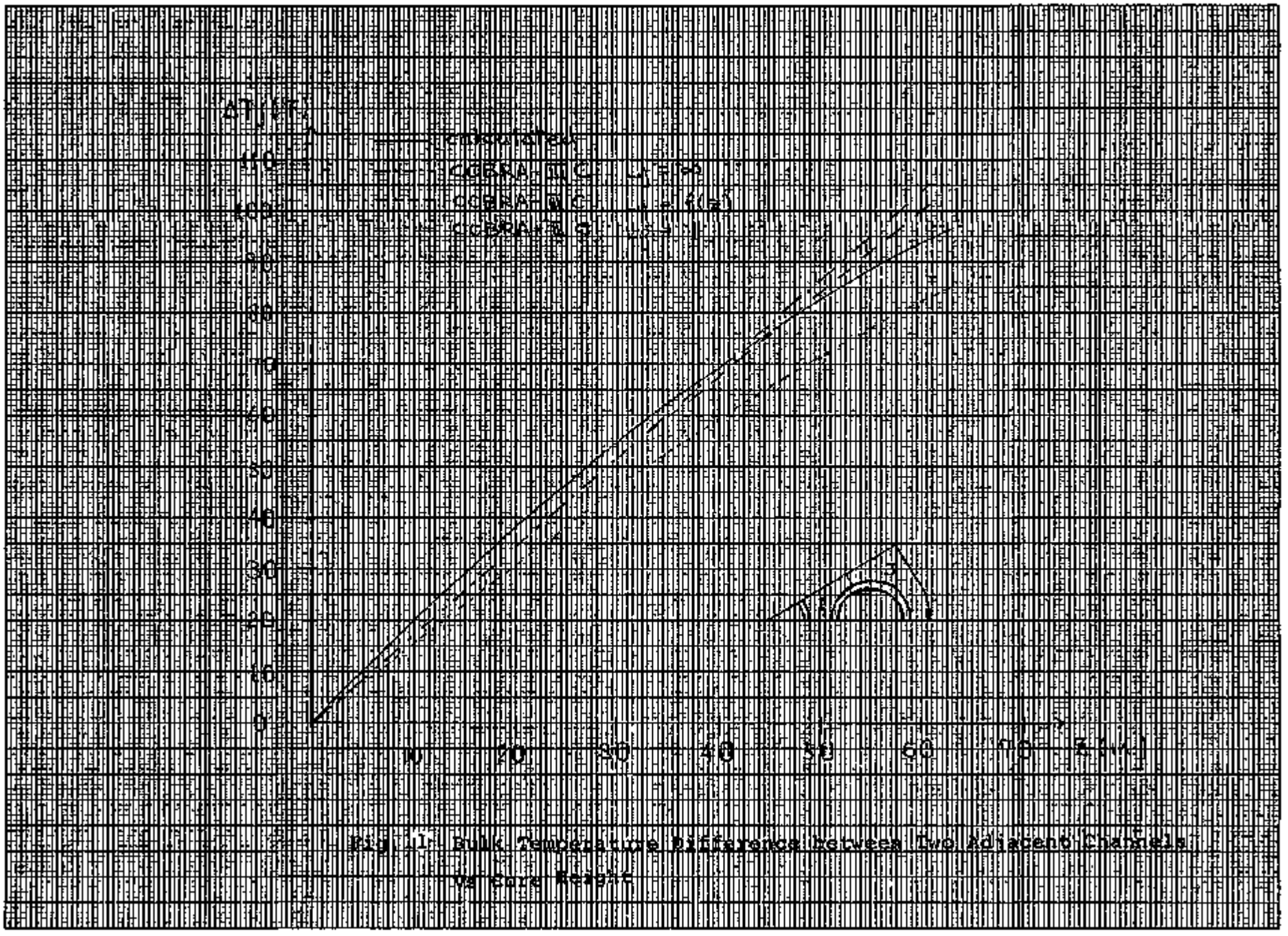

Fig. 11 Bulk Temperature Difference between Two Adjacent Channels vs Core Height

68

Submitted for presentation at the ANS Winter Meeting, 1977, in San Francisco

LAMINAR MIXED CONVECTION HEAT TRANSFER IN FINITE HEXAGONAL BUNDLES

Jong-Yul Kim, Lothar Wolf (MIT)

Recently, low flow conditions in LMFBR bundles have received appreciable attention because of their potential impact upon the thermal-hydraulic design and safety. The purpose of this paper is to present a fully analytical method for predicting the two-dimensional velocity and temperature fields in coolant cells of finite, bare hexagonal fuel and blanket bundles under the condition of fully-developed laminar mixed convection. Momentum and energy equations in the coolant and clad regions are solved simultaneously. Thus, for the first time, a true two-region analysis has been performed by accounting even for possible power tilt effects across the fuel pellet.

Under the assumption of steady-state, thermally and hydrodynamically fully-developed laminar flow and by neglecting viscous dissipation, axial conduction and heat sources in clad and coolant, the dimensionless momentum and energy equations for the coolant regime are

$$\nabla^2\overline{V} + n^4\overline{\phi} = -1 \qquad (1)$$

$$\nabla^2\overline{\phi} - \overline{V} = 0 \qquad (2)$$

respectively, where $\overline{\phi} = \phi/L$ and $\overline{V} = V/L$. Both equations can be combined to give the following biharmonic equation

$$\nabla^4\bar{V} + \eta^4\bar{V} = 0 \qquad (3)$$

The clad temperature field is given by the solution of Laplace's equation, which is well known.

The notation used in the foregoing equations includes:

$C_1 = \frac{\partial T}{\partial z}$: axial temperature gradient

$L = (\partial p/\partial z + \rho_o g)D_h^2/\mu U$: dimensionless pressure drop parameter

$V = \frac{u}{U}$: dimensionless local axial velocity

T_o : reference temperature

U : cell-averaged axial velocity

β : linear volume expansion coefficient

$\eta^4 = Ra = \rho_o^2 g c_p C_1 \beta D_h^2/k_w\mu$: Rayleigh number

$\phi = (t - T_o)k_w/\rho_o U c_p C_1 D_h^2$: dimensionless temperature

The general solution of Eq. (3) can be derived in terms of Kelvin functions as

$$\bar{V} = \sum_{\nu=0}^{\infty} [a_\nu ber_\nu(\eta R) + b_\nu bei_\nu(\eta R) + c_\nu ker_\nu(\eta R) + d_\nu kei(\eta R)] \times [f_\nu \cos(\nu\theta) + g_\nu \sin(\nu\theta)] \qquad (4)$$

where the dimensionless radial coordinate, R, is given by $R = r/D_h$ and θ is the angular coordinate. A similar equation can be obtained for $\bar{\phi}$. The unknown coefficients in the general solutions for $\bar{V}$, $\bar{\phi}$ and t are determined by using the boundary conditions at the polygonal cell boundaries, the clad-coolant interface, the bundle wall-coolant interface and

the inside clad surface. In order to simulate a power tilt across the fuel, the following circumferentially varying heat flux distribution at the inside surface is assumed:

$$q''(q,\theta) = \overline{q''}(H - F\cos\theta) \qquad (6)$$

where H and F are arbitrary multipliers characterizing the heat flux distribution. Whereas all boundary conditions can be satisfied continuously at the inside and outside clad surfaces, this is not possible for those along the polygonal cell boundaries where a point-matching procedure has to be applied on the basis of a preselected finite number of points. This leads to a set of linear equations which can be solved by standard methods. Details of this procedure applied to internal, edge and corner cells are outlined in [1].

The analytical method described above has been extensively tested against available information about buoyancy affected laminar flow in internal cells [2] and fully-developed laminar flow (Ra→0) in edge and corner cells [3]. In both cases excellent agreement has been achieved.

Fig. 1 shows the dimensionless two-dimensional velocity and temperature distributions in a corner cell. The upper part depicts that regimes of near stagnant and even reversed coolant flow exist. The associated coolant and clad temperature fields are shown in the lower part of Fig. 1. A comparison to the laminar flow situation reveals that the temperature gradients are very much equalized due to the beneficial

buoyancy effects. This is even true for large values of F, i.e. large variations of the inside clad heat flux distribution. However, as Fig. 2 depicts, there exists a critical Rayleigh-Number beyond which a sharp decrease in Nusselt-number ($\overline{Nu}$) occurs. $\overline{Nu}$ drops far below its laminar value and under specific conditions even negative values have been observed, indicating again the conceptual weakness of using integral heat transfer parameters in complex flow situations. Due to the fact that $Ra \propto q'/Re$, the designer can avoid this regime by carefully controlling this ratio such that it stays below its critical value.

References

[1] Kim, J.-Y.: Fully-developed Mixed Convection Heat Transfer in Finite Hexagonal Bundles, M.S. Thesis, Dept. Nucl. Engng., MIT, Jan. 1977.

[2] Igbal, M. et al: Buoyancy Effects on Longitudinal Laminar Flow Between Vertical Cylinders Arranged in Regular Arrays, Proc. 4th Int. Conf. Heat Transfer, Paris, 1970, vol. 4, paper No. NC 3.6.

[3] Hsu, C.-J.: Laminar- and Slug-Flow Heat Transfer Characteristics of Fuel Rods Adjacent to the Fuel Subassembly Walls. Nucl. Sci. Engng. 49 (1972), 398-404.

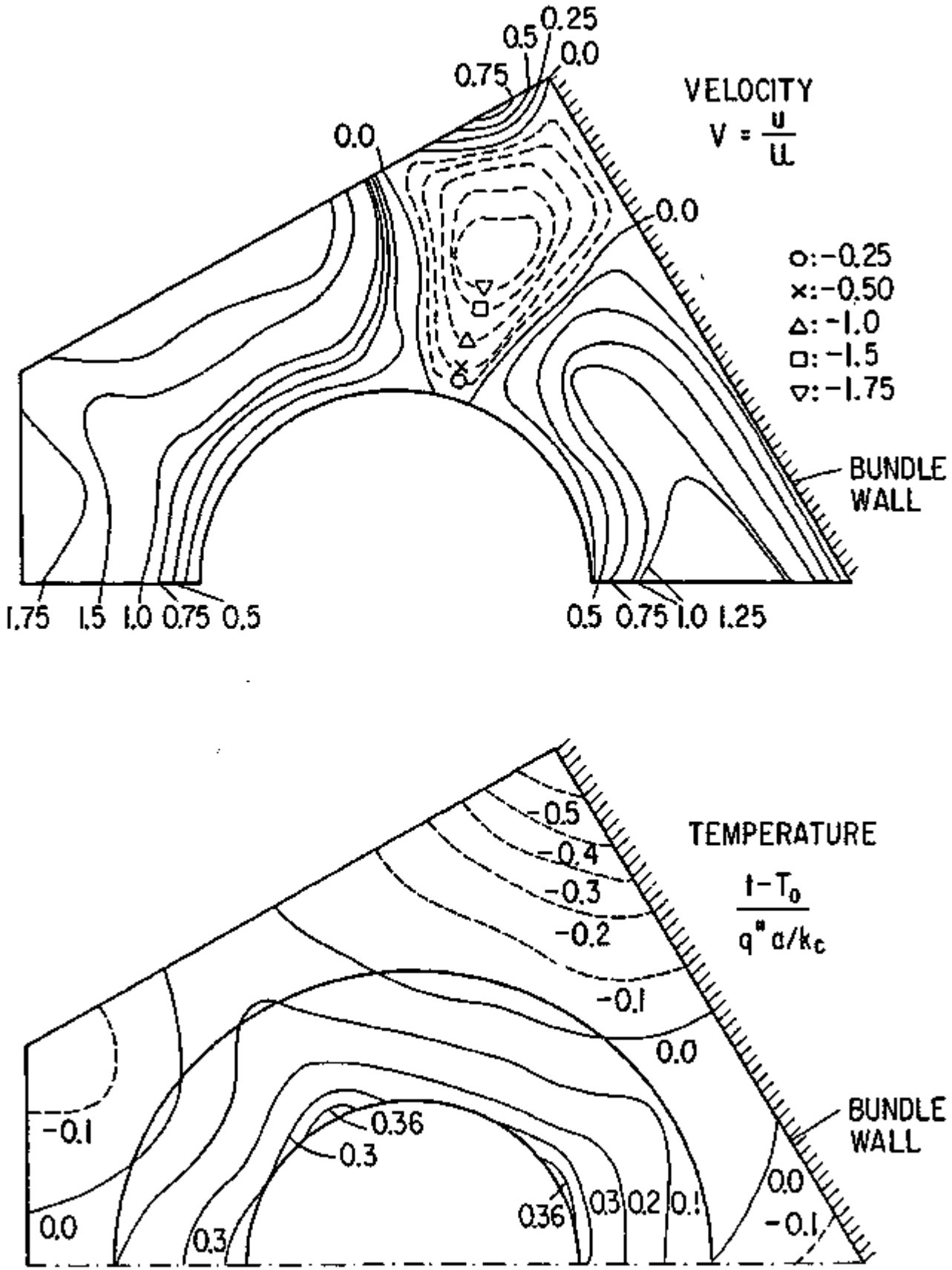

Fig. 1: Isovels and Isotherms in a Corner Cell (Ra = 10^3; P/D = 1.08; 2W/D = 1.125; H = 1.0; F = 0)

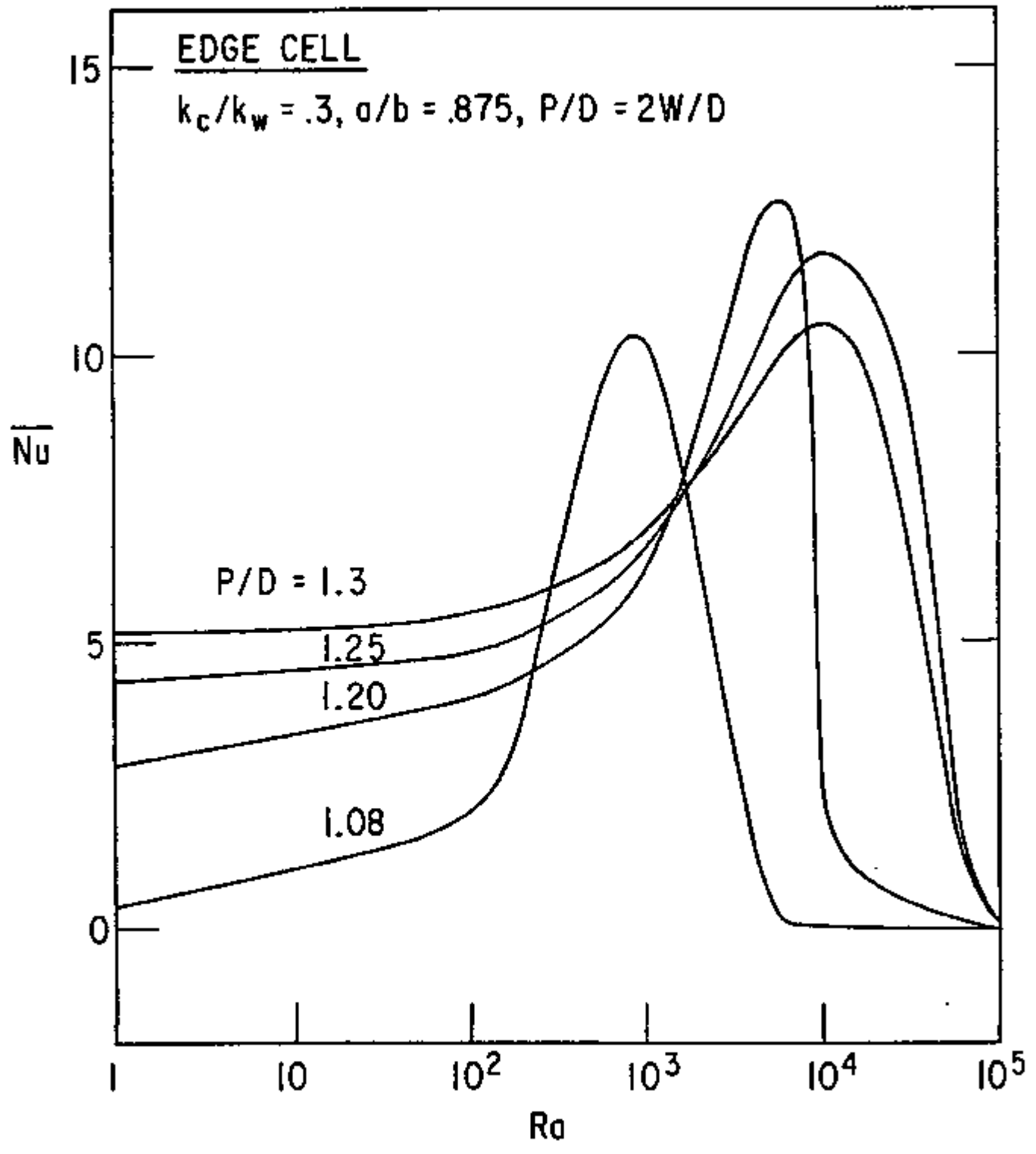

Fig. 2 Average Nusselt-Number vs. Rayleigh-Number in Edge Cells for Various Designs P/D = 2W/D

2-D THERMOELASTIC ANALYSIS OF LMFBR FUEL ROD CLADDINGS

L. WOLF, Ch. N. WONG, M. K. YEUNG

Department of Nuclear Engineering,
Massachusetts Institute of Technology, Cambridge, Massachusetts 02139, U.S.A.

Trans. 4th Int. Conf. SMIRT, San Francisco, 15-19, August, 1977. Vol. C, Structural Analysis of Reactor Fuel and Cladding

SUMMARY

The primary purpose of this study is twofold. Firstly, unique 2-D and 3-D temperature fields for bare finite rod bundles are presented which result from detailed distributed-parameter analyses using the slug flow model. Secondly, these results together with azimuthally varying inside and outside pressure fields are used to derive thermoelastic stress and displacement fields.

The 2-D temperature fields are obtained by an iterative multicell, multiregion technique. Multicell calculations are especially important for studying the pronounced asymmetry effects induced by the coolant cells which are bounded by the bundle wall. The solution takes into account an arbitrary flow split between wall and internal subchannels as well as different heat source densities in the pins. Results indicate that the adiabatic single cell calculation is not conservative under all circumstances as has been previously assumed. Integral mixing transport parameters which account for local temperature variations are quite different from those which are built into the subchannel codes and should be preferred in the future. The pin model used in these studies incorporates the following features:

— tilted power distribution as experienced across blanket rods,
— eccentric pellet position as the most probable pellet location at BOL,
— cracked pellet under higher burnup conditions.

For the first time, these internal pin disturbances are taken into account together with the external disturbances induced by coolant channel asymmetrics. Hot-spot midwall temperatures are shown. Under low flow conditions additional free convention effects come into effect. The fully-developed mixed convection problem is analytically solved for all types of cells in finite bundles. The clad region is fully integrated in this solution, too. The parametric effect of the Ra-number on velocity and temperature fields are shown and a criterion is presented which indicates the onset of local flow reversal.

Due to the fact that LMFBR cores are quite short, thermal entrance effects may play an important role. A 3-D analysis confirms this and shows that thermal conduction predominates in this regime. A comparison with recent liquid-metal cooled 19-pin bundle experiments shows excellent agreement. Mixing parameters which account for the thermal entrance effect are presented. The broad spectrum of local temperature results indicates that 2-D or even 3-D analyses are required to reveal the highest clad midwall temperature which governs the swelling behavior of LMFBR-fuel pin clads. Hitherto used subchannel codes cannot provide this detailed information and should be extended such, as to incorporate a local model in the region of interest.

1. INTRODUCTION

Recent developments of computer codes for the thermal-hydraulic [1] and structural [2] analysis of LMFBR rods indicate a growing need for multidimensional analysis. Seemingly, it has been fully recognized by now that at least two dimensional (r,φ) and (r,z) analyses are absolutely necessary in order to cope with the thermal and structural design constraints of todate's LMFBR rod designs. Actually, 3-D, distributed parameter analyses for fuel, clad, and coolant temperature fields are needed for the reliable design of LMFBR fuel, blanket and absorber assemblies rods to provide the necessary information to accurately evaluate the respective cladding strains which effectively determine the allowable burnup and thus the lifetime of these assemblies. Specifically, the following features should be included in such analyses all of which induce asymmetrical fuel and clad temperature fields.

1. capability to assess the effect of variations in coolant channel geometries specifically those which characterize assembly wall near regions.

2. capability to account for changes in the convective heat transport mode as for instance transition from turbulent to laminar flow heat transfer with and without natural convection effects.

3. capability to assess the effects of power gradients across the rod

4. possibility to account for pellet/cladding eccentricity and ovality as well as pellet cracking.

Certainly, these four disturbances lead to more or less localized increases in the cladding temperatures and cladding strain and hence may increase the clad life damage and thus possibly reduce the allowable burnup and lifetime of the respective assemblies. Furthermore, circumferential gradients support the rod boving process by a structural-thermal-hydraulic feedback effect and thus lead to an undesirably high mechanical rod-grid (wire spacer) interaction with resultant grid (wire spacer) assembly wall interactions.

Although the individual contributors enlisted above have long been recognized, their effects upon the cladding temperature have been studied only under various simplifying assumptions thus far. Most of these studies [3,4,5] thermally decoupled the heat transport between rod and coolant by using the concept of the heat transfer coefficient. Thus, the superior circumferential heat transport in the coolant has never been taken into account in the past. On the other hand, these procedures disregarded the additional disturbance induced by the asymmetrical coolant channel geometry. Thus, it is not clear whether the results of these former studies constitute a conservative or non conservative basis. The only way to find out is to treat all disturbances simultaneously as the present study does because it is thought that under certain circumstances the combined effect of variations in the source, sink and boundary conditions may lead to an amplification of circumferential cladding temperature variations.

Todate's design methods for evaluating rod temperatures heavily rely upon the use of lumped-parameter subchannel codes such as COBRA-III C [6] and the

lize, which determine the bulk coolant temperatures in the subchannels across an assembly as function of the axial location. The temperature of the hottest subchannel around a rod is used then to perform a one-dimensional radial heat transport analysis through the rod by employing the concept of the heat transfer coefficient to derive the cladding temperature. Recently, some methods emerged which take the different bulk temperatures of the subchannels surrounding the rod of interest and employ those as boundary conditions in a two-dimensional thermal analysis of the rod by assuming a constant heat transfer coefficient between the cladding and the coolant. It is worth mentioning that this procedure in even a more advanced form has been already been applied in 1971 [7] Naturally, although a step forward as compared to the one-dimensional analysis, this remains quite a crude approximation because as already shown by various authors in the past the concept of the heat transfer coefficient breaks down in cases where the defining variables are themselves strong functions of the independent variables Exactly this has to be expected however in assemblies with very tight pitch-to-diameter ratios such as blanket and absorber assemblies. Yet, due to the lack of more detailed information the aforementioned procedure seems to be the only choice to use the data supplied by subchannel codes right now. Additional insight can only be gained from distributed parameter methods. Due to their complexity the application of these methods have to be restricted to a limiting number of coolant cells surrounding the rod of interest Thus, in order to obtain meaningful results in the framework of an assembly analysis future efforts should be devoted to develop symbiotic hybrid methods for combined lumped and distributed parameter analysis A step towards this goal has been undertaken in the present study by interpreting the free unknown in the analytical solution in terms of the bulk temperature which can be supplied by subchannel codes for different axial locations.

Besides of providing directly deterministic local peak temperatures which can be fed into todate's probabilistic design tools for checking the calculated values against the design limits, the distributed parameter methods can be used to generate more reliable integral parameters for updating the effective mixing coefficients for the various transport phenomena incorporated into the subchannel codes. Thus far, only limited informations are available mainly for coolant regions inside an assemblies. However, nothing is known for coolant regions close to the assembly wall, despite the fact that the latter are of more importance for the thermal analysis due to the strong geometrical asymmetries in these regions. The present study will present effective conduction mixing lengths for the corner cells of hexagonal bundles

Thus far, two-dimensional temperature fields have been mostly used in connection with thermalelastic cladding analyses [3,7,8] A recent study [9] of clad ovalities as found during post-irradiation examination confirmed that this is not necessarily a bad choice in the first place. At least, deformations agreed very well with the experimental evidence although the

calculated stresses turned out to be twice the yield strength. Because thermoelastic analysis is the first logical choice entering the structural field it was decided to work with the codes described in [3,7] to determine the radial and tangential displacements. Due to the fact that the thermoelastic strains alone are unrealistically high the GRO-II code [10] is used to perform an order of magnitude analysis for the nonlinear effects. For this purpose the highest cladding midwall temperature as determined by the 2-D or 3-D thermal analysis has been used as input into this one-dimensional structural analysis code. Finally, this present study uses the two-dimensional nonlinear structural analysis code GOGO [2] to check the approximate results obtained by GRO-II and to obtain more detailed results for the local phenomena. GOGO is the only 2-D code in r-ϕ geometry known to the authors which handles all nonlinear effects relevant to LMFBR operational conditions within an affordable amount of computational efforts. It is worth mentioning that the original version of this code contained a very crude approximation of the clad temperature variation of a corner pin which has been changed for the present analysis according to the newly derived analytical results. Due to the limited space available only highlights of the basic findings of the whole study can be reproduced in the following figures. More details will be disclosed during the presentation and in follow-on publications [11,12].

2. ANALYSIS

2.1. Thermal Analysis

In what follows, short descriptions will be given about the underlying principles for two 2-D and one 3-D thermal-hydraulic analyses in typical subsections of hexagonal LMFBR assemblies.

2.11 2-D Multicell, Multiregion Slug Flow Heat Transfer Analysis

Thus far, only single cell, multiregion analyses have been reported for coolant regions close to the assembly wall [13] (see Fig. 1), although some progress has been made in the past to couple several internal cells in two [1] and three dimensions. However, despite of the value of the basic findings in this geometry the more interesting regions with respect to design are the outer coolant cells such as the corner cells (see Fig. 1) and the side cells. Multicell analyses are necessary in order to avoid the adiabatic boundary conditions around the polygonal sides of the coolant cells to study the propagation of disturbances across cell boundaries either from inside the bundle due to power skews and/or outer regions dus to assembly wall effects. In order to perform efficiently a multicell analysis for a rod bundle or sections thereof it is essential to develop a scheme which can uniquely identify any individual unit cell as a function of the cell number. For this purpose, a double index system (m,n) has been developed [14], where the first index indicates the number of rows from the center of the bundle and the second one designates the distance between the cell center and the normal to the bundle wall in terms of number of pitches. By virtue of this system each cell and more important the types of its neighbors can be automatically identified.

The present st
turbulent ligu
for fuel, clad
bundle under t
For this purpo
the separate a
discontinuity
two cells. An
atically this
continuity alo
shown in Fig.
corner cell -

$$T_i^{(o)}(p,$$

whereas for ce
sented by

$$T_j^{(o)}(p,$$

The superscrip
solutions an u
derived which
tribution alon
the neighborin
second iterati
so forth. In
channel codes
cell temper
evaluation of
effective con
channel codes.

$$l_{ij} =$$

For practical
distance betwe

$$l_{ij} =$$

However, this
evaluates a co

The present study adopts the slug flow heat transfer as an approximation to turbulent liquid-metal heat transfer. The multiregion temperature solutions for fuel, clad and coolant are derived for all types of cells in a finite bundle under the assumption of adiabatic conditions around the cell boundaries. For this purpose the solutions presented in [13] have been adopted. Naturally the separate adiabatic calculations of different cells result in temperature discontinuity along the imaginary matching boundary in the coolant between the two cells. An iterative method has been developed [12] which removes systematically this temperature difference by imposing the condition of heat flux continuity along the same line. The scheme can be explained for the geometry shown in Fig. 1 as follows. For the coolant temperature field of cell i - the corner cell - the adiabatic solution reads

$$T_i^{(o)}(\rho,\phi) = A_i + \frac{q_i''' a^2}{2k_3} \theta_j(\rho,\phi) \quad , \tag{1}$$

whereas for cell j - the internal cell - the coolant temperature is represented by

$$T_j^{(o)}(\rho,\phi) = A_j + \frac{q_j''' a^2}{2k_3} \theta_j(\rho,\phi) \tag{2}$$

The superscript o denotes the zeroth iteration. Starting with these initial solutions an updated coolant temperature field for the corner cell can be derived which is followed then by a calculation of an updated heat flux distribution along the common boundary. This is used as boundary condition for the neighboring cell which in turn leads to a new temperature field. The second iteration starts with the updated temperature boundary condition and so forth. In order to relate the outcome of this study to the results of subchannel codes a unique relationship for the differences of the average coolant cell temperatures has been established. This difference together with the evaluation of the heat transferred across the common cell boundary yields the effective conduction mixing length scale, l_{ij}, which is employed in subchannel codes. l_{ij} is given by

$$l_{ij} = k \frac{S_{ij}(\bar{T}_i - \bar{T}_j)}{\int_{S_{ij}} q_i'' \, ds} \tag{3}$$

For practical purposes, l_{ij} is usually set equal to the centroid-to-centroid distance between subchannels, l_{ij}^*, i.e.,

$$l_{ij} = l_{ij}^* \quad . \tag{4}$$

However, this assumption is not valid at all. Therefore, the present study evaluates a correction factor, L_{ij}, given by

$$L_{ij} = \frac{l_{ij}}{l_{ij}} = k \frac{S_{ij}}{l_{ij}} \frac{(\bar{T}_i - \bar{T}_j)}{\int_{S_{ij}} q''_i \, ds} \qquad (5)$$

where S_{ij}/l_{ij} can be simply expressed in terms of geometrical parameters alone as

$$\frac{S_{ij}}{l_{ij}} = \frac{\frac{1}{2}\left[\frac{P}{D} - \frac{1}{4}\right]}{\left[\frac{\frac{1}{16}\left(\frac{2W}{P}\right)^2\left(\frac{P}{D}\right) + \frac{1}{24\sqrt{3}}\left(\frac{2W}{D}\right)^3 - \frac{1}{16}}{-\frac{1}{4}\left(\frac{P}{D}\right)\left(\frac{2W}{D}\right) + \frac{1}{6\sqrt{3}}\left(\frac{2W}{D}\right)^2 - \frac{1}{12}} * \frac{\frac{1}{2}\left(\frac{P}{D}\right)^3 - \frac{\sqrt{3}}{12} * \left(\frac{P}{D}\right)}{\sqrt{3}\left(\frac{P}{D}\right)^2 - \frac{1}{2}} * \right] \qquad (6)$$

By virtue of the above procedure distributed parameter methods can provide meaningful informations for use in today's design codes and thus may help to improve the reliability of their results in cases where a priori no experimental evidence is available for tuning purposes.

In order to account for the additional effects of pellet eccentricity and cladding ovality the analytical formulation presented in [3] has been iteratively tied together with the present analysis.

2.12 3-D Single and Multicell, Single Region Slug Flow Heat Transfer Analysis

The analysis presented in the proceding section assumes thermally fully-developed conditions. Due to the high asymmetry effects induced by the corner and side cells and the relatively small core heights it may be argued that this assumption is invalid in reality. In order to check this a three-dimensional slug flow heat transfer analysis has been conducted on the basis of the analysis performed in [15]. The overall solution can be split into a fully developed part and an entrance solution part. The latter is given in general information form as

$$\vartheta_e(\rho,\phi,\xi) = \sum_{n=0}^{\infty}\sum_{m=1}^{\infty}\left[C_{n,m}J_n(\beta_m\rho) + D_{n,m}Y_n(\beta_m\rho)\right] E_m e^{-\beta_m^2\xi}\cos n\phi \qquad (7)$$

The assumption of slug flow under these circumstances seems to be quite justified because heat conduction constitutes a major part of the overall heat transport for liquid-metal flow in the entrance region especially for low and moderate flow conditions. Whereas the analysis in [15] was limited to a single cell, the present study extended the analytical procedure to analyze the coupled behavior of two cells as shown in Fig. 1. Due to the vastly different entrance region behavior of internal and corner cells special attention had to be devoted to minimize the numerical interior and boundary least square

errors introduced at the inlet section by satisfying the boundary condition of constant temperature over the total inlet cross-sectional area. Due to the fact that this analytical analysis is solely confined to the coolant region the assumption of constant heat flux around the outer cladding surface has been introduced. This simplification leads to conservative results for the circumferential cladding temperature variation due to the neglection of the azimuthal heat conduction effects in the cladding. Arbitrarily varying heat flux distributions in the axial direction are handled by Duhamel's superposition principle.

2.13 Fully-Developed, Single Cell, Two-Region Analysis of Laminar Mixed Convection Heat Transfer

Under low flow conditions as experienced in recent blanket assembly designs or in case of loss-of-flow in either fuel and/or blanket assemblies the assumption of turbulent flow and hence the slug flow approximation is certainly invalidated. The transition to laminar flow is accompanied by a substantial deterioration of the heat transfer from the rod to the coolant which may lead to an even higher circumferential cladding temperature variation. Therefore, the designer is very much interested to find out whether a superimposed natural convection effect may help to avoid the very low heat transfer regime. In order to study the mixed convection capabilities of typical unit cells in finite, hexagonal bundles with respect to local as well as average quantities a two-region analysis has been performed [16]. The general solutions for the temperature fields in the coolant and cladding assume the following forms, respectively

$$t_{c0}(r,\phi) = -\frac{1}{\eta^4} + \frac{1}{\eta^2} + \sum_{n=0}^{\infty} [a_{sn}\,bei_{sn}(\eta r) - b_{sn}\,ber_{sn}(\eta r) + c_{sn}\,kei_{sn}(\eta r) - d_{sn}\,ker_{sn}(\eta r)]\cos(sn\,\phi) \tag{8}$$

$$t_{c1}(r,\phi) = A_0 - \frac{\bar{q}''' H}{k_3}\,a^2 \ln r + \left[A_1 + \frac{a^2}{r^2}\left(A_1 - \frac{\bar{q}''' F}{k_3}\right)\right] r\cos\phi + \sum_{n=2}^{\infty} r^n\left[1 + \left(\frac{a}{r}\right)^2\right] A_n \cos(n\phi) \tag{9}$$

The coefficients in these equations are found by simultaneously solving these equations together with the general solution for the velocity field when substituted into the various boundary conditions. It is worth mentioning that Eq. (9) accounts for an azimuthally varying heat flux distribution at the cladding inside surface, thus simulating a power tilt across the fueled region.

2.2 Thermoelastic and Inelastic Analyses

The thermoelastic analyses are performed by using the methods in [1] and [8]. The former incorporates the possibility to account simultaneously for either pellet eccentricity or cladding ovality together with a superimposed

power tilt across the fueled region whereas the latter one performes a Fourier series analysis of the inside and outside cladding temperatures which have to be supplied as input. The majority of the inelastic studies is performed using the GRO-II code [10] which uses the thin shell approximation. The GOGO-code [2] is used to provide two-dimensional inelastic informations.

3. RESULTS AND DISCUSSION

Most results are obtained for a typical average corner pin of a fuel assembly and a peak corner pin of a blanket assembly for the CRBPR. Figure 2 shows the effect of a typical power tilt across the assembly upon the cladding temperature variation of the corner pin. Under the given circumstances the least variation can be expected when the tilt is decreasing towards the assembly center. Figure 3 demonstrates the quite different temperature variations in the individual unit cells as derived by a four-cell calculation. It is interesting to notice that the cladding temperature variation of cells 2 and 3 are about the same although both represent different locations within the assembly. Figure 4 represents the correction factor L_{ij} as function of the dimensionless wall distance for a given P/D. Obviously, L_{ij} deviates quite substantially from 1 which means that the common assumption of using the centroid-to-centroid distance as effective conduction mixing length is incorrect. Under extreme conditions the direction of the heat flow is even reversed. Figure 5 comprises a comparison between the 3-D slug flow heat transfer analysis and experimental evidence [17] as measured in a sodium cooled 19-rod bundle. Despite the stringent assumptions built into the analysis the agreement can be considered as quite satisfactory. In order to show the effect of coupling two different cells together, Fig. 6 compares the results of a single cell to a two-cell calculation. The "bump" in the cladding temperature which shows up at about 120 degrees can be attributed to the additional heat flow out of the internal cell into the corner cell. Overall, the comparison to two-dimensional calculations show that these overpredict the cladding temperature variations by about a factor of two. Thus, the 3-D calculations are necessary and meaningful to derive a scaling factor in order to realistically apply the 2-D results presented before. Figures 7 through 9 summarize some of the findings of the mixed convection study. It is obvious that for higher Ra-numbers the velocity field gets highly distorted and that locally coolant regions with downflow exist. Naturally, this affects both local and average thermal quantities as shown in Figs. 8 and 9. It is interesting to notice that $\overline{Nu}$ after increasing over a certain Ra-number range rapidly decreases beyond a certain critical Ra-number and assumes values which are lower than those for laminar convection only. As indicated these effects are strongly dependent upon the cell geometry.

Figures 11 through 13 summarize the results of the two-dimensional thermo-elastic analysis whereas Figs. 14 and 15 depict the results of the one-dimensional inelastic analysis using the GRO-II code. The temperature

distributic
the blanke
placement c
wall distan
wall. Over
interior re
already ch
lead to e
experience
Here the re
tion of u i
the tangent
in Fig. 12.
and 120 de
stress dis
by the two

Figur
the total
porated
by an ave
aforement
creep is e
for the av
approximat
variation
the minimu
depicts th
of 20% CW
region of
than the c
fuel the o
from 8% h
Annealed
than the
From an ov
Naturally,
material p

ACKNOWLEDG
The e
U.S. ERDA.

REFERENCES

[1] CHUAN
Blank

distributions which were used as input are shown in Fig. 10 for the fuel and the blanket assembly. The blanket rod experiences about twice the radial displacement of the fuel rod. The circumferential variation is largest for large wall distance and in case that the power tilt is directed towards the assembly wall. Overall, these results suggest that the corner rod moves towards the interior rod and hence reduces the coolant areas in a regime which is already characterized by higher temperatures. Thus, this feedback effect will lead to even higher temperatures at 180 degrees. The least variation is experienced in case that the wall distance is slightly less than P/D = 1.08. Here the rod closes the gap towards the side pin. The circumferential variation of u is substantially lower for the fuel rod. The largest variation in the tangential displacement occur for the large wall distance design as shown in Fig. 12. The maximum of v is located at an angular position between 110 and 120 degrees. Figure 13 demonstrates that the variation of the tangential stress distributions of all cases considered for the blanket rod are bounded by the two cases studied for the fuel rod.

Figures 14 and 15 show the effects of different temperature levels upon the total creep in blanket and fuel rods. Due to the simple approach incorporated in GRO-II it has been assumed that the rods are characterized either by an average temperature or by the maximum midwall temperature found by the aforementioned 2-D thermal analysis. As can be seen from the figure, the creep is about an order of magnitude higher for the maximum temperature than for the average one. The circumferential variation of the cladding creep is approximately bounded by the two lines given in the figure. Obviously this variation increases with burnup. This increase might be even larger because the minimum cladding temperature stays below the average one. As Fig. 15 depicts the fuel rod shows a similar behavior over most of its burnup in case of 20% CW 316 SS as cladding material. There again the high temperature region of the cladding circumference will creep more by an order of magnitude than the cooler parts. However, starting halfway through lifetime of the fuel the overall circumferential variation in creep behavior decreases and from 8% burnup on the fuel rod cladding nearly creeps in a uniform fashion. Annealed 316 SS behaves quite differently. There the cooler parts creeps more than the hotter ones and the difference keeps obviously growing with burnup. From an overall design point of view this might be a desirable feature. Naturally, the reported results heavily rely upon the correlations for the material properties built into GRO-II.

ACKNOWLEDGEMENTS

The authors appreciate the financial support for this study by the U.S. ERDA.

REFERENCES

[1] CHUANG, M.C., "Cladding Circumferential Hot Spot Factors for Fuel and Blanket Rods," Nucl. Eng. Design 35, 21 (1975).

[2] SIM, R.G., GOGO User's Manual," GEAP-13968 (1973).

[3] WOLF, L., "Thermo-Elastic Stresses in Fuel Element Clads Due to the Combined Effects of Flux Tilt in the Fuel and Circumferential Variations of Boundary Conditions," Proc. 2nd Int. Conf. SMIRT, Berlin, Germany (September 10-14, 1973), Paper C314.

[4] NIJSING, R., "Temperature and Heat Flux Distribution in Nuclear Fuel Element Rods," Nucl. Eng. Design, 4, 1 (1966).

[5] GODESAR, R., "Influence of Azimuthal Perturbation of Heat Transfer in the Gap on Design and Irradiation Behaviour of Fuel Pins," Proc. Int. Conf. Physical Metallurgy of Reactor Fuel Elements, CEGB, 1973, 308-314

[6] ROWE, D.S., "COBRA-IIIC: A Digital Computer Program for Steady State and Transient Thermal-Hydraulic Analysis of Rod Bundle Nuclear Fuel Elements," BNWL-1695 (May 1973).

[7] FISCHER, M., HOFMANN, F., KRIEG, R., "Mechanical Loads of Claddings by Azimuthal Temperature Gradients in Fuel Pins with Eccentric Geometry," (in German), Proc. 1st Int. Conf. SMIRT, Berlin, Germany, September 20-24, 1971, Paper C212.

[8] CROZIER, R.J.M., "SEGPIPE: A Program to Determine Thermo-Elastic Deformations in a Segment of a Hollow Cylinder," AECL-4056 (1971).

[9] KERRISK, J.F., BARNER, J.O., PETTY, "Cladding Ovalities in Advanced Liquid-Metal Fast Breeder Reactor Fuel Elements," Nucl. Technology 30, 361 (1976).

[10] PATEL, M., WHITE, D.E., "GRO-II: A Simplified Method for Predicting Mixed Oxide Fuel Rod Performance During Normal Operation," GEAP-14051 (1975).

[11] KARIMI, R., "Two-Dimensional Inelastic Cladding Loading Sensitivity Analyses," M.S. Thesis, Dept. Nucl. Engng., MIT, to be published

[12] YEUNG, M., "Multicell Fluid Flow and Heat Transfer Analysis in Rod Bundles," Ph.D. Thesis, Dept. Nucl. Engng., MIT, to be published.

[13] WOLF, L., JOHANNSEN, K., "Two-Dimensional, Multiregion Analysis of Temperature Fields in Finite Rod Bundles Cooled by Liquid Metals," Proc. 1st Int. Conf. SMIRT, Berlin, Germany, September 20-24, 1971.

[14] Progress Report: "Coolant Mixing in LMFBR Rod Bundles and Outlet Plenum Mixing Transients," Dept. Nucl. Engng., MIT COO-2245-31 (1976).

[15] MEIER, S., "An Analytical Solution for the Temperature Fields in Liquid-Metal Cooled Fuel Pin Bundles with Arbitrary Axial Heat Flux Profile," (in German) Ph.D. Thesis, Institut für Kerntechnik, Berlin, Germany, TUBIK-37, 1974.

[16] KIM, J.Y., "Fully-Developed Mixed Convection Heat Transfer in Finite Hexagonal Bundles," M.S. Thesis, Dept. Nucl. Engng., MIT (Feb. 1977).

[17] MÖLLER, R., TSCHÖKE, H., "Experimental Determination of Temperature Fields in Sodium-Cooled Pin Bundles," (in German), Nucl. Conf., Düsseldorf, Germany, 1976.

Fig. 2 Effec
the Re
Corne

Due to the
ncial Variations
lin, Germany

Nuclear Fuel

Transfer in the
roc. Int. Conf.
, 308-314

Steady State and
ar Fuel Elements,"

of Claddings by
ric Geometry,"
y, September 20-

o-Plastic Deforma-
51).

in Advanced
Technology

Predicting
," GEAP-14051

Sensitivity
ublished

ysis in Rod
ublished.

Analysis of
id Metals,"
20-24, 1971.

nd Outlet Plenum
(1976).

Fields in Liquid-
Flux Profile,"
lin, Germany.

fer in Finite
T (Feb. 1977).

Temperature
Conf.,

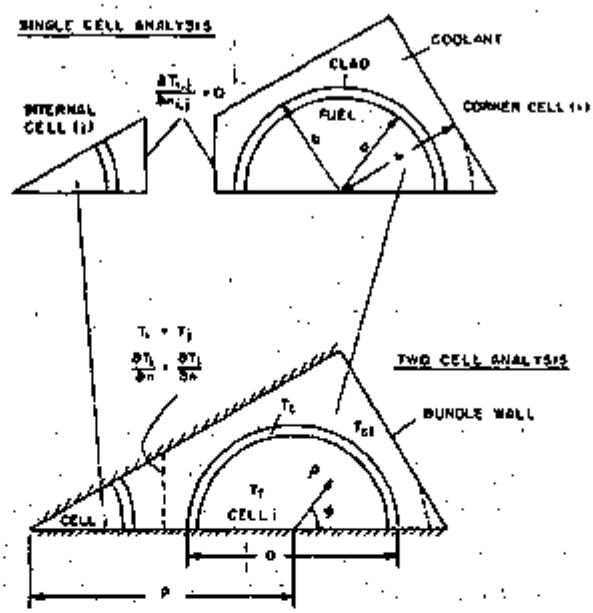

Fig. 1 Single Cell and Two Cell Geometries.

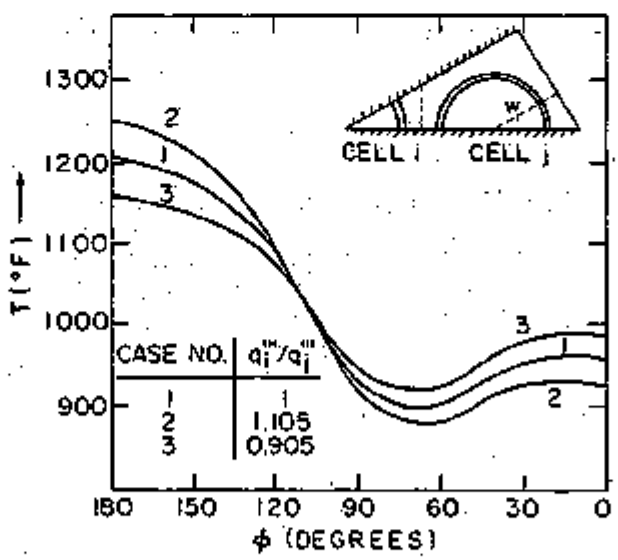

Fig. 2 Effect of Different Power Generation Rates in Adjacent Fuel Pins of the Radial Blanket Upon Outside Clad Temperature Distribution of the Corner Pin ($\bar{T}_{clad}$ = 1000°F)

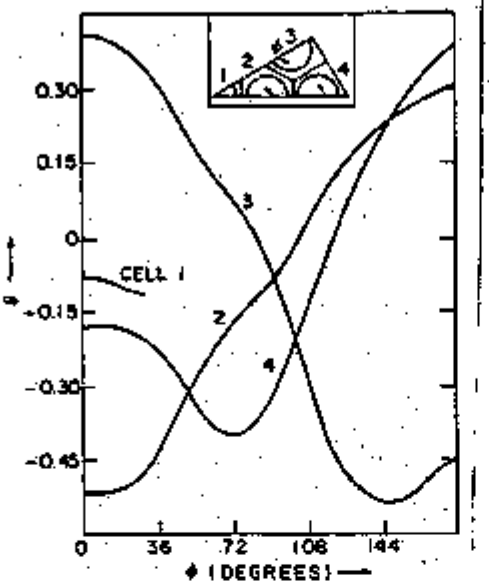

Fig. 3 Dimensionless Outside Clad Temperature Distributions as Calculated by a Four-Cell Analysis (P/D = 1.205; 2W/D = 1.2)

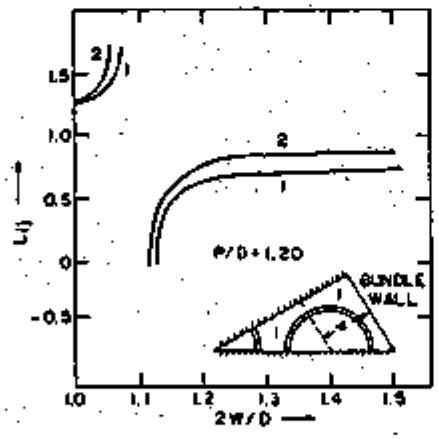

Fig. 4 Dimensionless Effective Conduction Mixing Length L_{ij} as Function of 2W/D for: 1) Azimuthally Uniform Heat Flux at Outside Clad Surface
2) Multiregion Analysis

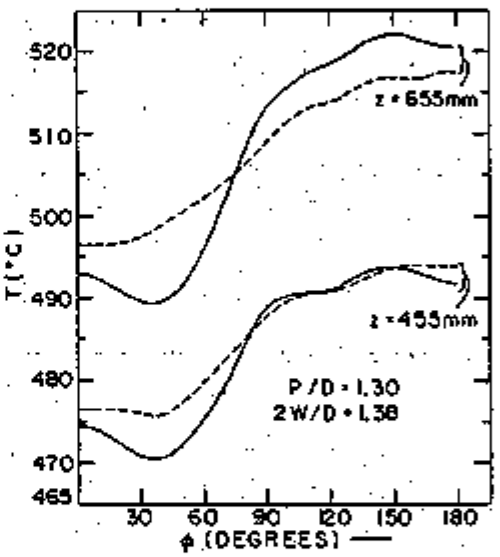

Fig. 5 Comparison between Experiment [17] (---) and Single-Cell, 3-D Analysis (—) for the Outside Clad Temperature Distribution of a Side Fin

Fig. 6

2

1

0

Fig. 7 Eff
for

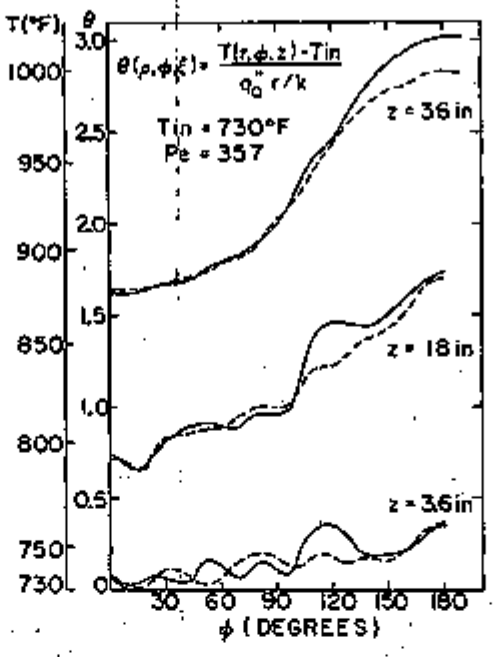

Fig. 6 Comparison of Outside Clad Temperatures for a Corner Pin in a Fuel Assembly as Obtained from Single-Cell,3-D (---) and Two-Cell (—) Analyses

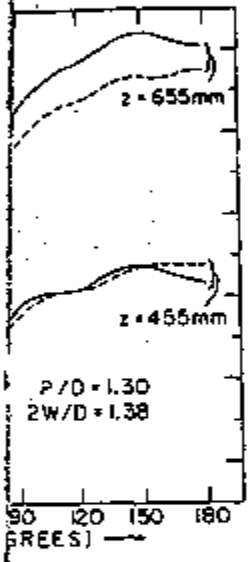

between Experiment
Single-Cell, 3-D
for the Outside Clad
istribution of a

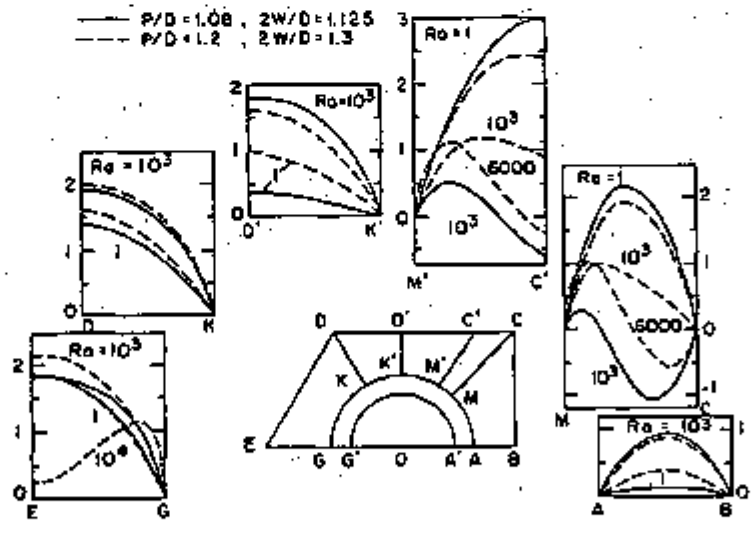

Fig. 7 Effect of Mixed Convection Upon the Velocity Profiles in a Side Cell for Two Different Designs

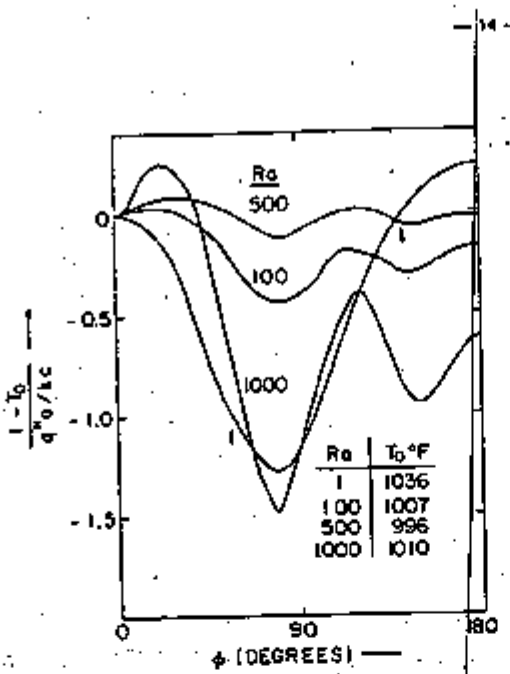

Fig. 8 Effect of Different Ra-Numbers Upon the Corner Pin Cladding Temperature Distribution of a Blanket Assembly ($q' = 1$ KW/ft, $T_{co} = 995°F$, $T_o = T_c(b,0)$)

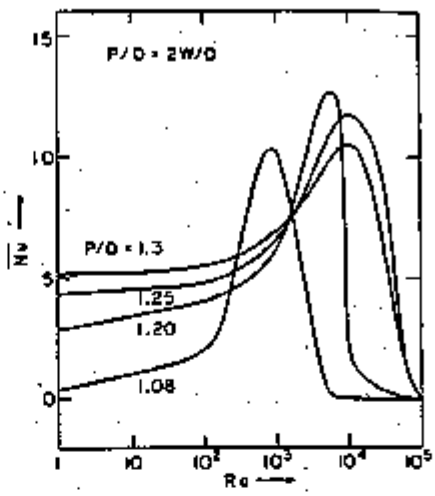

Fig. 9 Average Nusselt Number for the Side Cell as Function of Ra ($P_{wet} = \pi b + P/2$)

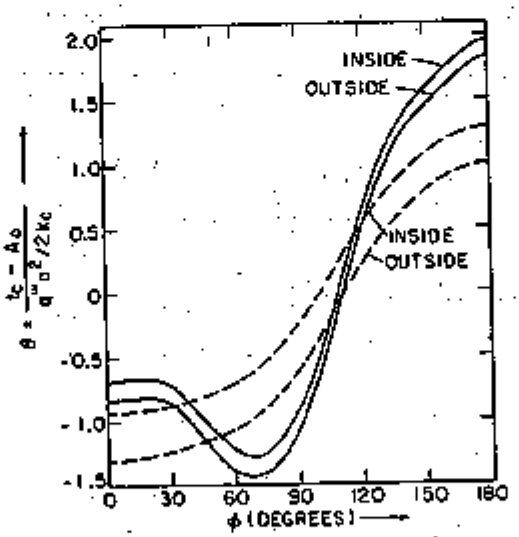

Fig. 10 Dimensionless Inside and Outside Caldding Temperature Distributions for Fuel (---) and Blanket (—) Assembly Corner Rods as Derived from Fully-Developed Slug Flow Analysis

Fig. 11 T
d

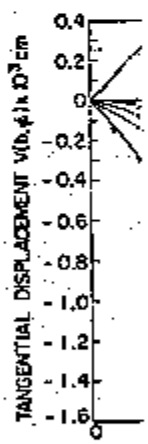

Fig. 12 Az
Thermoelas
of the Out
(For Symbol

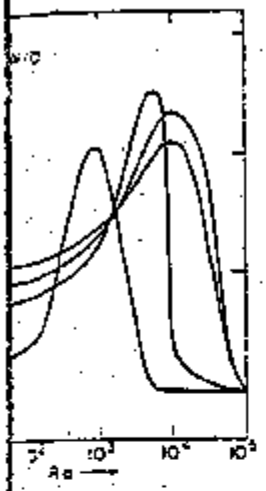

e Nusselt Number for
11 as Function of Ra
r/2)

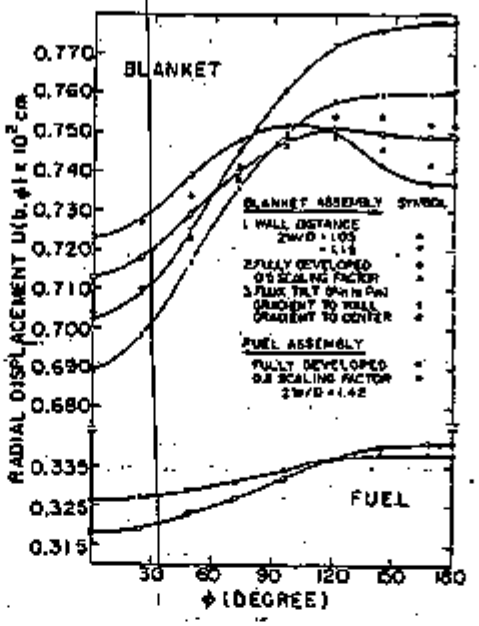

Fig. 11 Thermoelastic Circumferential Radial Displacement of the Outer Cladding Surface for Different Assumptions and Conditions

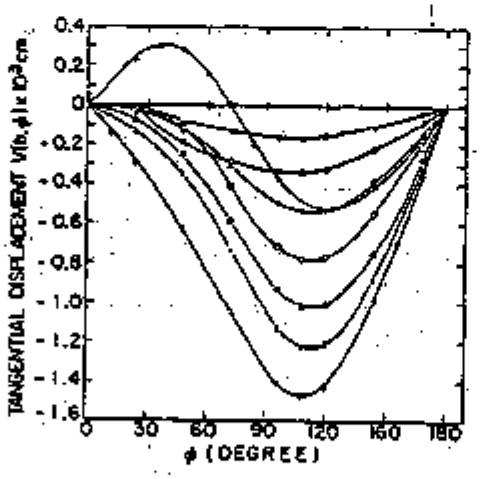

Fig. 12 Azimuthal Variation of Thermoelastic Tangential Displacements of the Outside Cladding Surface (For Symbols see Insert in Fig. 10)

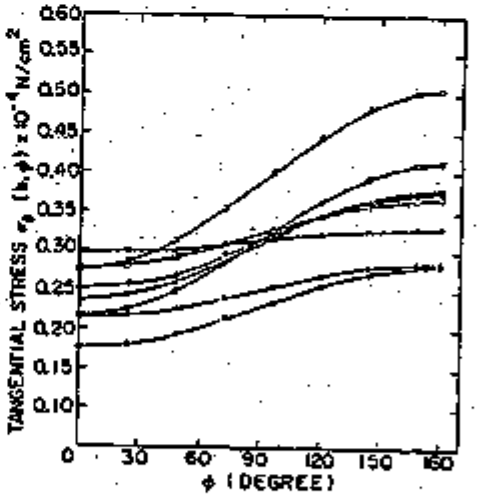

Fig. 13 Azimuthal Variation of Thermoelastic Stress Distributions (for Symbols see Insert in Fig. 10)

ature Distributions
ods as Derived from

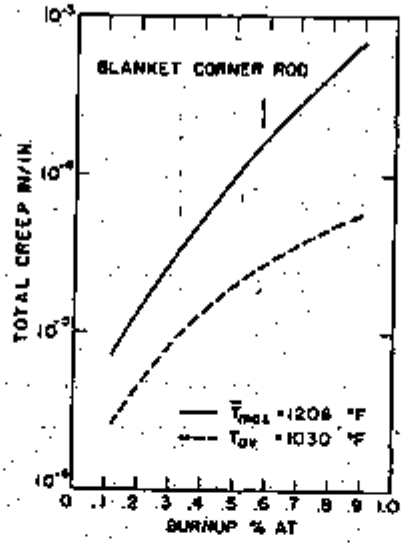

Fig. 14 Total Clad Creep (Thermal, Irradiation, Swelling) as Function of Burn-up for a Blanket Corner Rod with Average and Maximum Temperature Loads (Material: 20% CW 316 SS)

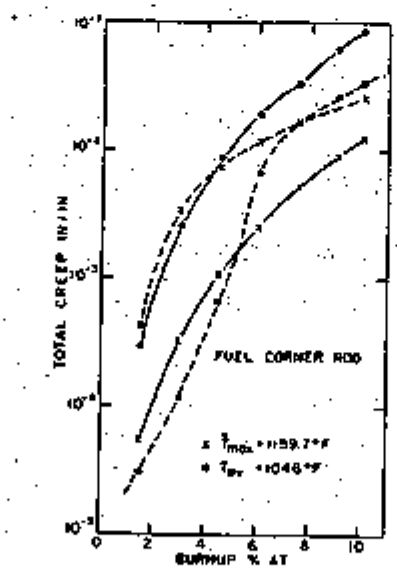

Fig. 15 Total Clad Creep (Thermal, Irradiation, Swelling) as Function of Burn-up for a Fuel Corner Rod with Average and Maximum Temperatue Loads (← Annealed 316 SS; --- 20% CW 316 SS)

SUMMAR

Radiatio
maximum i
served defo
terials, wit

The
nious
problem
changes i
the stainles
that underg
changes is e
position and
irradiation c
affecting the

A model
the effects of
swelling and
in the amo
bon from
vations sup
tion before ir
reactor. Simil
with the loca
irradiated in